Master's thesis

NTNU
Norwegian University of Science and Technology
Faculty of Information Technology and Electrical Engineering
Department of Engineering Cybernetics

Carl Martin Krokeide

Propulsion-based Attitude Control of Nanosatellites

Master's thesis in Cybernetics and Robotics
Supervisor: Jan Tommy Gravdahl
June 2020

NTNU
Norwegian University of Science and Technology

Carl Martin Krokeide

Propulsion-based Attitude Control of Nanosatellites

Master's thesis in Cybernetics and Robotics
Supervisor: Jan Tommy Gravdahl
June 2020

Norwegian University of Science and Technology
Faculty of Information Technology and Electrical Engineering
Department of Engineering Cybernetics

NTNU
Norwegian University of
Science and Technology

NTNU
Norges teknisk-naturvitenskapelige universitet

Fakultet for informasjonsteknologi, matematikk og elektroteknikk
Institutt for teknisk kybernetikk

MSc thesis assignment

Name of the candidate: Carl Martin Krokeide
Subject: Engineering Cybernetics
Title: Propulsion-based Attitude Control of Nanosatellites

Background:

The student shall develop a nonlinear model for dynamics & control of spacecraft, with applications to future smallsatellites developed at NTNU SmallSat Lab. Until now there has been research performed, together with NanoAvionics, on a 6U CubeSat performing a slew maneuver using reaction wheels and magnetorquers to achieve better imaging quality for a hyperspectral imager. Due to strict power budget during such missions, the student will investigate methods using propulsion (cold gas or electric) to dump momentum, improve power consumption and achieve high accuracy in pointing and rotational maneuvers of a spacecraft. Matlab/Simulink and AGI Systems ToolKit (STK) will be used to develop the dynamical model of spacecraft and actuators together with suitable controllers

Tasks:

1. Develop a modular nonlinear model for a satellite with emphasis on orbital mechanics, control theory, mathematics and physics. The model shall be modular such that various spacecraft, internal actuator and thruster parameters may be chosen.
2. Space environment disturbances in Low-Earth-Orbit shall be included such as solar radiation pressure, gravity gradient, electromagnetic field, atmospheric drag. Detailed model of disturbances from the spacecraft model, sensors and actuators (magnetorquers, reaction wheels and propulsion unit) shall also be presented.
3. Investigate trade-offs of using reaction wheels and propulsion for pointing and slew maneuver:
    a. How many propulsion units are required
    b. How many reaction wheels are required
    c. Which are best suited in terms of accuracy, power consumption and momentum storage.
4. Design controllers based on optimal control, model predictive control (MPC) and nonlinear feedback control for both pointing and slew maneuver. Stability of the augmented model shall be analyzed. Performance of suitable controllers shall be characterized:
    a. Root-mean-square error
    b. Steady-state error
    c. Settling time

To be handed in by: 22/6-2019
Co-supervisors: Mariusz Eivind Grøtte and Bjørn Andreas Kristiansen

Jan Tommy Gravdahl
Professor, supervisor

Abstract

The last decade has seen a growing trend towards miniaturized satellite technology. This research intends to derive a complete mathematical model and attitude control system for miniaturized propulsion systems on nanosatellites, and determine to which extent they are suitable compared to other actuation solutions. Hopefully, this research will contribute to data and insight that will aid future design specification processes in nanosatellite projects.

There are four main contributions of this thesis. First, a dynamical model of a nanosatellite with actuators is derived; A simulation environment, including orbital perturbations, is then developed; An adaptive integer model predictive controller for attitude maneuvers is implemented; And lastly, the performance of different actuators and controllers is measured and compared.

Simulations for this study were carried out using MATLAB software. The project aimed to develop modular software that is compatible with different satellite and actuator configurations.

Sammendrag

Det siste tiåret har sett en økende trend mot miniatyrisert satellitteknologi. Dette forskningsarbeidet er ment å utlede en komplett matematisk modell og et attityde-reguleringssystem til bruk med miniatyriserte fremdriftssystemer på nanosatellitter, samt fastslå til hvilken grad disse er passende sammenliknet med andre aktueringsløsninger. Håpet er at denne forskningen vil kunne bli brukt som et data- og innsiktsgrunnlag for fremtidige designspesifikasjonsprosesser i nanosatellittprosjekter.

Det er fire hovedkontribusjoner i denne oppgaven. For det første er en dynamisk modell av en nanosatellitt med pådragsorganer utledet; Et simuleringsprogram som inkluderer orbitale forstyrrelser er utviklet; En adaptiv integerbasert modell-prediktiv regulator for attitydemanøvre er implementert; Og til slutt er ytelsen til de forskjellige pådragsorganene og regulatorene målt og sammenliknet.

Simuleringene i denne studien ble gjennomført i simuleringsverktøyet MATLAB. Prosjektet tok sikte på å utvikle modulær programvare som er kompatibel med forskjellige satellitt- og pådragsorgankonfigurasjoner.

Preface

Throughout the thesis work, I have received excellent support, advice, and mentoring from my supervisors Mariusz Grøtte, Bjørn Kristiansen, and prof. Jan Tommy Gravdahl. Their continuous involvement in the project, despite the ongoing pandemic, has been deeply appreciated. Reaching beyond the scope of this thesis, they have provided me with insight into the development of the HYPSO satellite and introduced me to several exciting aspects of space engineering.

The thesis consists of theoretical derivations and practical simulations. Parts of the theory presented in the second chapter, *Background Theory*, is a reformulation of the material presented in the author's specialization project report. The author has implemented the simulator, and the figures presented throughout the report are designed by the author unless stated otherwise.

Carl Martin Krokeide
Trondheim, Norway
June 20, 2020

Contents

List of Tables

List of Figures

Space is hard.

Chapter 1

Introduction

The thesis work was conducted to support the NTNU SmallSat Lab and completes the degree of M.Sc. in Robotics and Cybernetics at the Norwegian University of Science and Technology (NTNU).

This chapter provides a description of the motivation behind the research (section 1.1), a presentation of related works (section 1.2) and an outline of the thesis (section 1.3).

1.1 Motivation

Over the past decade, there has been a dramatic increase in the development and launch of nanosatellites [10]. The innovation in small-satellite technology provides relatively cheap access to space for both academic institutions, government

agencies, and private enterprises. By utilizing the CubeSat platform, a satellite can be constructed using off-the-shelf subsystems, which drastically reduces the development costs [1]. In recent years, many companies have developed technologies tailored for CubeSat platforms, including miniaturized propulsion systems. However, there is a lack of research on the practical usefulness of propulsion systems for attitude control on CubeSats. This thesis provides a mathematical model and an attitude control system for use with propulsion systems on nanosatellites. The applicability of a propulsion system for the NTNU SmallSat Lab is also analyzed and discussed.

The simulations performed in this thesis are based on the HYPSO satellite (HYPer-Spectral smallsat for Ocean observation), which is currently being developed at the Norwegian University of Science and Technology (NTNU). The HYPSO satellite is a 6U CubeSat equipped with reaction wheels and magnetorquers. In this research, a propulsion system is imagined added to the satellite design. The HYPSO project's mission is to observe oceanographic phenomena using a hyperspectral camera, with mission requirements that require accurate attitude control during pointing and slew rate maneuvers.

1.2 Previous Work

There is little published data on optimal attitude control using propulsion systems on nanosatellites. However, two miniaturized propulsion systems have recently been developed, suitable for orbital and attitude control. The first system is an electric ion-based propulsion system developed by researchers at the Technical

University of Dresden [3]. The second system is a water-based resistojet system developed by the Finnish company *Aurora Propulsion Technologies* [2]. Both systems have the advantage of not utilizing any dangerous chemicals, which fulfills common CubeSat standards [16].

The simulated satellite includes reaction wheels and magnetorquer actuators. These are conventional attitude actuators on nanosatellites. A derivation of the reaction wheel dynamics was explicitly done for the NTNU HYPSO project by Kristiansen [11].

1.3 Thesis Outline

The thesis is organized in seven chapters. This chapter, *Introduction*, describes the motivation for the research and introduces previous work. The second chapter, *Background Theory*, introduces necessary concepts in orbital mechanics. In the third chapter, *Satellite Model*, a mathematical model of the satellite dynamics is derived. The attitude controllers developed are presented in the fourth chapter, *Controller Design*, and the MATLAB simulator is presented in the fifth chapter, *Simulations*. The results are presented in the sixth chapter, *Results*, and discussed in chapter seven, *Discussion*. Lastly, a conclusion is provided and further work is proposed in in chapter eight, *Conclusions*.

Chapter 2

Background Theory

This chapter serves as an introduction to relevant theory in orbital mechanics. The intended reader is someone with a technical background other than orbital mechanics, and the purpose is to introduce the nomenclature and concepts used in this thesis.

The chapter is organized as follows: First, the mechanics of objects in orbit is discussed in section 2.1 *Orbital Mechanics*. Then, orbital perturbations, which disturb the natural motion of orbiting objects, are discussed in section 2.2 *Orbital Perturbations*.

2.1 Orbital Mechanics

Orbital mechanics concerns the study of natural and actuated motion of artificial satellites. The section is meant to provide the most important definitions and equations that govern satellite dynamics, and provide a mathematical description of orbits. The coordinate frames applied for the translational motion are introduced in subsection 2.1.1 *Coordinate Systems*. The equations that govern the satellite motion are given in subsection 2.1.2 *Equation of Motion*. A parametric description of orbits is presented in subsection 2.1.3 *Orbital Parameters*. Finally, the moment of inertia properties that govern the satellite attitude dynamics are defined in subsection 2.1.4 *Inertia*.

2.1.1 Coordinate Systems

This section presents two different reference frames for representing the location of an orbiting object in space relative to other objects. The origin of both coordinate systems is placed at the center of the Earth. The *Earth-Centered Intertial Coordinate System* (sec. 2.1.1) is an *inertial* coordinate system, meaning that the frame is assumed unaccelerated, while the *Earth-Centered Earth-Fixed Coordinate System* (sec. 2.1.1) is non-inertial.

Earth-Centered Intertial Coordinate System

Earth-Centered Intertial (ECI) coordinate systems originate in the center of mass of the Earth and are non-rotating with respect to the stars. In this project, we consider the *J2000* definition of the ECI frame. The ECI frame is here denoted with superscript i.

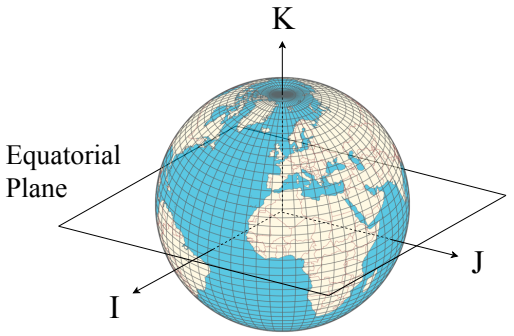

Figure 2.1: Earth-centered coordinate system. Figure based on work by *Hellerick* [8] with added axes and equatorial plane.

The position of celestial objects at noon on January 1st, 2000, defines the J2000 ECI frame [21]. It is spanned by the principle I-, J- and K-axes. The I-axis points towards the center of the Sun, the K-axis points along the mean axis of rotation of the Earth, and the J-axis is perpendicular to the other axes, thus pointing 90ř East of the principal I-axis along the mean Equatorial plane.

The position of an orbiting object described in the ECI frame is given in Equation (2.1), and the velocity is given in Equation (2.2).

$$\boldsymbol{r}^i = \bar{x}\boldsymbol{I}^i + \bar{y}\boldsymbol{J}^i + \bar{z}\boldsymbol{K}^i \tag{2.1}$$

$$\boldsymbol{v}^i = \dot{\boldsymbol{r}}^i = \dot{\bar{x}}\boldsymbol{I}^i + \dot{\bar{y}}\boldsymbol{J}^i + \dot{\bar{z}}\boldsymbol{K}^i \tag{2.2}$$

Earth-Centered Earth-Fixed Coordinate System

Earth-Centered Earth-Fixed (ECEF) coordinate systems originate in the center of mass of the Earth and rotate with the Earth. Here, the *International Astronomical Union* (IAU) resolutions of 2000/2006 are used to define the transformation between the J2000 ECI coordinates and the ECEF coordinates. The ECEF frame is indicated with superscript e.

The position of an orbiting object described in the ECEF frame is given in Equation (2.3), and the velocity is given in Equation (2.4).

$$\boldsymbol{r}^e = \bar{x}\boldsymbol{I}^e + \bar{y}\boldsymbol{J}^e + \bar{z}\boldsymbol{K}^e \tag{2.3}$$

$$\boldsymbol{v}^e = \dot{\boldsymbol{r}}^e = \dot{\bar{x}}\boldsymbol{I}^e + \dot{\bar{y}}\boldsymbol{J}^e + \dot{\bar{z}}\boldsymbol{K}^e \tag{2.4}$$

2.1.2 Equation of Motion

Discoveries made by the 17th-century German scientist Johannes Kepler about celestial motion led Isaac Newton to develop his law of universal gravitation, presented in Equation (2.5). The equation considers a system consisting of two objects, in which F_g is the gravitational force acting between the objects, G is the universal gravitational constant, m_1 and m_2 are the point masses of the objects, and r is the position vector connecting the point masses.

$$\mathbf{F} = Gm_1m_2\frac{\mathbf{r}}{|\mathbf{r}|^3} \tag{2.5}$$

The equation of motion used for the simulations is given in Equation (2.6). In this equation, $\mu = G \cdot M = 398600.4415\, km^3 s^{-2}$ is the product of the universal gravitational constant and the mass of the Earth, considered as the standard gravitational parameter [13]; $\mathbf{r}_{sat}$ is the position vector of the satellite center of mass from the center of the Earth, and m_{sat} is the mass of the satellite. Additional forces acting on a satellite other than the Newtonian force of gravity are considered *perturbing* forces, denoted $\boldsymbol{F}_p$. A selection of the perturbing forces are discussed in section 2.2 *Orbital Perturbations*.

$$\ddot{\mathbf{r}}^i_{sat} = \mathbf{a}^i_{sat} = \mu \frac{\mathbf{r}^i_{sat}}{\left|\mathbf{r}^i_{sat}\right|^3} + \frac{\boldsymbol{F}^i_p}{m_{sat}} \tag{2.6}$$

2.1.3 Orbital Parameters

The following subsection gives an introduction to a parametric description of orbits using the definitions of *orbital parameters* made by [5].

Under the assumption that an orbit is an ideal *Keplerian* orbit (only affected by the Newtonian force of gravity discussed in subsection 2.1.2), it can be uniquely identified using six orbital elements. Three parameters are required to define the orbit on a plane, and three additional parameters are needed to further place the orbit in three-dimensional space. A summary of the six orbital elements is given in Table 2.1, and an illustration of four of them is given in Figure 2.2.

Name	Symbol	Range	Unit
Specific angular momentum	h	$[0,\ \infty)$	$\frac{kgm}{s^2}$
Inclination	i	$[0,\ 180]$	$^\circ$
Right ascension of the ascending node	Ω	$[0,\ 360]$	$^\circ$
Eccentricity	e	$[0,\ \infty)$	-
Argument of perigee	ω	$[0,\ 360]$	$^\circ$
True anomaly	Θ	$[0,\ 360]$	$^\circ$

Table 2.1: Overview of the six parameters describing an orbit.

Three parameters describe the orbit plane: the *specific angular momentum*, *eccentricity*, and *true anomaly*. The **specific angular momentum** is the angular momentum of the orbiting object seen in an Earth-centered inertial frame, which is constant for a non-perturbed orbit. The **eccentricity** value describes how close the shape of the orbit is to a perfect circle. The value of the eccentricity can be found by dividing the distance between the center of the orbit and one of its *foci* by the *semi-major axis* (the largest radius of the orbit). Orbit shapes corresponding to different eccentricity values are given in Table 2.2. **True anomaly** is the angle between the position of the orbiting object and *periapsis* (the point on the orbit with the shortest distance to the central body) seen from the main focus of the orbit.

So far, a two-dimensional orbit plane has been defined. To place the orbit plane in three-dimensional space, three additional axis rotations are required. The orbital elements corresponding to these rotations are the *inclination*, *right ascension of the ascending node* and the *argument of perigee*. The **inclination**

$e = 0$	Circle
$0 < e < 1$	Ellipse
$e = 1$	Parabola
$e > 1$	Hyperbola

Table 2.2: Orbital shapes corresponding to different eccentricity values.

describes the angle between the orbital plane and the *equatorial* (Earth XY) plane. The **right ascension of the ascending node** is the angle between the equatorial X-axis and the point on the equatorial plane where the orbit passes through from below. The third angle, the **argument of perigee**, is the angle in the orbital plane between the point of passing through the equatorial plane from below and the point of perigee as seen from the focus of the orbit.

2.1.4 Inertia

The angular momentum $\boldsymbol{H}$, with unit $\frac{kgm^2}{s}$, of a body is determined by the angular velocity $\boldsymbol{\omega}$ and inertia $\boldsymbol{I}$, as shown in Equation (2.7). The rate of change in angular velocity of an object is thus dependent on the applied torque $\boldsymbol{\tau}$, measured in Nm, and the inertia $\boldsymbol{I}$ of the satellite, with unit kgm^2.

$$\boldsymbol{H}^i = \boldsymbol{I}^i \boldsymbol{\omega}^i, \quad \boldsymbol{\tau}^i = \frac{{}^i d\boldsymbol{H}^i}{dt} \tag{2.7}$$

The inertia matrix $\boldsymbol{I} \in \mathbb{R}^{3\times3}$ is given in Equation (2.8), as defined by Fossen [7]. In this expression, I_x, I_x and I_x are the moments of inertia about the x-, y-

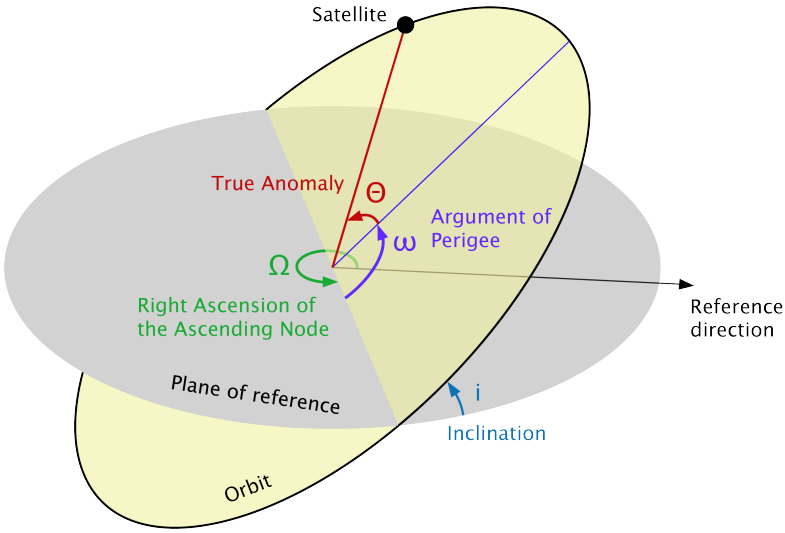

Figure 2.2: Illustration of Four of the Orbital Elements. Figure based on work by *Lasunncty* [12] with modifications to the notation.

and z-axes, and $I_{xy} = I_{yx}$, $I_{xz} = I_{zx}$ and $I_{yz} = I_{zy}$ are the products of inertia, provided in Equation (2.9).

$$\boldsymbol{I} := \begin{bmatrix} I_x & -I_{xy} & -I_{xz} \\ -I_{yx} & I_y & -I_{yz} \\ -I_{zx} & -I_{zy} & I_z \end{bmatrix}, \quad \boldsymbol{I} = \boldsymbol{I}^T > \boldsymbol{0} \tag{2.8}$$

$$
\begin{aligned}
I_x &= \int_V \left(y^2 + z^2\right) \rho\,(x,y,z)\,dV; \quad I_{xy} = I_{yx} = \int_V xy\ \rho\,(x,y,z)\,dV \\
I_y &= \int_V \left(x^2 + z^2\right) \rho\,(x,y,z)\,dV; \quad I_{xz} = I_{zx} = \int_V xz\ \rho\,(x,y,z)\,dV \\
I_z &= \int_V \left(x^2 + y^2\right) \rho\,(x,y,z)\,dV; \quad I_{yz} = I_{zy} = \int_V yz\ \rho\,(x,y,z)\,dV
\end{aligned} \tag{2.9}
$$

When the axes of the coordinate system in which the inertia matrix is defined are aligned with the *principal axes* of the body, the inertia matrix is diagonal. The moment of inertia matrix for solid cuboid with evenly distributed mass m and dimensions x, y, z along the principal axes is given in Equation (2.10).

$$
\boldsymbol{I}_c^b = \begin{bmatrix}
\frac{1}{12}m\left(y^2 + z^2\right) & 0 & 0 \\
0 & \frac{1}{12}m\left(x^2 + z^2\right) & 0 \\
0 & 0 & \frac{1}{12}m\left(x^2 + y^2\right)
\end{bmatrix} \tag{2.10}
$$

2.2 Orbital Perturbations

Orbital perturbations is a term used for all effects that cause an object's orbit to deviate from the ideal *Keplerian* orbit. The Keplerian orbit model considers only the forces of the point-mass central body acting on the orbiting object. Forces originating from the uneven distributions of mass on Earth (subsection 2.2.1), atmospheric drag (subsection 2.2.3), solar radiation pressure (subsection 2.2.4), or gravitational pull from other celestial bodies are all examples of perturbing

forces. The gravity gradient (section 2.2.2) is also discussed.

2.2.1 Earth's Oblateness

Oblateness is a measure of the flattening of a sphere, and is defined as in Equation (2.11) [5], in which γ is the oblateness measure, r_e the equatorial radius and r_p the polar radius.

$$\gamma = \frac{r_e - r_p}{r_e} \tag{2.11}$$

The Earth's equatorial radius is larger than the polar radius due to the centrifugal forces originating from its spin.

An oblate spheroid, unlike a perfect sphere, has a gravitational field that varies with latitude. *Harmonic parameters* are used to quantify the effects of oblateness on gravitational pull. The second zonal harmonic, $\boldsymbol{J}_\Gamma 30002$, is the most significant harmonic force, with its effect being about one thousand times larger than the next greatest zonal harmonic contributor, $\boldsymbol{J}_\Gamma 30003$.

The gravitational pull on an orbiting object with the effects of the second zonal harmonic J_2 may be modeled as in Equation (2.12), based on [19]. In Equation (2.12), μ is the standard gravitational constant, J_2 is the second zonal harmonic, R_e is the mean equatorial radius of the Earth, $\boldsymbol{r}$ is the position of the satellite and r is its norm, and $\boldsymbol{z}_G = [0, 0, 1]^T$ is the z-axis vector.

$$\boldsymbol{F}^i_{J_2} = \frac{3\mu J_2 R_e^2}{2r^5}\left[5\left(\frac{(\boldsymbol{r}^i \cdot \boldsymbol{z}_G)^2}{r^2} - 1\right)\boldsymbol{r}^i - 2\left(\boldsymbol{r}^i \cdot \boldsymbol{z}_G\right)\boldsymbol{z}_G\right] \tag{2.12}$$

2.2.2 Gravity Gradient

The satellite interacting with Earth's gravity field produces a torque known as the gravity gradient. The torque is produced on volumes of mass that are not aligned with Earth's gravitational pull. This happens as a consequence of the property that a gravitational field decreases quadratically with distance. The portion of the satellite mass positioned closest to the Earth's center experience a stronger gravitational pull than the mass positioned further away. The torque can be modeled as in Equation (2.13), based on [19].

$$\boldsymbol{\tau}^b_G = \frac{3\mu}{r^5}\left[\boldsymbol{r}^b \times \boldsymbol{I}^b_{sat}\boldsymbol{r}^b\right] \tag{2.13}$$

In Equation (2.13), $\boldsymbol{\tau}^b_G$ denotes the gravity gradient torque produced, μ the standard gravitational constant, and $\boldsymbol{I}^b_{sat}$ is the inertia matrix of the satellite. $\boldsymbol{r}^b$, with r being its norm, is the position of the satellite relative to the center of the Earth, as seen in the body frame of the satellite.

2.2.3 Atmospheric Drag

Objects orbiting near Earth will experience a decrease in velocity due to collisions with atmospheric particles, known as drag. The magnitude of the acceleration

depends on the density of the atmospheric particles. The atmosphere's density has both latitudinal, longitudinal, periodic, and random variations. However, it depends mainly on the gravitational forces exerted on the atmospheric particles by the Earth and thus the altitude of the orbit. Other contributing factors to the atmospheric density are the Sun's position and radiation activity and variations in the Earth's magnetic field. The variations in the atmospheric drag forces are represented in the density of the atmosphere, denoted ρ. In this research, the atmospheric density is calculated by taking the average value of the Harris-Priester model [15] corresponding to the altitude.

A model of the force and torque produced by atmospheric drag, based on [15] and [19], is given in Equations (2.14) and (2.15). The force and torque produced by the atmosphere are found by summation of the atmospheric effect on all surfaces of the satellite in the set S_{wa}, which is the set of *wetted area* surfaces, which are the surfaces exposed to atmospheric drag forces. The wetted areas are defined as the surfaces on which the dot product of the surface normal and relative velocity of the satellite to the atmosphere is positive.

$$\boldsymbol{F}^b_{drag} = \sum_{A_d \in S_{wa}} \boldsymbol{F}^b_{drag_{A_d}} = -\frac{1}{2}\, C_D\, \rho\, v^2_{rel}\, \hat{\boldsymbol{v}}^b \sum_{A_d \in S_{wa}} A_d\, (\boldsymbol{n}^b_{A_d} \cdot \hat{\boldsymbol{v}}^b) \qquad (2.14)$$

In Equation (2.14), C_D is the coefficient of drag, a factor which indicates how susceptible the spacecraft is to drag forces, and ρ is the atmospheric density at the position of the spacecraft. $\boldsymbol{v}_{rel}$ is the relative velocity of the spacecraft to the atmosphere, and $\hat{\boldsymbol{v}}^b = \frac{\boldsymbol{v}^b_{rel}}{v_{rel}}$ represents the direction of the relative velocity in the body frame. A_d represents the area of the surface in the set S_{wa}, and $\boldsymbol{n}^b_{A_d}$

represents the surface normal in the body frame.

$$\boldsymbol{\tau}^b_{drag} = \sum_{A_d \in S_{wa}} \boldsymbol{c}^b_{A_d} \times \boldsymbol{F}^b_{drag_{A_d}} \tag{2.15}$$

The torque produced by the atmospheric drag is given in Equation (2.15). In this equation, $\boldsymbol{c}^b_{A_d}$ is the vector from the center of mass of the satellite to the center of the given surface in the set S_{wa}, and $bmF^b_{drag_{A_d}}$ is the atmospheric drag force corresponding to the surface.

2.2.4 Solar Radiation Pressure

Solar radiation pressure concerns the forces acting on a spacecraft due to radiation from the Sun. The forces originate from the momentum exchange between the photons emitted from the Sun and the body of the spacecraft. The magnitude of the force varies based on solar activity, and the perturbation becomes more pronounced at higher altitudes as seen from the Earth, compared to other perturbing effects. It is necessary to know the force of the solar radiation per unit area, p_{srp}, which is difficult to predict accurately, as it varies based on solar activity. Here, an average estimate from [15] is used as a constant value to model the incoming solar radiation. A model of the solar radiation pressure force and torque, based on [15] and [19], is given in Equations (2.16) and (2.17).

$$\boldsymbol{F}^b_{srp} = \sum_{A_s \in S_\odot} \boldsymbol{F}^b_{srp_{A_s}} = -\boldsymbol{s}^b \; p_{srp} \; C_R \sum_{A_s \in S_\odot} A_s \; \left(\boldsymbol{n}^b_{A_s} \cdot \boldsymbol{s}^b \right), \quad \boldsymbol{s}^b = \frac{\boldsymbol{r}^b_{sat-\odot}}{r_{sat-\odot}} \tag{2.16}$$

In Equation (2.16), $\boldsymbol{r}_{sat-\odot}$ is the vector from the satellite to the center of the Sun, $r_{sat-\odot}$ is its norm, and p_{srp} is the force of the solar radiation per unit area. C_R is the coefficient of reflectivity of the spacecraft, a factor representing the spacecraft's ratio between reflected and absorbed radiation. The set $S_\odot$ contains the surfaces of the spacecraft that are exposed to the Sun, which is found using the SIGHT algorithm [15]. A_s and $\boldsymbol{n}^b_{A_s}$ are the area and normal vectors of the surfaces.

$$\boldsymbol{\tau}^b_{srp} = \sum_{A_s \in S_\odot} \boldsymbol{c}^b_{A_s} \times \boldsymbol{F}^b_{srp_{A_s}} \tag{2.17}$$

In Equation (2.17), $\boldsymbol{c}^b_{A_s}$ is the vector from the satellite's center of mass to the center of the surface, and $\boldsymbol{F}^b_{srp_{A_s}}$ is the corresponding force from the solar radiation pressure on the surface. As for the force calculation, the set $S_\odot$ contains the surfaces of the spacecraft that are exposed to the Sun.

2.3 Actuator Power Models

This section presents the power consumption models used for the actuators. An estimation of the power consumption is later used to find an optimal combination of actuator gains minimizing the total power consumption of the satellite.

The following actuators are discussed: subsection 2.3.1 covers *Reaction Wheels*, subsection 2.3.2 the *Magnetorquer*, and subsection 2.3.3 considers *Propulsion Systems*.

2.3.1 Reaction Wheels

To model the reaction wheels' energy consumption, the components that make up the actuator are considered. The reaction wheels consist of a brushless electric motor connected to the spacecraft on one end and a high inertia flywheel on the other end. For an electric motor, the mechanical output power P_m is given by the angular speed ω and torque produced $\tau = I\frac{d}{dt}\omega$. The electric input power P_e is given by the mechanical output power and the efficiency η of the motor, as defined in Equation (2.18) [22].

$$P_m = |\omega|\,\tau = |\omega|\,I\left|\frac{d}{dt}\omega\right|, \quad P_e = \frac{P_m}{\eta} \tag{2.18}$$

2.3.2 Magnetorquer

To approximate the power consumption of the magnetorquer, a simplified model of the actuator construction is used. The magnetorquer is made up of multiple coils of conducting wire placed in an orthogonal configuration. The coils are made up of n turns, with the resulting vector area given by $\boldsymbol{S}$. The strength of the magnetic dipole, $\|\boldsymbol{m}\|$, created by any of the coils in the configuration is proportional to the current applied, I, as given in Equation (2.19) [6].

$$\|\boldsymbol{m}\| = nI\|\boldsymbol{S}\| \tag{2.19}$$

Combining Equation (2.19) and Ohm's law, we get a simplified expression for the power consumed as a result of the resistance of the coils and the magnetic dipole created, given in Equation (2.20), in which $m = \|\boldsymbol{m}\|$ and $S = \|\boldsymbol{S}\|$.

$$P_{MTQ} = R_{coil} I^2 = R_{coil_i} \left(\frac{m}{nS} \right)^2 \tag{2.20}$$

2.3.3 Propulsion Systems

The power consumption of the thrusters consists of the preheating stage and thrust firing actuation. The preheating stage is neglected in this research. At thruster firing, the thrusters' power consumption is defined as the maximum rating in the provided thruster specifications. The resulting estimated power consumption is given by Equation (2.21), in which n is the number of thrusters.

$$P_T = \sum_n P_n, \quad P_n := \begin{cases} P_{specified}, & \text{if thruster is firing} \\ 0, & \text{otherwise} \end{cases} \tag{2.21}$$

2.4 Genetic Algorithm Optimization

Genetic algorithms are inspired by biological evolution and the concept of *natural selection*. The method initializes a population of random initial points, evaluates the objective function corresponding to the population, and modifies the

population based on biologically inspired operators such as *mutation*, *crossover*, and *selection* [17]. The algorithm accepts non-smooth functions with any type of constraint. The stopping criteria for the algorithm can be based on either optimality conditions, resource constraints, or a combination of both.

Here, the population consists of vectors describing different actuation sequences. **Mutation** is the operation of randomly changing some of the vectors' components to produce a new vector. Similarly, **crossover** is the operation of combining elements of previous vectors in the population to produce a new vector. **Selection** is the operation of including the best-scoring members of the current generation in the next generation's population.

Chapter 3

Satellite Model

This chapter derives the dynamical equations of the satellite orbital position and attitude, which will form the basis for the controller and simulation design, and is structured as follows: Assumptions made regarding the satellite construction and the satellite fixed reference frames used for modeling are discussed in section 3.1 *Satellite Assumptions*. The dynamics of the actuators are derived in sections 3.2 *Reaction Wheels*, 3.3 *Magnetorquer*, and 3.4 *Propulsion*. Finally, the complete dynamics of the satellite are derived in section 3.5 *Satellite Dynamics*.

3.1 Satellite Assumptions

In the modeling of the satellite dynamics, some assumptions about its structural design had to be made. The satellite is assumed to be a single rigid body, with time-varying mass and inertia. The satellite is assumed to be equipped with

three types of actuators:

1. A set of reaction wheels, with equal weight and dimension.
2. Magnetorqers, able to produce a magnetic field along all three axes of the satellite.
3. Propulsion units, in two defined configurations.

The satellite is further assumed to be a solid cuboid with evenly distributed mass when the propellant storage modules are excluded.

3.1.1 Reference Frames

Two reference frames are used to define the satellite dynamics: the *body* frame and the *structural* frame. The **body frame** of the satellite, denoted $\{b\}$, is fixed to the center of mass of the satellite. The satellite is thus rotating around the center of the body frame. The axes of the body frame point along the satellite dimensions, as illustrated in Figure 3.1. The satellite **structural frame**, denoted $\{s\}$, is fixed at a point on the satellite structure rather than the center of mass, with the axes pointing along with the satellite structural dimensions. It is assumed that the axes of the body frame are parallel to the axes of the structural frame and non-rotating, and there is thus only translation and no rotation between the frames.

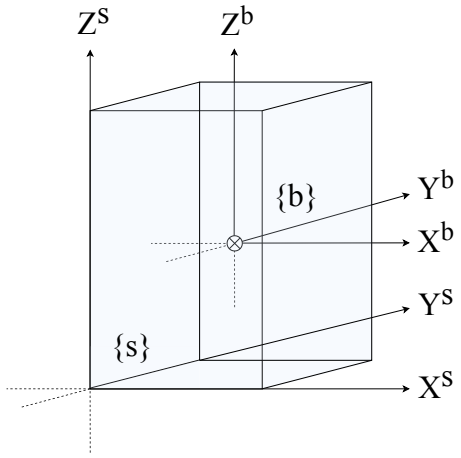

Figure 3.1: Illustration of Satellite Attached Frames. The Structural Frame is attached to the Satellite Construction, while the Body Frame is attached to the Center of Mass of the Satellite, denoted $\otimes$. There is no rotation between the two frames, and the axes in both frames point along the satellite dimensions.

3.2 Reaction Wheels

The reaction wheels' total angular momentum in an inertial frame consists of the momentum caused by the rotation of the satellite body, on which the reaction wheels are mounted, and the rotation of the wheels themselves relative to the satellite body. The total angular momentum of the reaction wheels in the body frame is given by Equation (3.1c), with $\boldsymbol{A}_w^b$ being the torque distribution matrix [11] mapping the spin axis of each reaction wheel to Cartesian space, and $\boldsymbol{A}_w^{b\,*}$ being the *Moore Penrose pseudoinverse* of $\boldsymbol{A}_w^b$. The inertia of the reaction wheels along the spin-axis make up the diagonal matrix $\boldsymbol{I}_{RW}^w$.

$$\boldsymbol{h}_{RW}^{b} = \boldsymbol{A}_{w}^{b}\boldsymbol{I}_{RW}^{w}\boldsymbol{A}_{w}^{b\,*}\boldsymbol{\omega}_{i\ b}^{b} + \boldsymbol{A}_{w}^{b}\boldsymbol{I}_{RW}^{w}\boldsymbol{\omega}_{b\ w}^{w} \tag{3.1a}$$

$$= \boldsymbol{A}_{w}^{b}\boldsymbol{I}_{RW}^{w}\boldsymbol{A}_{w}^{b\,*}\left(\boldsymbol{\omega}_{i\ b}^{b} + \boldsymbol{A}_{w}^{b}\boldsymbol{\omega}_{b\ w}^{w}\right) \tag{3.1b}$$

$$= \boldsymbol{A}_{w}^{b}\boldsymbol{I}_{RW}^{w}\boldsymbol{A}_{w}^{b\,*}\boldsymbol{\omega}_{i\ w}^{b} \tag{3.1c}$$

The dynamic relationship between the total moment of the reaction wheels, the angular velocities of the satellite body and reaction wheels, and the applied torque to the reaction wheels are found using the Transport Theorem and Euler's equations for rigid body rotations, and is presented in Equation (3.2).

$$\frac{^{i}d}{dt}\boldsymbol{h}_{RW}^{b} = \frac{^{b}d}{dt}\boldsymbol{h}_{RW}^{b} + \boldsymbol{\omega}_{i\ w}^{b} \times \boldsymbol{h}_{RW}^{b} \tag{3.2a}$$

$$= \boldsymbol{A}_{w}^{b}\boldsymbol{I}_{RW}^{w}\boldsymbol{A}_{w}^{b\,*}\frac{^{b}d}{dt}\boldsymbol{\omega}_{i\ w}^{b} + \boldsymbol{\omega}_{i\ w}^{b} \times \boldsymbol{A}_{w}^{b}\boldsymbol{I}_{RW}^{w}\boldsymbol{A}_{w}^{b\,*}\boldsymbol{\omega}_{i\ w}^{b} \tag{3.2b}$$

$$= \boldsymbol{A}_{w}^{b}\boldsymbol{I}_{RW}^{w}\boldsymbol{A}_{w}^{b\,*}\frac{^{b}d}{dt}\boldsymbol{\omega}_{i\ w}^{b} + \boldsymbol{A}_{w}^{b}\boldsymbol{\omega}_{i\ w}^{w} \times \boldsymbol{A}_{w}^{b}\boldsymbol{I}_{RW}^{w}\boldsymbol{\omega}_{i\ w}^{w} \tag{3.2c}$$

$$= \boldsymbol{A}_{w}^{b}\boldsymbol{I}_{RW}^{w}\boldsymbol{A}_{w}^{b\,*}\frac{^{b}d}{dt}\boldsymbol{\omega}_{i\ w}^{b} \tag{3.2d}$$

$$= \boldsymbol{A}_{w}^{b}\boldsymbol{I}_{RW}^{w}\boldsymbol{A}_{w}^{b\,*}\left(\frac{^{b}d}{dt}\boldsymbol{\omega}_{i\ b}^{b} + \boldsymbol{A}_{w}^{b}\frac{^{w}d}{dt}\boldsymbol{\omega}_{b\ w}^{w}\right) \tag{3.2e}$$

$$= \boldsymbol{A}_{w}^{b}\boldsymbol{\tau}_{u}^{w} \tag{3.2f}$$

In Equation (3.2c), the assumption that the weight and dimensions of all reaction wheels are equal is applied. In this case, the inertia matrix of the reaction wheels in the wheel frame can be replaced by a scalar multiplied by the identity matrix:

$\boldsymbol{I}_{RW}^{w} = \sigma \mathbb{I}_{n\times n}$. This leads to the cancellation of the cross product term, as the angular velocity vectors are parallel:

$$\begin{aligned}
\boldsymbol{A}_{w}^{b}\boldsymbol{\omega}_{i\ w}^{w} \times \boldsymbol{A}_{w}^{b}\boldsymbol{I}_{RW}^{w}\boldsymbol{\omega}_{i\ w}^{w} &= \boldsymbol{A}_{w}^{b}\boldsymbol{\omega}_{i\ w}^{w} \times \boldsymbol{A}_{w}^{b}\sigma\mathbb{I}_{n\times n}\boldsymbol{\omega}_{i\ w}^{w} && \text{(3.3a)}\\
&= \boldsymbol{A}_{w}^{b}\boldsymbol{\omega}_{i\ w}^{w} \times \sigma\boldsymbol{A}_{w}^{b}\boldsymbol{\omega}_{i\ w}^{w} && \text{(3.3b)}\\
&= \sigma\left(\boldsymbol{\omega}_{i\ w}^{b} \times \boldsymbol{\omega}_{i\ w}^{b}\right) && \text{(3.3c)}\\
&= 0 && \text{(3.3d)}
\end{aligned}$$

Rearranging Equation (3.2e) and Equation (3.2f), the expression for the reaction wheels dynamics is derived in Equation (3.4).

$$\frac{{}^{w}d}{dt}\boldsymbol{\omega}_{b\ w}^{w} = {\boldsymbol{I}_{RW}^{w}}^{-1}\boldsymbol{\tau}_{u}^{w} - \boldsymbol{A}_{w}^{b} * \frac{{}^{b}d}{dt}\boldsymbol{\omega}_{i\ b}^{b} \tag{3.4}$$

The power consumption of the reaction wheels is based on the model described in section 2.3.1, found in chapter 2 *Background Theory*. The power consumption is linearized as a function of the acceleration around a specified operating point ω_0, as defined in Equation (3.5). For the simulations, the operating point is chosen as the reference reaction wheel velocity.

$$P_{RW} = \frac{|\omega_0|\, I_{RW}}{\eta_0}\left|\frac{d}{dt}\omega_{RW}\right| \tag{3.5}$$

3.3 Magnetorquer

The torque produced by the magnetorquer is given by the cross product between the magnetic dipole moment, $\boldsymbol{M}^b$, and the Earth's magnetic field, $\boldsymbol{B}^b_{Earth}$, as defined in Equation (3.6) [19]. A consequence of this is that torque can only be produced in directions perpendicular to Earth's magnetic field at a given location.

$$\boldsymbol{\tau}^b_{MTQ} = \boldsymbol{M}^b \times \boldsymbol{B}^b_{Earth} \tag{3.6}$$

3.4 Propulsion

The propulsion system on the satellite consists of several thrusters mounted on the satellite body, which produce force in specified directions. This results in both a force and torque being applied to the satellite. The force acting from the propulsion on the satellite in the Earth-Centered Inertial frame is given in Equation (3.7).

$$\boldsymbol{F}^i_T = -\mathbf{R}^i_{body} \sum_k \boldsymbol{f}^b_k \tag{3.7}$$

The torque on the satellite produced by the propulsion unit is denoted $\boldsymbol{\tau}_T$. The force produced by the propulsion units, $\boldsymbol{f}^b_T$, is translated into a torque acting on the satellite by cross multiplication with the thrust arm, $\boldsymbol{l}^b_t$, as given in Equation (3.8). The thrust arm is time-dependent as a result of the satellite's center of mass moving when the propellant is consumed.

$$\boldsymbol{\tau}_T^b = -\sum_k \left[\boldsymbol{l}_k^b(t) \times \boldsymbol{f}_k^b \right] \tag{3.8}$$

To be fully actuated, a satellite needs at least six propulsion units, with the force vectors aligned along all three Cartesian axes, in both positive and negative directions.

Propellant consumption is related to the force output through the *specific impulse* value, denoted I_{sp}. The specific impulse is defined in Equation (3.9) [5], in which F_T is the force output of the thruster, $\frac{d}{dt}m_p$ is the propellant mass flow, and g_0 is the standard acceleration due to Earth's gravity. The unit of the specific impulse is *seconds*.

$$I_{sp} = \frac{F_T^i}{\frac{d}{dt}(m_p)\, g_0} \tag{3.9}$$

The propellant mass flow rate is found by rearranging the expression for the specific impulse, which gives Equation (3.10):

$$\frac{d}{dt}m_p = \frac{F_T}{I_{sp} g_0} \tag{3.10}$$

3.5 Satellite Dynamics

In this section, the equations of motion for the satellite are derived. The translational dynamics are derived in subsection 3.5.1 *Position*, and the rotational dynamics in subsection 3.5.2 *Attitude*. Subsection 3.5.3 *Center of Mass* presents the dynamics used to model the satellite center of mass, and subsection 3.5.4

Inertia presents the dynamics of the satellite inertia.

3.5.1 Position

The translational motion of the satellite is governed by Newton's Second Law of Motion, given in Equation (3.11). In this equation, $\boldsymbol{F}^i$ is the force applied to an object, $\boldsymbol{p}^i$ is the linear momentum of that object in an inertial frame, and $\boldsymbol{m}$ and $\boldsymbol{v}^i$ are the mass and velocity of the object, respectively.

$$\boldsymbol{F}^i = \sum_k \boldsymbol{f}_k^i = {}^i\frac{d}{dt}\boldsymbol{p}^i = {}^i\frac{d}{dt}\left(m\boldsymbol{v}^i\right) \tag{3.11}$$

When the satellite mass varies with time, the satellite's translational motion is described as in Equation (3.12).

$$\begin{aligned}
\boldsymbol{F}_{tot}^i &= {}^i\frac{d}{dt}\boldsymbol{p}_{sat}^i && \text{(3.12a)}\\
&= {}^i\frac{d}{dt}\left(m_{sat}\boldsymbol{v}_{sat}^i\right) && \text{(3.12b)}\\
&= \frac{d}{dt}\left(m_{sat}\right)\boldsymbol{v}_{sat}^i + m_{sat}\,{}^i\frac{d}{dt}\left(\boldsymbol{v}_{sat}^i\right) && \text{(3.12c)}\\
&= \frac{d}{dt}\left(m_{sat}\right)\boldsymbol{v}_{sat}^i + m_{sat}\boldsymbol{a}_{sat}^i && \text{(3.12d)}
\end{aligned}$$

The resulting satellite acceleration in the Earth-Centered Inertial frame (see section 2.1.1) is described in Equation 3.13. This is the equation used to model

the dynamics of the satellite position, with the resulting acceleration given by $\boldsymbol{a}^i_{sat}$. The acceleration due to the gravitational pull is $\boldsymbol{a}^i_{grav}$ (section 2.1.2), the satellite mass is denoted m_{sat}, and the satellite velocity is denoted $\boldsymbol{v}^i_{sat}$. $\boldsymbol{F}^i_{J_2}$ represents the J_2 perturbing force (section 2.2.1), $\boldsymbol{F}^i_{drag}$ the atmospheric drag force (section 2.2.3), and $\boldsymbol{F}^i_{srp}$ the force resulting from the solar radiation pressure (section 2.2.4). The force from the thruster actuation is given by $\boldsymbol{F}^i_T$ (section 3.4).

$$\begin{aligned}\boldsymbol{a}^i_{sat} &= \boldsymbol{a}^i_{grav} + \frac{1}{m_{sat}}\left[\boldsymbol{F}^i_{tot} - \frac{d}{dt}\left(m_{sat}\right)\boldsymbol{v}^i_{sat}\right] \\ &= \boldsymbol{a}^i_{grav} + \frac{1}{m_{sat}}\left[\boldsymbol{F}^i_{J_2} + \boldsymbol{F}^i_T + \boldsymbol{F}^i_{drag} + \boldsymbol{F}^i_{srp} - \frac{\boldsymbol{F}^i_T}{I_{sp}\cdot g_0}\boldsymbol{v}^i_{sat}\right]\end{aligned} \tag{3.13}$$

3.5.2 Attitude

The attitude of the satellite is represented with a unit quaternion $\boldsymbol{q}_{ib}$ describing the rotation from the inertia frame to the satellite body frame. The quaternion dynamical equation is given in (3.14) [7].

$$\frac{^i d}{dt}\boldsymbol{q}_{ib} = \frac{1}{2}\boldsymbol{T}\left(\boldsymbol{q}_{ib}\right)\boldsymbol{\omega}^b_{i\ b}, \qquad \boldsymbol{T} = \begin{bmatrix} -\epsilon_1 & -\epsilon_2 & -\epsilon_3 \\ \eta & -\epsilon_3 & \epsilon_2 \\ \epsilon_3 & \eta & -\epsilon_1 \\ -\epsilon_2 & \epsilon_1 & \eta \end{bmatrix} \tag{3.14}$$

The system consisting of the satellite body and reaction wheels exchange moment internally, and external torques applied to the satellite affect the total moment of the system. The total moment of the satellite system consists of the moment

of the satellite body and the moment of the reaction wheels and is given in Equation (3.15). The combined inertia of the satellite body and reaction wheels is denoted $\boldsymbol{I}^b_{sys} = \boldsymbol{I}^b_{sat} + \boldsymbol{A}^b_w \boldsymbol{I}^w_{RW} \boldsymbol{A}^{b\ *}_w$.

$$\begin{aligned}
\boldsymbol{h}^b_{sys} &= \boldsymbol{h}^b_{sat} + \boldsymbol{h}^b_{RW} && \text{(3.15a)}\\
&= \boldsymbol{I}^b_{sat}\boldsymbol{\omega}^{b\ b}_{i} + \boldsymbol{A}^b_w \boldsymbol{I}^w_{RW} \boldsymbol{A}^{b\ *}_w \boldsymbol{\omega}^{b\ b}_{i} + \boldsymbol{A}^b_w \boldsymbol{I}^w_{RW} \boldsymbol{\omega}^{w\ w}_{b} && \text{(3.15b)}\\
&= \boldsymbol{I}^b_{sys}\boldsymbol{\omega}^{b\ b}_{i} + \boldsymbol{A}^b_w \boldsymbol{I}^w_{RW} \boldsymbol{\omega}^{w\ w}_{b} && \text{(3.15c)}
\end{aligned}$$

The dynamic equation for the satellite system's total momentum is derived using the Transport Theorem and Euler's equations for rigid body rotations. The relation between system angular acceleration and torque applied to the reaction wheels was found in section 3.2.

The satellite angular momentum dynamics with time-varying satellite inertia becomes:

$$\begin{aligned}
\frac{^i d}{dt}\boldsymbol{h}^b_{sys} &= \frac{^b d}{dt}\boldsymbol{h}^b_{sys} + \boldsymbol{\omega}^{b\ b}_{i} \times \boldsymbol{h}^b_{sys} && \text{(3.16a)}\\
&= \frac{^b d}{dt}\left(\boldsymbol{I}^b_{sys}\boldsymbol{\omega}^{b\ b}_{i} + \boldsymbol{A}^b_w \boldsymbol{I}^w_{RW} \boldsymbol{\omega}^{w\ w}_{b}\right) + \boldsymbol{\omega}^{b\ b}_{i} \times \boldsymbol{h}^b_{sys} && \text{(3.16b)}\\
&= \frac{^b d}{dt}\left(\boldsymbol{I}^b_{sys}\right)\boldsymbol{\omega}^{b\ b}_{i} + \boldsymbol{I}^b_{sys}\frac{^b d}{dt}\left(\boldsymbol{\omega}^{b\ b}_{i}\right) && \text{(3.16c)}\\
&\quad + \boldsymbol{\omega}^{b\ b}_{i} \times \boldsymbol{h}^b_{sys} + \boldsymbol{A}^b_w \boldsymbol{I}^w_{RW}\frac{^w d}{dt}\left(\boldsymbol{\omega}^{w\ w}_{b}\right)
\end{aligned}$$

$$= \frac{^b d}{dt}\left(\boldsymbol{I}_{sat}^b\right)\boldsymbol{\omega}_{i\ b}^{b} + \boldsymbol{I}_{sat}^b \frac{^b d}{dt}\left(\boldsymbol{\omega}_{i\ b}^{b}\right) \tag{3.16d}$$
$$+ \boldsymbol{\omega}_{i\ b}^{b} \times \boldsymbol{h}_{sys}^b + \boldsymbol{A}_w^b \boldsymbol{\tau}_{RW}^w$$
$$= \boldsymbol{\tau}_{MTQ}^b + \boldsymbol{\tau}_T^b + \boldsymbol{\tau}_{dist}^b \tag{3.16e}$$

Equation (3.16d) uses the fact that the reaction wheel inertia matrix is constant and is inserted with Equation (3.2e), which relates the reaction wheel torque to the angular velocities of the satellite and the reaction wheels.

Rearranging Equation (3.16), we get an expression for the rate of the satellite angular velocity, provided in Equation (3.17).

$$\frac{^b d}{dt}\boldsymbol{\omega}_{i\ b}^{b} = {\boldsymbol{I}_{sat}^b}^{-1}\left(-\frac{^b d}{dt}\left(\boldsymbol{I}_{sat}^b\right)\boldsymbol{\omega}_{i\ b}^{b} - \boldsymbol{\omega}_{i\ b}^{b} \times \boldsymbol{h}_{sys}^b \right. \tag{3.17a}$$
$$\left. - \boldsymbol{A}_w^b \boldsymbol{\tau}_{RW}^w + \boldsymbol{\tau}_{MTQ}^b + \boldsymbol{\tau}_T^b + \boldsymbol{\tau}_{dist}^b\right)$$

$$= {\boldsymbol{I}_{sat}^b}^{-1}\left(-\frac{^b d}{dt}\left(\boldsymbol{I}_{sat}^b\right)\boldsymbol{\omega}_{i\ b}^{b} - \boldsymbol{\omega}_{i\ b}^{b} \times \boldsymbol{h}_{sys}^b \right.$$
$$\left. - \boldsymbol{A}_w^b \boldsymbol{I}_{RW}^w {\boldsymbol{A}_w^b}^* \left(\frac{^b d}{dt}\boldsymbol{\omega}_{i\ b}^{b} + \boldsymbol{A}_w^b \frac{^w d}{dt}\boldsymbol{\omega}_{b\ w}^{w}\right) + \boldsymbol{\tau}_{MTQ}^b + \boldsymbol{\tau}_T^b + \boldsymbol{\tau}_{dist}^b\right) \tag{3.17b}$$

$$= \left(\boldsymbol{I}_{sat}^b + \boldsymbol{A}_w^b \boldsymbol{I}_{RW}^w {\boldsymbol{A}_w^b}^*\right)^{-1}\left(-\frac{^b d}{dt}\left(\boldsymbol{I}_{sat}^b\right)\boldsymbol{\omega}_{i\ b}^{b} - \boldsymbol{\omega}_{i\ b}^{b} \times \boldsymbol{h}_{sys}^b \right. \tag{3.17c}$$
$$\left. - \boldsymbol{A}_w^b \boldsymbol{I}_{RW}^w \frac{^w d}{dt}\boldsymbol{\omega}_{b\ w}^{w} + \boldsymbol{\tau}_{MTQ}^b + \boldsymbol{\tau}_T^b + \boldsymbol{\tau}_{dist}^b\right)$$

3.5.3 Center of Mass

The mass of the satellite consists of the mass of the propellant, m_{prop}, and the mass of the rest of the satellite, m_{body}. For a system consisting of k propellant containers, the total mass is given by Equation (3.18).

$$m_{sat} = m_{body} + \sum_{k} m_{prop_k} = m_{body} + m_{prop} \tag{3.18}$$

It is assumed that the mass of propellant at launch is m_{prop_0} and that the satellite's center of mass in the structural frame at launch is $\boldsymbol{c}^s_{m_0}$. The relation in Equation (3.20) for the center of mass of the satellite body, $\boldsymbol{c}^s_{body}$, is then found by decomposing the initial center of mass at launch (3.19), and rearranging the equation. The center of mass of the satellite body, $\boldsymbol{c}^s_{body}$, is assumed to remain constant in the simulations.

$$\boldsymbol{c}^s_{m_0} = \boldsymbol{c}^s_{body}\frac{m_{body}}{m_{sat_0}} + \boldsymbol{c}^s_{prop}\frac{m_{prop_0}}{m_{sat_0}} \tag{3.19}$$

$$\boldsymbol{c}^s_{body} = \boldsymbol{c}^s_{m_0}\frac{m_{sat_0}}{m_{body}} - \boldsymbol{c}^s_{prop}\frac{m_{prop_0}}{m_{body}} \tag{3.20}$$

With a known and constant center of mass for the satellite body, the calculation of the center of mass for the whole satellite becomes dependent only on the mass and location of the propellant. The expression for the center of mass of the satellite is given in Equation (3.21), with its derivative in time given by Equation (3.22).

$$\begin{aligned} \boldsymbol{c}_m^s(t) &= \boldsymbol{c}_{body}^s \frac{m_{body}}{m_{sat}(t)} + \sum_k \boldsymbol{c}_{prop_k}^s \frac{m_{prop_k}(t)}{m_{sat}(t)} \\ &= \boldsymbol{c}_{body}^s \frac{m_{body}}{m_{sat}(t)} + \boldsymbol{c}_{prop}^s \frac{m_{prop}(t)}{m_{sat}(t)} \end{aligned} \tag{3.21}$$

$$\begin{aligned} \frac{^s d}{dt}\boldsymbol{c}_m^s(t) &= \left(-\boldsymbol{c}_{body}^s \frac{m_{body}}{m_{sat}^2(t)} + \boldsymbol{c}_{prop}^s \frac{1}{m_{sat}(t)} \right. \\ &\qquad \left. - \boldsymbol{c}_{prop}^s \frac{m_{prop}(t)}{m_{sat}^2(t)} \right) \frac{d}{dt} m_{prop} \\ &= \sum_k \left(-\boldsymbol{c}_{body}^s \frac{m_{body}}{m_{sat}^2(t)} + \boldsymbol{c}_{prop_k}^s \frac{1}{m_{sat}(t)} \right. \\ &\qquad \left. - \boldsymbol{c}_{prop_k}^s \frac{m_{prop_k}(t)}{m_{sat}^2(t)} \right) \frac{d}{dt} m_{prop_k} \end{aligned} \tag{3.22}$$

3.5.4 Inertia

The satellite inertia matrix is calculated in the body frame using the time-varying propellant density. The moments of inertia are denoted I_i, while the products of inertia are denoted I_{ij}.

In the following derivations, ρ_{body} is the mass density of the satellite body, and ρ_{prop} is the mass density of the thruster propellant. The density of the satellite body is assumed to be constant, while the mass density of the propellant is dependent on the consumption, and thus time-varying. The variables i, j, and k represent the axes of the body frame and are replaces with the satellite's x, y, and z values corresponding to the elements of the inertia matrix of interest.

The expression for the moment of inertia is given in Equation (3.23), and the product of inertia in Equation (3.24). The time-derivatives of these are given in Equation (3.25) and Equation (3.26), respectively.

$$
\begin{aligned}
I_i^c(t) &= \int_{V_{body}^c} \left(j^2+k^2\right)\ \rho_{body}\ dV + \int_{V_{prop}^c} \left(j^2+k^2\right)\ \rho_{prop}(t)\ \ dV \qquad (3.23)\\
&= \frac{\rho_{body}}{3} d_i d_k \left[\left(j^s_{ub_{body}} - j^s_{com}(t)\right)^3 - \left(j^s_{lb_{body}} - j^s_{com}(t)\right)^3\right]\\
&\quad + \frac{\rho_{body}}{3} d_i d_j \left[\left(k^s_{ub_{body}} - k^s_{com}(t)\right)^3 - \left(k^s_{lb_{body}} - k^s_{com}(t)\right)^3\right]\\
&\quad + \frac{\rho_{prop}(t)}{3}\left(i^s_{ub_{prop}} - i^s_{lb_{prop}}\right)\left(j^s_{ub_{prop}} - j^s_{lb_{prop}}\right)\\
&\qquad \left[\left(k^s_{ub_{prop}} - k^s_{com}(t)\right)^3 - \left(k^s_{lb_{prop}} - k^s_{com}(t)\right)^3\right]\\
&\quad + \frac{\rho_{prop}(t)}{3}\left(i^s_{ub_{prop}} - i^s_{lb_{prop}}\right)\left(k^s_{ub_{prop}} - k^s_{lb_{prop}}\right)\\
&\qquad \left[\left(j^s_{ub_{prop}} - j^s_{com}(t)\right)^3 - \left(j^s_{lb_{prop}} - j^s_{com}(t)\right)^3\right]
\end{aligned}
$$

$$I^c_{ij}(t) = I^c_{ji}(t) = \int_{V^c_{body}} ij\ \rho_{body} dV + \int_{V^c_{prop}} ij\ \rho_{prop}(t)\ dV \tag{3.24}$$

$$\begin{aligned}
&= \frac{\rho_{body}}{4} \left({i^s_{ub_{body}}}^2 - {i^s_{lb_{body}}}^2 + 2\left(i^s_{lb_{body}} - i^s_{ub_{body}}\right) i^s_{com}(t) \right) \\
&\qquad \left({j^s_{ub_{body}}}^2 - {j^s_{lb_{body}}}^2 + 2\left(j^s_{lb_{body}} - j^s_{ub_{body}}\right) j^s_{com}(t) \right) \\
&\qquad \left(k^s_{ub_{body}} - k^s_{lb_{body}} \right) \\
&\quad + \frac{\rho_{prop}(t)}{4} \left({i^s_{ub_{prop}}}^2 - {i^s_{lb_{prop}}}^2 + 2\left(i^s_{lb_{prop}} - i^s_{ub_{prop}}\right) i^s_{com}(t) \right) \\
&\qquad \left({j^s_{ub_{prop}}}^2 - {j^s_{lb_{prop}}}^2 + 2\left(j^s_{lb_{prop}} - j^s_{ub_{prop}}\right) j^s_{com}(t) \right) \\
&\qquad \left(k^s_{ub_{prop}} - k^s_{lb_{prop}} \right)
\end{aligned}$$

$$\frac{d}{dt}I_i^c(t) = \rho_{body} d_i d_k \left[{j^s_{lb_{body}}}^2 - {j^s_{ub_{body}}}^2 + 2j^s_{com}(t)\left(j^s_{ub_{body}} - j^s_{lb_{body}}\right)\right] \frac{d}{dt}\, j^s_{com}(t)$$

$$+ \rho_{body} d_i d_j \left[{k^s_{lb_{body}}}^2 - {k^s_{ub_{body}}}^2 \right.$$

$$\left. + 2k^s_{com}(t)\left(k^s_{ub_{body}} - k^s_{lb_{body}}\right)\right] \frac{d}{dt}\, k^s_{com}(t)$$

$$+ \frac{1}{3}\left(i^s_{ub_{prop}} - i^s_{lb_{prop}}\right)\left(k^s_{ub_{prop}} - k^s_{lb_{prop}}\right)$$

$$\left[\left(j^s_{ub_{prop}} - j^s_{com}(t)\right)^3 - \left(j^s_{lb_{prop}} - j^s_{com}(t)\right)^3\right] \frac{d}{dt}\, \rho_{prop}(t)$$

$$+ \rho_{prop}(t)\left(i^s_{ub_{prop}} - i^s_{lb_{prop}}\right)\left(k^s_{ub_{prop}} - k^s_{lb_{prop}}\right)$$

$$\left[{j^s_{lb_{prop}}}^2 - {j^s_{ub_{prop}}}^2 + 2j^s_{com}(t)\left(j^s_{ub_{prop}} - j^s_{lb_{prop}}\right)\right] \frac{d}{dt}\, j^s_{com}(t)$$

$$+ \frac{1}{3}\left(i^s_{ub_{prop}} - i^s_{lb_{prop}}\right)\left(j^s_{ub_{prop}} - j^s_{lb_{prop}}\right)$$

$$\left[\left(k^s_{ub_{prop}} - k^s_{com}(t)\right)^3 - \left(k^s_{lb_{prop}} - k^s_{com}(t)\right)^3\right] \frac{d}{dt}\, \rho_{prop}(t)$$

$$+ \rho_{prop}(t)\left(i^s_{ub_{prop}} - i^s_{lb_{prop}}\right)\left(j^s_{ub_{prop}} - j^s_{lb_{prop}}\right)$$

$$\left[{k^s_{lb_{prop}}}^2 - {k^s_{ub_{prop}}}^2 + 2k^s_{com}(t)\left(k^s_{ub_{prop}} - k^s_{lb_{prop}}\right)\right] \frac{d}{dt}\, k^s_{com}(t)$$

(3.25)

$$
\begin{aligned}
\frac{d}{dt} I_{ij}^{c}(t) = & \frac{\rho_{body}}{2} \left(i_{lb_{body}}^{s} - i_{ub_{body}}^{s} \right) \\
& \left({j_{ub_{body}}^{s}}^{2} - {j_{lb_{body}}^{s}}^{2} + 2 \left(j_{lb_{body}}^{s} - j_{ub_{body}}^{s} \right) j_{com}^{s}(t) \right) \\
& \left(k_{ub_{body}}^{s} - k_{lb_{body}}^{s} \right) \frac{d}{dt} \; i_{com}^{s}(t) \\
& + \frac{\rho_{body}}{2} \left(j_{lb_{body}}^{s} - j_{ub_{body}}^{s} \right) \\
& \left({i_{ub_{body}}^{s}}^{2} - {i_{lb_{body}}^{s}}^{2} + 2 \left(i_{lb_{body}}^{s} - i_{ub_{body}}^{s} \right) i_{com}^{s}(t) \right) \\
& \left(k_{ub_{body}}^{s} - k_{lb_{body}}^{s} \right) \frac{d}{dt} \; j_{com}^{s}(t) \\
& + \frac{\rho_{prop}(t)}{2} \left(i_{lb_{prop}}^{s} - i_{ub_{prop}}^{s} \right) \\
& \left({j_{ub_{prop}}^{s}}^{2} - {j_{lb_{prop}}^{s}}^{2} + 2 \left(j_{lb_{prop}}^{s} - j_{ub_{prop}}^{s} \right) j_{com}^{s}(t) \right) \\
& \left(k_{ub_{prop}}^{s} - k_{lb_{prop}}^{s} \right) \frac{d}{dt} \; i_{com}^{s}(t) \\
& + \frac{\rho_{prop}(t)}{2} \left(j_{lb_{prop}}^{s} - j_{ub_{prop}}^{s} \right) \\
& \left({i_{ub_{prop}}^{s}}^{2} - {i_{lb_{prop}}^{s}}^{2} + 2 \left(i_{lb_{prop}}^{s} - i_{ub_{prop}}^{s} \right) i_{com}^{s}(t) \right) \\
& \left(k_{ub_{prop}}^{s} - k_{lb_{prop}}^{s} \right) \frac{d}{dt} \; j_{com}^{s}(t) \\
& + \frac{1}{4} \left({i_{ub_{prop}}^{s}}^{2} - {i_{lb_{prop}}^{s}}^{2} + 2 \left(i_{lb_{prop}}^{s} - i_{ub_{prop}}^{s} \right) i_{com}^{s}(t) \right) \\
& \left({j_{ub_{prop}}^{s}}^{2} - {j_{lb_{prop}}^{s}}^{2} + 2 \left(j_{lb_{prop}}^{s} - j_{ub_{prop}}^{s} \right) j_{com}^{s}(t) \right) \\
& \left(k_{ub_{prop}}^{s} - k_{lb_{prop}}^{s} \right) \frac{d}{dt} \; \rho_{prop}(t)
\end{aligned}
\tag{3.26}
$$

Chapter 4

Controller Design

This chapter presents the attitude controllers that have been developed. The controllers are derived based on the satellite model presented in chapter 3, *Satellite Model*. The first section, 4.1, presents the Proportional-Derivative controller, and the second section, 4.2, presents the Adaptive Model Predictive Controller.

4.1 Proportional-Derivative Controller

This section presents the developed PD controller. First, the torque command is derived based on the error variables. Then, in subsection 4.1.1, the control allocation based on the reaction wheels actuator is described.

For the satellite body we define the reference orientation quaternion $\boldsymbol{q}_{Ref}$, reference rotational velocity $\boldsymbol{\omega}_{Ref}$, and reference rotational acceleration $\boldsymbol{\alpha}_{Ref}$. The

reference deviation variables are denoted with subscript e and are given in Equation (4.1).

$$\boldsymbol{q}_e = \boldsymbol{q}_{Ref}^{-1} \otimes \boldsymbol{q}_{Curr} = \begin{bmatrix} \eta_e \\ \boldsymbol{\epsilon}_e \end{bmatrix} \tag{4.1a}$$

$$\boldsymbol{\omega}_e = \boldsymbol{\omega}_{Curr} - \boldsymbol{\omega}_{Ref} \tag{4.1b}$$

$$\boldsymbol{\alpha}_e = \boldsymbol{\alpha}_{Curr} - \boldsymbol{\alpha}_{Ref} \tag{4.1c}$$

The control law regulating the satellite attitude response is defined as in Equation (4.2). Similarly, the control law for angular velocity tracking is defined in Equation (4.3).

$$\boldsymbol{\tau}_{cmd_a}^b = -K_p \boldsymbol{I}_{sat}^b \boldsymbol{\epsilon}_e - K_d \boldsymbol{I}_{sat}^b \boldsymbol{\omega}_e \tag{4.2}$$

$$\boldsymbol{\tau}_{cmd_\omega}^b = -K_p \boldsymbol{I}_{sat}^b \boldsymbol{\omega}_e - K_d \boldsymbol{I}_{sat}^b \boldsymbol{\alpha}_e \tag{4.3}$$

4.1.1 Reaction Wheels

This subsection introduces the control allocation method for the reaction wheels and presents the resulting satellite dynamics based on the implemented controller.

The control allocation is done as presented in Equation (4.4), using the Moore-Penrose pseudo-inverse of the torque distribution matrix $\boldsymbol{A}_w^b$, indicated with superscript $*$. A maximum acceleration and velocity value constrain the reaction wheels.

$$\frac{^w d}{dt}\boldsymbol{\omega}^w = \boldsymbol{A}_w^{b\,*}\boldsymbol{I}_{RW}^{-1}\boldsymbol{\tau}_{cmd}^b \tag{4.4}$$

The torque produced by the reaction wheels on the satellite in the body frame is given by Equation (4.5):

$$\boldsymbol{\tau}_{RW}^b = -\boldsymbol{A}_w^b\boldsymbol{\tau}_u^w \tag{4.5}$$

Setting the torque produced by the reaction wheels equal to the torque given by the PD control law in Equation (4.2), and inserting this in the satellite dynamics of Equation (3.17a), results in the following satellite attitude-behavior:

$$\begin{aligned}\frac{^b d}{dt}\boldsymbol{\omega}_{i\ b}^b = &-K_{p_{RW}}\boldsymbol{\epsilon}_e^b - K_{d_{RW}}\boldsymbol{\omega}_e^b - K_{dd_{RW}}\boldsymbol{\alpha}_e^b \\ &+ \boldsymbol{I}_{sat}^{b\ -1}\left[-\frac{^b d}{dt}\left(\boldsymbol{I}_{sat}^b\right)\boldsymbol{\omega}_{i\ b}^b - \boldsymbol{\omega}_{i\ b}^b \times \boldsymbol{h}_{sys}^b + \boldsymbol{\tau}_{MTQ}^b + \boldsymbol{\tau}_T^b + \boldsymbol{\tau}_{dist}^b\right]\end{aligned} \tag{4.6}$$

4.2 Adaptive Model Predictive Controller

The adaptive MPC is designed to find an optimal control input making the satellite following the desired reference trajectory. The controller minimizes a quadratic cost function over a given prediction horizon subject to a set of constraints, based on the work by Hovd [9]. The adaptive update rule of the controller linearizes the attitude dynamics around the current state of the satellite.

The principle workings of the controller is presented in Equation (4.7), with $\boldsymbol{x}$ and $\boldsymbol{u}$ being the satellite state vector and the control input vector, respectively. The set $\mathbb{T}$ contains the control input indexes that inhibit integer values, which correspond to the control signal indexes assigned to the propulsion system.

$$\begin{aligned} \underset{\boldsymbol{u}}{minimize} \quad & \boldsymbol{f}\left(\boldsymbol{x}, \boldsymbol{u}\right) \\ \text{subject to} \quad & \boldsymbol{x}_0 \text{ given}, \\ & \boldsymbol{A}\boldsymbol{x} \leq \boldsymbol{b}, \\ & \boldsymbol{u}_{lb} \leq \boldsymbol{u} \leq \boldsymbol{u}_{ub}, \\ & \boldsymbol{u}_i \text{ integer}, \ i \in \mathbb{T} \end{aligned} \tag{4.7}$$

The satellite state vector $\boldsymbol{x}$ and control input vector $\boldsymbol{u}$ consist of the data presented in Equation (4.8).

$$\boldsymbol{x} = \begin{bmatrix} \boldsymbol{q}_{sat}^{ECI} \\ \boldsymbol{\omega}_{sat}^{b} \\ \boldsymbol{\omega}_{RW}^{w} \\ \boldsymbol{\rho}_{PROP} \end{bmatrix}, \quad \boldsymbol{u} = \begin{bmatrix} \boldsymbol{M}_{MTQ}^{ECI} \\ \frac{^w d}{dt}\boldsymbol{\omega}_{RW}^{w} \\ \boldsymbol{F}_{PROP}^{p} \end{bmatrix} \tag{4.8}$$

4.2.1 Satellite Dynamics Formulated for MPC

The system dynamics are reformulated to be dependent only on the actuator input u. This is accomplished by linearizing the dynamics around the current operating point of the satellite and using the superposition principle of linear systems. The unactuated system dynamics and effects of control input are modeled as presented in this subsection, based on the work by Hovd [9].

Two new variables are introduced, $\boldsymbol{\chi}$ and $\boldsymbol{\upsilon}$, which consists of the system state vector, $\boldsymbol{x}_i$, and control input, $\boldsymbol{u}_i$, for each timestep of the prediction horizon stacked on top of each other. The length of the prediction horizon is n. The unactuated system dynamics are collected in the term Γ, and the effects of the actuation input at a given timestep are modeled as a gain matrix Θ. The reformulated system is given in Equation (4.9).

$$\boldsymbol{\chi} = \Gamma \boldsymbol{x}_0 + \Theta \boldsymbol{\upsilon} = \boldsymbol{\chi}_0 + \Theta \boldsymbol{\upsilon}, \quad \boldsymbol{\chi} = \begin{bmatrix} \boldsymbol{x}_1 \\ \boldsymbol{x}_2 \\ \vdots \\ \boldsymbol{x}_n \end{bmatrix}, \ \boldsymbol{\upsilon} = \begin{bmatrix} \boldsymbol{u}_1 \\ \boldsymbol{u}_2 \\ \vdots \\ \boldsymbol{u}_n \end{bmatrix} \tag{4.9}$$

The reformulated system is based on the discretized satellite dynamics, on the form $\boldsymbol{x}_{i+1} = \boldsymbol{A}_d\boldsymbol{x}_i + \boldsymbol{B}_d\boldsymbol{u}_i$. The matrices Γ and Θ are thus given by Equation (4.10), in which n is the number of steps in the prediction horizon.

$$\Gamma = \begin{bmatrix} \boldsymbol{A}_d \\ \boldsymbol{A}_d^2 \\ \vdots \\ \boldsymbol{A}_d^n \end{bmatrix}, \quad \Theta = \begin{bmatrix} \boldsymbol{B}_d & \boldsymbol{0} & \cdots & \boldsymbol{0} & \boldsymbol{0} \\ \boldsymbol{A}_d\boldsymbol{B}_d & \boldsymbol{B}_d & \ddots & \vdots & \vdots \\ \vdots & \vdots & \ddots & \boldsymbol{0} & \boldsymbol{0} \\ \boldsymbol{A}_d^{n-2}\boldsymbol{B}_d & \boldsymbol{A}_d^{n-3}\boldsymbol{B}_d & \cdots & \boldsymbol{B}_d & \boldsymbol{0} \\ \boldsymbol{A}_d^{n-1}\boldsymbol{B}_d & \boldsymbol{A}_d^{n-2}\boldsymbol{B}_d & \cdots & \boldsymbol{A}_d\boldsymbol{B}_d & \boldsymbol{B}_d \end{bmatrix} \tag{4.10}$$

In the context of control, we are interested in making the satellite follow the desired state trajectory. This is formulated as an optimization problem by minimization of a deviation variable, $\boldsymbol{\chi}_{dev}$, defined in Equation (4.11).

$$\boldsymbol{\chi}_{dev} = \boldsymbol{\chi} - \begin{bmatrix} \boldsymbol{x}_{ref,1} \\ \boldsymbol{x}_{ref,2} \\ \vdots \\ \boldsymbol{x}_{ref,n} \end{bmatrix} = \boldsymbol{\chi} - \widetilde{\boldsymbol{x}}_{ref} \tag{4.11}$$

4.2.2 Cost Function

The cost function describes the optimal satellite behavior. It is formulated as a quadratic function with an additional absolute value term. It is designed to

penalize both deviations from the reference satellite attitude trajectory, momentum buildup in the reaction wheels, and excess use of the actuators.

$$\boldsymbol{f}\left(\boldsymbol{x},\boldsymbol{u}\right)=\sum_{i=1}^{n}\left(\boldsymbol{x}_i-\boldsymbol{x}_{ref,i}\right)^T\boldsymbol{Q}\left(\boldsymbol{x}_i-\boldsymbol{x}_{ref,i}\right)+\boldsymbol{u}_i^T\boldsymbol{P}\boldsymbol{u}_i+\boldsymbol{z}|\boldsymbol{u}_i| \tag{4.12}$$

The cost function takes the form given by Equation (4.12). The matrix $\boldsymbol{Q}$ is a diagonal matrix consisting of the weights related to reference trajectory deviation. The actuation weights are described by the diagonal matrix $\boldsymbol{P}$ and the row vector $\boldsymbol{z}$.

Using the superposition principle, and the formulation of the problem with υ as the free variable (see subsection 4.2.1), the cost function becomes:

$$\begin{aligned}
\boldsymbol{f}\left(\boldsymbol{\chi}_{dev},\boldsymbol{\upsilon}\right)&=\boldsymbol{\chi}_{dev}^T\widetilde{\boldsymbol{Q}}\boldsymbol{\chi}_{dev}+\boldsymbol{\upsilon}^T\widetilde{\boldsymbol{P}}\boldsymbol{\upsilon}+\widetilde{\boldsymbol{z}}|\boldsymbol{\upsilon}| && \text{(4.13a)}\\
&=\left(\boldsymbol{\chi}_0+\Theta\boldsymbol{\upsilon}-\widetilde{\boldsymbol{x}}_{ref}\right)^T\widetilde{\boldsymbol{Q}}\left(\boldsymbol{\chi}_0+\Theta\boldsymbol{\upsilon}-\widetilde{\boldsymbol{x}}_{ref}\right)+\boldsymbol{\upsilon}^T\widetilde{\boldsymbol{P}}\boldsymbol{\upsilon}+\widetilde{\boldsymbol{z}}|\boldsymbol{\upsilon}| && \text{(4.13b)}\\
&=\boldsymbol{\chi}_0^T\widetilde{\boldsymbol{Q}}\boldsymbol{\chi}_0+\boldsymbol{\upsilon}^T\Theta^T\widetilde{\boldsymbol{Q}}\boldsymbol{\chi}_0-\widetilde{\boldsymbol{x}}_{ref}^T\widetilde{\boldsymbol{Q}}\boldsymbol{\chi}_0+\boldsymbol{\chi}_0^T\widetilde{\boldsymbol{Q}}\Theta\boldsymbol{\upsilon}\\
&\quad+\boldsymbol{\upsilon}^T\Theta^T\widetilde{\boldsymbol{Q}}\Theta\boldsymbol{\upsilon}-\widetilde{\boldsymbol{x}}_{ref}^T\widetilde{\boldsymbol{Q}}\Theta\boldsymbol{\upsilon}-\boldsymbol{\chi}_0^T\widetilde{\boldsymbol{Q}}\widetilde{\boldsymbol{x}}_{ref} && \text{(4.13c)}\\
&\quad-\boldsymbol{\upsilon}^T\Theta^T\widetilde{\boldsymbol{Q}}\widetilde{\boldsymbol{x}}_{ref}+\widetilde{\boldsymbol{x}}_{ref}^T\widetilde{\boldsymbol{Q}}\widetilde{\boldsymbol{x}}_{ref}+\boldsymbol{\upsilon}^T\widetilde{\boldsymbol{P}}\boldsymbol{\upsilon}+\widetilde{\boldsymbol{z}}|\boldsymbol{\upsilon}|\\
&=\boldsymbol{\upsilon}^T\Theta^T\widetilde{\boldsymbol{Q}}\boldsymbol{\chi}_0+\boldsymbol{\chi}_0^T\widetilde{\boldsymbol{Q}}\Theta\boldsymbol{\upsilon}+\boldsymbol{\upsilon}^T\Theta^T\widetilde{\boldsymbol{Q}}\Theta\boldsymbol{\upsilon} && \text{(4.13d)}\\
&\quad-\widetilde{\boldsymbol{x}}_{ref}^T\widetilde{\boldsymbol{Q}}\Theta\boldsymbol{\upsilon}-\boldsymbol{\upsilon}^T\Theta^T\widetilde{\boldsymbol{Q}}\widetilde{\boldsymbol{x}}_{ref}+\boldsymbol{\upsilon}^T\widetilde{\boldsymbol{P}}\boldsymbol{\upsilon}+\widetilde{\boldsymbol{z}}|\boldsymbol{\upsilon}|\\
&=\boldsymbol{\upsilon}^T\left(\Theta^T\widetilde{\boldsymbol{Q}}\boldsymbol{\chi}_0-\Theta^T\widetilde{\boldsymbol{Q}}\widetilde{\boldsymbol{x}}_{ref}\right)+\left(\boldsymbol{\chi}_0^T\widetilde{\boldsymbol{Q}}\Theta-\widetilde{\boldsymbol{x}}_{ref}^T\widetilde{\boldsymbol{Q}}\Theta\right)\boldsymbol{\upsilon} && \text{(4.13e)}\\
&\quad+\boldsymbol{\upsilon}^T\left(\Theta^T\widetilde{\boldsymbol{Q}}\Theta+\widetilde{\boldsymbol{P}}\right)\boldsymbol{\upsilon}+\widetilde{\boldsymbol{z}}|\boldsymbol{\upsilon}|\\
&=2\left(\boldsymbol{\chi}_0^T\widetilde{\boldsymbol{Q}}\Theta-\widetilde{\boldsymbol{x}}_{ref}^T\widetilde{\boldsymbol{Q}}\Theta\right)\boldsymbol{\upsilon}+\boldsymbol{\upsilon}^T\left(\Theta^T\widetilde{\boldsymbol{Q}}\Theta+\widetilde{\boldsymbol{P}}\right)\boldsymbol{\upsilon}+\widetilde{\boldsymbol{z}}|\boldsymbol{\upsilon}| && \text{(4.13f)}
\end{aligned}$$

In Equation (4.13), the matrices $\widetilde{\boldsymbol{Q}}$ and $\widetilde{\boldsymbol{P}}$, which describe the cost over the whole prediction horizon, are formed by placing the cost matrices of a single timestep along the diagonal, as presented in Equation (4.14). Similarly, the vector $\widetilde{\boldsymbol{z}}$ is formed by stacking the cost vector n times, covering the prediction horizon of the controller.

$$\widetilde{\boldsymbol{Q}} = \begin{bmatrix} \boldsymbol{Q} & \mathbf{0} & \cdots & \mathbf{0} \\ \mathbf{0} & \boldsymbol{Q} & \ddots & \vdots \\ \vdots & \ddots & \ddots & \mathbf{0} \\ \mathbf{0} & \cdots & \mathbf{0} & \boldsymbol{Q} \end{bmatrix}, \quad \widetilde{\boldsymbol{P}} = \begin{bmatrix} \boldsymbol{P} & \mathbf{0} & \cdots & \mathbf{0} \\ \mathbf{0} & \boldsymbol{P} & \ddots & \vdots \\ \vdots & \ddots & \ddots & \mathbf{0} \\ \mathbf{0} & \cdots & \mathbf{0} & \boldsymbol{P} \end{bmatrix}, \quad \widetilde{\boldsymbol{z}} = \begin{bmatrix} \boldsymbol{z} & \dots & \boldsymbol{z} \end{bmatrix} \tag{4.14}$$

4.2.3 Constraints

The controller's constraints concern both the satellite states and the controller inputs and are included to make the solution of the optimization problem a feasible satellite trajectory.

Actuation Inequality Constraints

The upper and lower bounds on the actuators are given as $\boldsymbol{u}_{ub}$ and $\boldsymbol{u}_{lb}$ respectively. The bounds are defined in Equation (4.15).

$$\boldsymbol{u}_{ub} = \begin{bmatrix} \boldsymbol{M}_{MTQ_{MAX}} \\ \boldsymbol{\alpha}^{w}_{RW_{MAX}} \\ \boldsymbol{F}_{PROP_{MAX}} \end{bmatrix}, \quad \boldsymbol{u}_{lb} = \begin{bmatrix} -\boldsymbol{M}_{MTQ_{MAX}} \\ -\boldsymbol{\alpha}^{w}_{RW_{MAX}} \\ \boldsymbol{0}^{p} \end{bmatrix} \tag{4.15}$$

In the reformulated system, where $\boldsymbol{v}$ represents the actuation inputs covering the entire prediction horizon, the upper and lower bounds are stacked on top of each other n times to form the complete bounds, with n representing the length of the prediction horizon. The resulting bounds are given in Equation (4.16).

$$\boldsymbol{v}_{ub} = \begin{bmatrix} \boldsymbol{u}_{ub} \\ \vdots \\ \boldsymbol{u}_{ub} \end{bmatrix}, \quad \boldsymbol{v}_{lb} = \begin{bmatrix} \boldsymbol{u}_{lb} \\ \vdots \\ \boldsymbol{u}_{lb} \end{bmatrix} \tag{4.16}$$

Satellite State Inequality Constraints

The inequality constraints on the satellite state only concern the reaction wheels angular velocity and density of propellant. The upper and lower bounds are defined in Equation (4.17).

$$\boldsymbol{x}_{ub} = \begin{bmatrix} \infty \\ \infty \\ \boldsymbol{\omega}^{w}_{RW_{MAX}} \\ \infty \end{bmatrix}, \quad \boldsymbol{x}_{lb} = \begin{bmatrix} -\infty \\ -\infty \\ -\boldsymbol{\omega}^{w}_{RW_{MAX}} \\ \boldsymbol{0}^{p} \end{bmatrix} \tag{4.17}$$

The bounds are formulated as an inequality constraint on the form $\boldsymbol{Ax} \leq \boldsymbol{b}$ using the following choice of matrices given in Equation (4.18).

$$\boldsymbol{A} = \begin{bmatrix} 0 & 0 & 0 & 0 \\ 0 & 0 & 0 & 0 \\ 0 & 0 & 1 & 0 \\ 0 & 0 & 0 & 0 \\ 0 & 0 & 0 & 0 \\ 0 & 0 & 0 & 0 \\ 0 & 0 & -1 & 0 \\ 0 & 0 & 0 & -1 \end{bmatrix}, \quad \boldsymbol{b} = \begin{bmatrix} \boldsymbol{x}_{ub} \\ -\boldsymbol{x}_{lb} \end{bmatrix} \tag{4.18}$$

For the reformulated system, in which $\boldsymbol{\chi}$ contains the satellite states of the entire prediction horizon, the inequality matrices are repeated n times, with n representing the length of the prediction horizon. The resulting matrices are given in Equation (4.19).

$$\boldsymbol{A}_\chi \boldsymbol{\chi} \leq \boldsymbol{b}_\chi, \quad \boldsymbol{A}_\chi = \begin{bmatrix} \boldsymbol{A} & \boldsymbol{0} & \cdots & \boldsymbol{0} \\ \boldsymbol{0} & \boldsymbol{A} & \ddots & \vdots \\ \vdots & \ddots & \ddots & \boldsymbol{0} \\ \boldsymbol{0} & \cdots & \boldsymbol{0} & \boldsymbol{A} \end{bmatrix}, \quad \boldsymbol{b}_\chi = \begin{bmatrix} \boldsymbol{b} \\ \vdots \\ \boldsymbol{b} \end{bmatrix} \tag{4.19}$$

In the MPC controller, the only free variable is the control inputs $\boldsymbol{v}$, and thus the constraint is reformulated to be dependent on this. The resulting inequality constraint is presented in Equation (4.21).

$$\boldsymbol{A}_{\chi}\left(\boldsymbol{\chi}_0 + \Theta\boldsymbol{\upsilon}\right) \leq \boldsymbol{b}_{\chi} \tag{4.20}$$

$$\boldsymbol{A}_{\chi}\Theta\boldsymbol{\upsilon} \leq \boldsymbol{b}_{\chi} - \boldsymbol{A}_{\chi}\boldsymbol{\chi}_0 \tag{4.21}$$

4.2.4 Controller Adaptation

The controller optimizes the satellite trajectory using the Γ and Θ matrices. These matrices describe the dynamical response of the satellite and are linearized around the current satellite attitude and discretized to match the controller frequency. They are updated on each call to the MPC controller and are thus dependent on time.

The linearized state matrix of the satellite dynamics take the form given in Equation (4.22), in which $\boldsymbol{T}\left(\boldsymbol{q}\right)$ is defined as in Fossen [7]. The linearized input matrix takes the form given in Equation (4.24).

$$\boldsymbol{A}_{lin} = \begin{bmatrix} \mathbf{0}_{4\times4} & \boldsymbol{T}\left(\boldsymbol{q}^{ECI}\right) & \mathbf{0}_{4\times10} \\ \mathbf{0}_{13\times4} & \mathbf{0}_{13\times3} & \mathbf{0}_{13\times10} \end{bmatrix} \tag{4.22}$$

$$\boldsymbol{T}(\boldsymbol{q}) = \frac{1}{2}\begin{bmatrix} -\boldsymbol{\epsilon}(1) & -\boldsymbol{\epsilon}(2) & -\boldsymbol{\epsilon}(3) \\ \eta & -\boldsymbol{\epsilon}(3) & \boldsymbol{\epsilon}(2) \\ \boldsymbol{\epsilon}(3) & \eta & -\boldsymbol{\epsilon}(1) \\ -\boldsymbol{\epsilon}(2) & \boldsymbol{\epsilon}(1) & \eta \end{bmatrix} \tag{4.23}$$

$$\boldsymbol{B}_{lin} = \begin{bmatrix} \boldsymbol{B}_{MTQ} & \boldsymbol{B}_{RW} & \boldsymbol{B}_{PROP} \end{bmatrix} \tag{4.24}$$

The linearized input matrix in Equation (4.24) is made up of the linearized matrices for each actuator, which are defined in Equations (4.25), (4.26), and (4.27).

$$\boldsymbol{B}_{MTQ} = \boldsymbol{I}_{sys}^{-1}\begin{bmatrix} 0 & \boldsymbol{b}_{Earth}(3) & -\boldsymbol{b}_{Earth}(2) \\ -\boldsymbol{b}_{Earth}(3) & 0 & \boldsymbol{b}_{Earth}(1) \\ \boldsymbol{b}_{Earth}(2) & -\boldsymbol{b}_{Earth}(1) & 0 \end{bmatrix} \tag{4.25}$$

$$\boldsymbol{B}_{RW} = -\boldsymbol{I}_{sys}^{-1}\boldsymbol{A}_{RW}^{b}\boldsymbol{I}_{RW}^{w} \tag{4.26}$$

$$\boldsymbol{B}_{PROP} = \boldsymbol{I}_{sys}^{-1}\begin{bmatrix} \left(\boldsymbol{l}_1^s - \boldsymbol{c}_{mass}^s\right)\times\boldsymbol{d}_1 & \dots & \left(\boldsymbol{l}_6^s - \boldsymbol{c}_{mass}^s\right)\times\boldsymbol{d}_6 \end{bmatrix} \tag{4.27}$$

The discretization is done as a first-order Taylor approximation, presented in Equation (4.29). The discretized matrices are then used to form the Γ and Θ matrices as presented in Equation (4.10), and the adaptation is complete.

$$\boldsymbol{A}_d = \mathbb{I} + \boldsymbol{A}_{lin} \cdot t_{step} \tag{4.28}$$

$$\boldsymbol{B}_d = \boldsymbol{B}_{lin} \cdot t_{step} \tag{4.29}$$

4.2.5 Optimization Algorithm

The resulting optimization problem consists of a quadratic cost function with an absolute value term, linear constraints, and an integer subset of optimization variables. A quadratic integer problem (QIP) is considered as being NP-hard [4], and no straightforward method of finding the optimum exists. A pseudo-optimal method that showed promising results in terms of computational speed and accuracy during simulations was the MATLAB genetic algorithm *ga()* [14].

The genetic algorithm consists of many parameters that need to be defined. Here, each generation's population size is set to 100, and a uniform probability distribution creates the initial population. 80% of the population at the next generation is created through crossover, and 5% of the points are considered as elite, which guarantees survival to the next generation. The optimization stops if the average relative cost function improvement is less than $1 \cdot 10^{-6}$ over 50 consecutive generations.

Chapter 5

Simulations

This chapter presents the simulation setup for the conducted experiments. The first section, 5.1 *Satellite Parameters*, presents the satellite construction details used for the simulations. Section 5.1.1 *Actuators* presents the parameters used for the actuators, and section 5.2 *Controller Parameters* presents the controller configuration. Lastly, the propagation algorithm is discussed in section 5.3 *Propagation*.

The simulations were carried out using MATLAB version $R2020a$. A flow chart of the simulation algorithm for the PD controller is presented in Figure 5.1, and for the MPC in Figure 5.2.

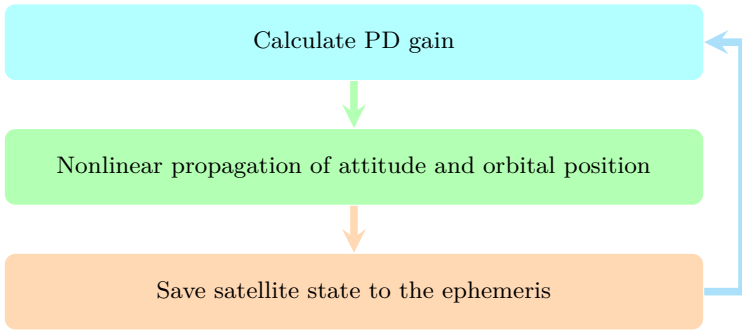

Figure 5.1: Diagram illustrating the Algorithm used for Simulations with PD Control.

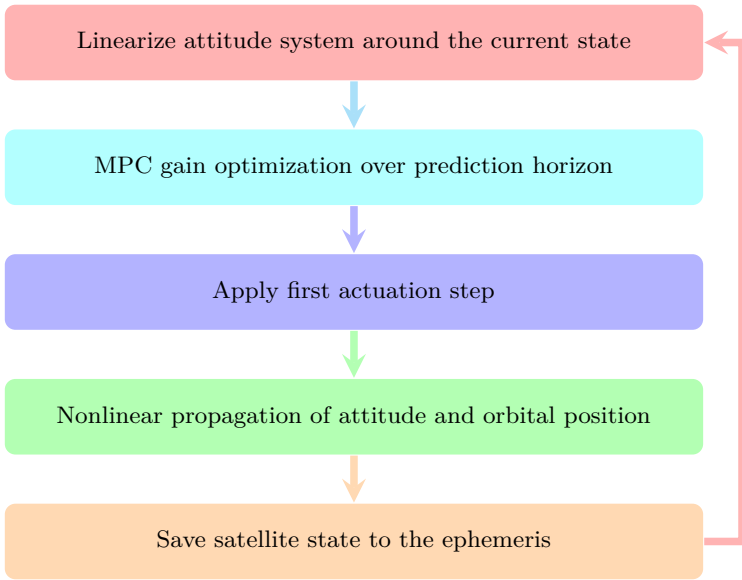

Figure 5.2: Diagram illustrating the Algorithm used for Simulations with MPC.

5.1 Satellite Parameters

The satellite is modeled as a 6U CubeSat based on the HYPSO satellite of NTNU SmallSat Lab. The data used for the simulations are presented in table 5.1, with C_D being the coefficient of drag and C_R being the coefficient of reflectivity. The shape of the satellite is assumed to be a cuboid.

Satellite Construction Parameters	
X dimension	0.2263 m
Y dimension	0.100 m
Z dimension	0.366 m
Mass	5.7 kg
Drag Coefficient, C_D	2.2
Reflectivity Coefficient, C_R	1.0

Table 5.1: Construction Parameters for the Simulated Satellite.

5.1.1 Actuators

The satellite is assumed to be equipped with three attitude actuators, namely the **reaction wheels**, **magnetorquers**, and a **propulsion system**. The configurations of these actuators are discussed in this section.

Reaction Wheels

The torque distribution matrix used for the reaction wheels is provided in Equation (5.1). The maximum reaction wheel acceleration is defined as $\alpha_{MAX_{RW}} = 108.9\ \frac{rad}{s^2}$, and maximum velocity $\omega_{MAX_{RW}} = 680.7\ \frac{rad}{s}$. The reaction wheels are assumed to have equal moment of inertia in the direction of their respective torque vectors, defined as $I^w_{RW} = 2.94 \cdot 10^{-5}\ kg\ m^2$.

$$\boldsymbol{A}^b_w = \begin{bmatrix} \sqrt{\frac{2}{3}} & -\sqrt{\frac{2}{3}} & 0 & 0 \\ \sqrt{\frac{1}{3}} & \sqrt{\frac{1}{3}} & -\sqrt{\frac{1}{3}} & -\sqrt{\frac{1}{3}} \\ 0 & 0 & \sqrt{\frac{2}{3}} & -\sqrt{\frac{2}{3}} \end{bmatrix} \tag{5.1}$$

Magnetorquer

The magnetorquer actuator consists of six magnetorquer coils in a perpendicular configuration. The magnetorquer actuator is modeled as being able to produce a magnetic dipole along all three axes of the satellite, with a spherical maximum and minimum dipole strength given in Equations (5.2) and (5.3).

$$\boldsymbol{M}_{MAX} = \mathbb{I}_{3\times3} \cdot 2M_{coil_{MAX}} = \mathbb{I}_{3\times3} \cdot 0.84\ \text{Am}^2 \tag{5.2}$$

$$\boldsymbol{M}_{MIN} = -\mathbb{I}_{3\times3} \cdot 0.84\ \text{Am}^2 \tag{5.3}$$

Propulsion System

When the thruster is firing, the force output is considered an integer value, either taking the value 0 or a value from a predefined set $\mathbb{F}$. The propulsion system

affects both the orbital and attitude dynamics of the satellite, and the orbital effects of the thrusters on the satellite are modeled as an external force acting on the satellite given by Equation (5.4).

$$\boldsymbol{F}_T^{ECI} = -\mathbb{R}_s^{ECI} \sum_k f_k \cdot \boldsymbol{d}_k^s \tag{5.4}$$

The torque produced by the propulsion system is given in Equation (5.5).

$$\boldsymbol{\tau}_T^b = -\sum_k \left[\boldsymbol{l}_k^b \times \left(f_k \cdot \boldsymbol{d}_k^s \right) \right] \tag{5.5}$$

To calculate the torque, an expression for the thrust arm $\boldsymbol{l}_k^b$ of the propulsion module in the body frame is needed. The expression given in Equation (5.6) converts the thruster position from the structural frame to the body frame by subtracting the center of mass of the satellite in the structural frame. The position of the k-th thruster in the structural frame is given by $\boldsymbol{l}_k^s$. The center of the k-th propulsion unit in the body frame, $\boldsymbol{l}_k^b$, is propagated as in Equation (5.7).

$$\boldsymbol{l}_k^b(t) = \boldsymbol{l}_k^s - \boldsymbol{c}_m^s(t) \tag{5.6}$$

$$\frac{{}^b d}{dt}\boldsymbol{l}_k^b = -\frac{{}^s d}{dt}\boldsymbol{c}_m^s(t) \tag{5.7}$$

In the rest of the section, the propulsion system parameters for two specific thruster configurations are presented. The configurations considered are two systems based on the *NanoFEEP* and *Aurora Thruster* propulsion systems.

NanoFEEP. The first thruster configuration is based on the *nano Field Emission Electronic Propulsion* system [**NanoFEEP**] developed by researchers at the Technical University of Dresden. The system is a form of ion-thruster with liquid metal propellant, in which thrust is generated by evaporated ions from the propellant accelerating under the influence of a strong magnetic field. For this setup, the thruster and propellant are modeled as being integrated into one unit, with a total of six such units assembled on the satellite. The thruster and propellant assembly is illustrated in Figure 5.3. The use of ion-thrusters requires an electron-emitting neutralizer, but this component is not modeled for the simulations. The parameters used for the thruster actuators are given in Table 5.2, and the parameters used for the propellant are given in Table 5.3.

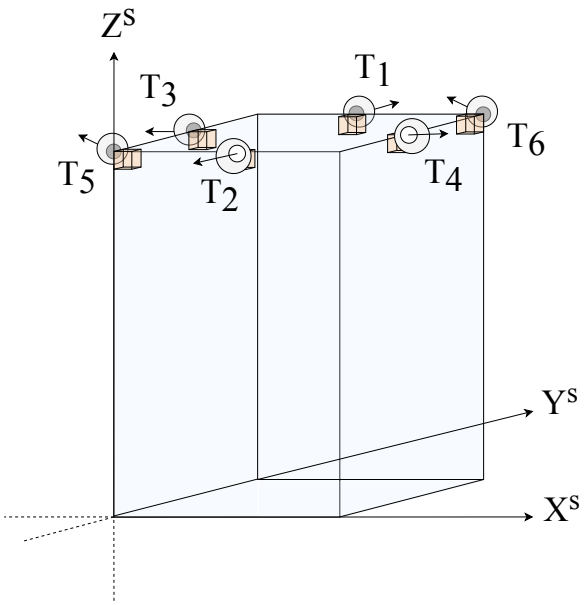

Figure 5.3: Figure shows thruster and propellant placement for the NanoFEEP propulsion system on the satellite in the structure frame. The propellant is illustrated as orange cuboids contained within the satellite body, and the thrust vectors are placed along the border of the satellite body. The components of T_1 and T_2 point along the Y^s axis, T_3 and T_4 point along the X^s axis, while T_5 and T_6 vectors point in equal distances along the X^s and Y^s axes.

NanoFEEP Thrust Parameters		
	Thrust position	Thrust direction
T_1	$\begin{bmatrix} \frac{d_x}{2} & d_y & d_z \end{bmatrix}$	$\begin{bmatrix} 0 & 1 & 0 \end{bmatrix}$
T_2	$\begin{bmatrix} \frac{d_x}{2} & 0 & d_z \end{bmatrix}$	$\begin{bmatrix} 0 & -1 & 0 \end{bmatrix}$
T_3	$\begin{bmatrix} 0 & \frac{d_y}{2} & d_z \end{bmatrix}$	$\begin{bmatrix} -1 & 0 & 0 \end{bmatrix}$
T_4	$\begin{bmatrix} d_x & \frac{d_y}{2} & d_z \end{bmatrix}$	$\begin{bmatrix} 1 & 0 & 0 \end{bmatrix}$
T_5	$\begin{bmatrix} 0 & 0 & d_z \end{bmatrix}$	$\begin{bmatrix} -\frac{1}{\sqrt{2}} & \frac{1}{\sqrt{2}} & 0 \end{bmatrix}$
T_6	$\begin{bmatrix} d_x & d_y & d_z \end{bmatrix}$	$\begin{bmatrix} -\frac{1}{\sqrt{2}} & \frac{1}{\sqrt{2}} & 0 \end{bmatrix}$
	$\mathbb{F}$ [μN]	ISP [s]
T_1		
$\vdots$	$\begin{bmatrix} 0 & 1 & 2 & \dots & 20 \end{bmatrix}$	3000
T_6		

Table 5.2: Parametric Values for the Simulated NanoFEEP Thrusters.

NanoFEEP Propellant Parameters			
	X^s-dimensions [m]	Y^s-dimensions [m]	Z^s-dimensions [m]
T_1	$\begin{bmatrix} \frac{d_x}{2} - 5 \cdot 10^{-3} \\ \frac{d_x}{2} + 5 \cdot 10^{-3} \end{bmatrix}$	$\begin{bmatrix} d_y - 1 \cdot 10^{-2} \\ d_y \end{bmatrix}$	$\begin{bmatrix} d_z - 1 \cdot 10^{-2} \\ d_z \end{bmatrix}$
T_2	$\begin{bmatrix} \frac{d_x}{2} - 5 \cdot 10^{-3} \\ \frac{d_x}{2} + 5 \cdot 10^{-3} \end{bmatrix}$	$\begin{bmatrix} 0 \\ 1 \cdot 10^{-2} \end{bmatrix}$	$\begin{bmatrix} d_z - 1 \cdot 10^{-2} \\ d_z \end{bmatrix}$
T_3	$\begin{bmatrix} 0 \\ 1 \cdot 10^{-2} \end{bmatrix}$	$\begin{bmatrix} \frac{d_x}{2} - 5 \cdot 10^{-3} \\ \frac{d_x}{2} + 5 \cdot 10^{-3} \end{bmatrix}$	$\begin{bmatrix} d_z - 1 \cdot 10^{-2} \\ d_z \end{bmatrix}$
T_4	$\begin{bmatrix} d_x - 1 \cdot 10^{-2} \\ d_x \end{bmatrix}$	$\begin{bmatrix} \frac{d_x}{2} - 5 \cdot 10^{-3} \\ \frac{d_x}{2} + 5 \cdot 10^{-3} \end{bmatrix}$	$\begin{bmatrix} d_z - 1 \cdot 10^{-2} \\ d_z \end{bmatrix}$
T_5	$\begin{bmatrix} 0 \\ 1 \cdot 10^{-2} \end{bmatrix}$	$\begin{bmatrix} 0 \\ 1 \cdot 10^{-2} \end{bmatrix}$	$\begin{bmatrix} d_z - 1 \cdot 10^{-2} \\ d_z \end{bmatrix}$
T_6	$\begin{bmatrix} d_x - 1 \cdot 10^{-2} \\ d_x \end{bmatrix}$	$\begin{bmatrix} d_y - 1 \cdot 10^{-2} \\ d_y \end{bmatrix}$	$\begin{bmatrix} d_z - 1 \cdot 10^{-2} \\ d_z \end{bmatrix}$
	V_{prop} [m^3]	m_{prop} [kg]	
T_1 $\vdots$ T_6	$1 \cdot 10^{-6}$	$1 \cdot 10^{-2}$	

Table 5.3: Parametric Values for the Simulated NanoFEEP Propellant.

Aurora Thruster. The second thruster configuration is based on the *Aurora Propulsion Technologies* water-based resistojet system [2]. The thrust force is generated by heating and expelling propellant mass, which in this case consists of water-vapor. For this setup, multiple thrusters are modeled to share a single propellant tank. The thruster and propellant assembly is illustrated in Figure 5.4. The parameters used for the thruster actuators are given in Table 5.4, and the parameters used for the propellant are given in Table 5.5.

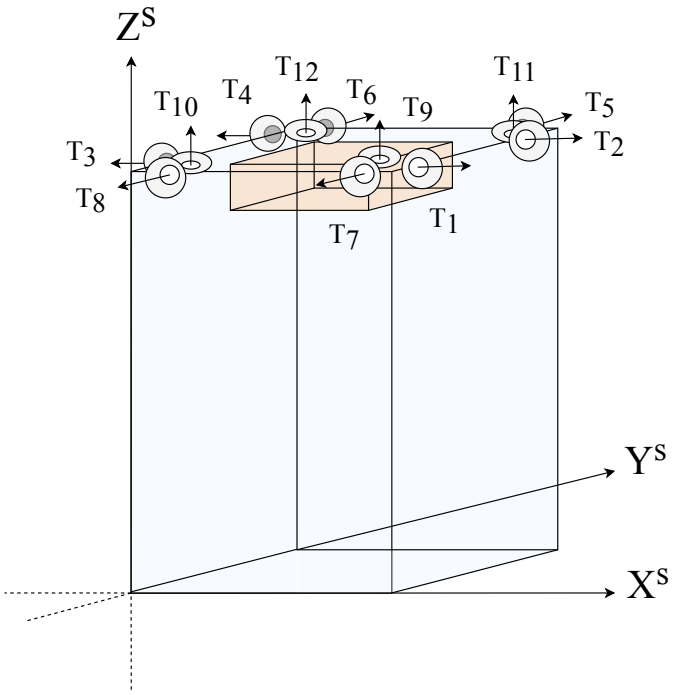

Figure 5.4: Figure shows thruster and propellant placement for the Aurora resistojet propulsion system on the satellite in the structure frame. The propellant is shared between the thrusters and illustrated as an orange cuboid contained within the satellite body. The thrust direction vectors are illustrated as arrows and placed along the border of the satellite body. The components of T_1 and T_2 point along the positive X^s axis, T_3 and T_4 point along the negative X^s axis. T_5 and T_6 point along the positive Y^s axis, T_7 and T_8 point along the negative Y^s axis. T_9 through T_{12} point along the positive Z^s axis.

Aurora Thrust Parameters		
	Thrust position [m]	Thrust direction
T_1	$\begin{bmatrix} d_x & 0.01 & d_z - 0.01 \end{bmatrix}$	$\begin{bmatrix} 1 & 0 & 0 \end{bmatrix}$
T_2	$\begin{bmatrix} d_x & d_y - 0.01 & d_z - 0.01 \end{bmatrix}$	$\begin{bmatrix} 1 & 0 & 0 \end{bmatrix}$
T_3	$\begin{bmatrix} 0 & 0.01 & d_z - 0.01 \end{bmatrix}$	$\begin{bmatrix} -1 & 0 & 0 \end{bmatrix}$
T_4	$\begin{bmatrix} 0 & d_y - 0.01 & d_z - 0.01 \end{bmatrix}$	$\begin{bmatrix} -1 & 0 & 0 \end{bmatrix}$
T_5	$\begin{bmatrix} d_x - 0.01 & d_y & d_z - 0.01 \end{bmatrix}$	$\begin{bmatrix} 0 & 1 & 0 \end{bmatrix}$
T_6	$\begin{bmatrix} 0.01 & d_y & d_z - 0.01 \end{bmatrix}$	$\begin{bmatrix} 0 & 1 & 0 \end{bmatrix}$
T_7	$\begin{bmatrix} d_x - 0.01 & 0 & d_z - 0.01 \end{bmatrix}$	$\begin{bmatrix} 0 & -1 & 0 \end{bmatrix}$
T_8	$\begin{bmatrix} 0.01 & 0 & d_z - 0.01 \end{bmatrix}$	$\begin{bmatrix} 0 & -1 & 0 \end{bmatrix}$
T_9	$\begin{bmatrix} d_x - 0.01 & 0.01 & d_z \end{bmatrix}$	$\begin{bmatrix} 0 & 0 & 1 \end{bmatrix}$
T_{10}	$\begin{bmatrix} 0.01 & 0.01 & d_z \end{bmatrix}$	$\begin{bmatrix} 0 & 0 & 1 \end{bmatrix}$
T_{11}	$\begin{bmatrix} d_x - 0.01 & d_y - 0.01 & d_z \end{bmatrix}$	$\begin{bmatrix} 0 & 0 & 1 \end{bmatrix}$
T_{12}	$\begin{bmatrix} 0.01 & d_y - 0.01 & d_z \end{bmatrix}$	$\begin{bmatrix} 0 & 0 & 1 \end{bmatrix}$
Shared parameters $T_1 \ \ldots \ T_{12}$		
$\mathbb{F}$ [mN]	$\begin{bmatrix} 0 & 0.1 & 0.25 & 0.5 & 0.75 & 1 & 1.25 & 1.5 & 1.75 & 2 \end{bmatrix}$	
ISP [s]	100	

Table 5.4: Parametric Values for the Simulated Aurora Thrusters.

Aurora Propellant Parameters		
X^s-dimensions [m]	Y^s-dimensions [m]	Z^s-dimensions [m]
$\begin{bmatrix} \frac{d_x}{2} - 4 \cdot 10^{-2} \\ \frac{d_x}{2} + 4 \cdot 10^{-2} \end{bmatrix}$	$\begin{bmatrix} \frac{d_x}{2} - 2 \cdot 10^{-2} \\ \frac{d_x}{2} + 2 \cdot 10^{-2} \end{bmatrix}$	$\begin{bmatrix} d_z - 6.125 \cdot 10^{-2} \\ d_z - 3 \cdot 10^{-2} \end{bmatrix}$
V_{prop} [m^3]	m_{prop} [kg]	
0.1	0.1	

Table 5.5: Parametric Values for the Simulated Aurora Propellant.

5.2 Controller Parameters

This section presents the parametric configuration of the attitude controllers. Detailed explanations of the controllers are given in chapter 4 *Controller Design*. The parameters applied to the PD controller are presented in subsection 5.2.1, and the parameters for the MPC are presented in subsection 5.2.2.

5.2.1 PD Parameters

The PD controller parameters were determined experimentally, based on what produced a desirable satellite response in the simulations. The parameters differ based on the objective, and separate sets of parameters are used for attitude and slew rate control. The chosen parameters are presented in Equations (5.8) and (5.9).

$$\textit{Attitude:} \qquad K_{p_{RW}} = 10, \qquad K_{d_{RW}} = 10, \qquad K_{dd_{RW}} = 0 \tag{5.8}$$

$$\textit{Slew rate:} \qquad K_{p_{RW}} = 0, \qquad K_{d_{RW}} = 10, \qquad K_{dd_{RW}} = 0.1 \tag{5.9}$$

5.2.2 MPC Parameters

For the adaptive model predictive controller, the parameters that need to be defined are the cost function values given in Equations (5.10) and (5.11). These include the cost on the attitude deviation, $\boldsymbol{\zeta}_a$, angular velocity deviation, $\boldsymbol{\zeta}_\omega$, and reaction wheel momentum, $\boldsymbol{\zeta}_m$. Additionally, there are actuation costs for the magnetorquer, $\boldsymbol{\zeta}_{MTQ}$, thruster, $\boldsymbol{\zeta}_T$, and the reaction wheels, $\boldsymbol{\zeta}_{RW}$. The actuation costs are based on the power consumption of the different actuators, scaled by a factor κ to achieve the desired behavior. In contrast, the satellite state costs are defined solely such that a desirable output behavior is achieved.

$$\boldsymbol{Q} = \begin{bmatrix} 0 & & & & & & & & & & \\ & \boldsymbol{\zeta}_a & & & & & & & & & \\ & & \boldsymbol{\zeta}_\omega & & & & & & & & \\ & & & 0 & & & & & & & \\ & & & & \ddots & & & & & & \\ & & & & & 0 & & & & & \\ & & & & & & \boldsymbol{\zeta}_m & & & & \\ & & & & & & & 0 & & & \\ & & & & & & & & \ddots & & \\ & & & & & & & & & 0 & \end{bmatrix}, \quad \boldsymbol{P} = \begin{bmatrix} \boldsymbol{\zeta}_{MTQ} & & & & \\ & 0 & & & \\ & & \ddots & & \\ & & & 0 & \\ & & & & \boldsymbol{\zeta}_T \end{bmatrix} \tag{5.10}$$

$$\boldsymbol{z} = \begin{bmatrix} 0 & \dots & 0 & \boldsymbol{\zeta}_{RW} & 0 & \dots & 0 \end{bmatrix} \tag{5.11}$$

Magnetorquer Weights

The cost of the magnetorquer actuation, $\boldsymbol{\zeta}_{MTQ}$, is given in Equation (5.12). The coefficient is based on the voltage and torque ratings provided in the NanoAvionics SatBus MTQ M6P magnetorquer datasheet. A factor κ_{MTQ} is added so that the actuator usage of the MPC can be tuned.

$$\boldsymbol{\zeta}_{MTQ} = \kappa_{MTQ} \cdot \mathbb{I}_{3\times 1} \cdot \frac{R_{coil}}{n^2 S^2} = \kappa_{MTQ} \cdot \mathbb{I}_{3\times 1} \cdot 4.875 \tag{5.12}$$

Reaction Wheels Weights

The cost of the reaction wheel actuation, $\boldsymbol{\zeta}_{RW}$, is given in Equation (5.13). The cost is calculated based on the ideal operating point of the reaction wheel, given by $\boldsymbol{\omega}_0^w$. The efficiency value is calculated based on the power and torque ratings provided in the Nano Avionics NA-4RW0-G0-R6 datasheet [18]. In addition, a factor κ_{RW} is added, which enables the actuator usage to be tuned, e.g., to reduce wear and tear on the reaction wheels.

$$\boldsymbol{\zeta}_{RW} = \kappa_{RW} \left(P_{RW_{idle}} + \frac{I_{RW}}{\eta_0} \right) |\boldsymbol{\omega}_0^w| = 0.045 \cdot \kappa_{RW} \cdot |\boldsymbol{\omega}_0^w| \tag{5.13}$$

NanoFEEP Thruster Weights

The cost of the NanoFEEP thruster actuation, $\boldsymbol{\zeta}_T$, is given in Equation (5.14). At thruster firing, the node is applied 150 μA and 5600 V, which makes the firing power consumption equal to $P_T = 0.84\ W$. The preheating demand is between 50 mW and 150 mW, but is not considered in the cost. An additional cost of the thruster is the loss of propellant, which is incorporated by multiplying the actuation weight by a factor κ_T.

$$\boldsymbol{\zeta}_T = \kappa_T \cdot \mathbb{I}_{6\times 1} \cdot P_T = \kappa_T \cdot \mathbb{I}_{6\times 1} \cdot 0.84 \tag{5.14}$$

Aurora Thruster Weights

The cost of the Aurora thruster actuation, $\boldsymbol{\zeta}_T$, is given in Equation (5.15). The power consumption at thruster firing is equal to $P_T = 5\ W$. The indirect cost of propellant consumption is incorporated by multiplying the actuation weight by a factor κ_T, which will need to be defined.

$$\boldsymbol{\zeta}_T = \kappa_T \cdot \mathbb{I}_{6\times 1} \cdot P_T = \kappa_T \cdot \mathbb{I}_{6\times 1} \cdot 5 \tag{5.15}$$

5.3 Propagation

The satellite ephemeris is calculated by applying actuator gains and propagating the satellite state using the MATLAB *ode45()* solver. The solver uses variable step lengths and compares the results of a fourth and fifth-order *Runge-Kutta* algorithm [20]. The dynamic equation is propagated based on initial conditions and an expression for the satellite state derivative, as presented in Equation (5.16). The propagation is performed in-between actuation gain calculations, and has a duration equal to the inverse of the controller frequency, $d_{propagation} = \frac{1}{f_{controller}}$.

$$\boldsymbol{x}_0 \text{ given}, \qquad \dot{\boldsymbol{x}} = \begin{bmatrix} \dot{\boldsymbol{r}}^i \\ \dot{\boldsymbol{v}}^i \\ \dot{\boldsymbol{q}}^i \\ \dot{\boldsymbol{\omega}}^b_{sat} \\ \dot{\boldsymbol{\omega}}^w_{RW} \\ \dot{\boldsymbol{I}}^b_{sat} \\ \dot{\boldsymbol{\rho}}_{prop} \\ \dot{\boldsymbol{c}}^s_m \end{bmatrix} \tag{5.16}$$

The state variable derivatives of Equation (5.16) are described in chapter 3 *Satellite Model*, section 3.5 *Satellite Dynamics*. $\boldsymbol{r}^i$ represents the position of the satellite in the ECI frame, and $\boldsymbol{v}^i$ its translational velocity. $\boldsymbol{q}^i$ is the attitude quaternion of the satellite, describing the rotation from the ECI frame to the satellite body frame. $\boldsymbol{\omega}^b_{sat}$ describes the angular velocity of the satellite given in the body frame, and $\boldsymbol{\omega}^w_{RW}$ describes the scalar angular velocities of the reaction wheels relative to the satellite body. $\boldsymbol{I}^b_{sat}$ is the inertia matrix of the satellite in the body frame, and $\boldsymbol{\rho}_{prop}$ is the density of the propellant. Lastly, $\boldsymbol{c}^s_m$ is the center of mass of the satellite.

The satellite state dynamics include perturbing forces and torques, which are calculated as described in chapter 2 *Background Theory*, section 2.2 *Orbital Perturbations*. Earth's magnetic field is calculated using the MATLAB function *igrfmagm()* from the Aerospace Toolbox, which is based on the International Geomagnetic Reference Field.

Chapter 6

Results

This chapter presents the results on satellite attitude maneuver performance obtained from simulations. The results are organized in sections based on the objective of the simulations and regarded as different experiments. Section 6.1 provides an overview of the experiments, and section 6.2, 6.3, 6.4, and 6.5 present the first, second, third and fourth experiment, respectively. Section 6.6 summarizes the results, presenting observations made across the experiments.

6.1 Overview of Experiments

A list of the experiments conducted and their objective is given in table 6.1. In addition to having different objectives, the experiments also differ in terms of duration and initial satellite conditions.

Experiments Overview	
	Objective
E 1	Optimal MPC Parameters
E 2	Pointing Maneuver Performance
E 3	Slew Rate Performance
E 4	Momentum Dumping Performance

Table 6.1: Objectives of the Conducted Experiments.

In total, four experiments were conducted. The first experiment was designed to identify suitable parameters for the model predictive controller. The second experiment compares the performance of the different actuator and controller combinations on pointing maneuvers, and the third experiment compares the performance on slew rate maneuvers. The fourth and final experiment concerns the ability of the actuator combinations to dump excess reaction wheel momentum.

6.2 Experiment 1

The first experiment is designed to identify suitable MPC parameters. The parameter identification was split into large and small momentum maneuvers, as different controller properties are desired in the two cases. Furthermore, the parameter identification was split based on the actuator combination.

The MPC parameters that need to be optimized are the satellite state weights, controller timestep, and length of the prediction horizon. Besides, factors assigned to the actuation weights need to be identified, limiting excess use of the actuators.

6.2.1 Cost Function Weights

The behavior of an MPC controlled system is mainly dependent on the cost function design. Careful thought needs to be taken when assigning the state deviation and actuation weights. The proposed weights were found based on trial and error in the simulations, and do not reflect the actual optimal values.

Table 6.2 presents the applied cost function parameters. As previously discussed, different parameters are used based on the actuator configuration and control objective.

6.2.2 Controller Timestep

The choice of controller timestep length is a compromise between computational load and controller performance. The controller timestep was chosen to be:

$$\text{Timestep} = 1\text{s}$$

This choice of timestep led to the best performance in large momentum maneuvers, and gives the controller sufficient possibility to correct small momentum maneuvers. It is also considered to be the minimum timestep achievable given the limited computational power onboard a satellite.

Cost Function Parameters						
Actuators & Control Objective	ζ_a	ζ_ω	ζ_m	κ_{MTQ}	κ_T	κ_{RW}
With Aurora:						
Large Momentum	10^{15}	0	10^6	1	10^{14}	10^6
Small Momentum	0	10^{15}	$5 \cdot 10^5$	10^3	10^{12}	10^8
With NanoFEEP:						
Large Momentum	10^{15}	0	10^6	1	10^9	10^6
Small Momentum	0	10^{15}	10^4	1	10^9	10^6
No Thruster:						
Large Momentum	10^{15}	0	10^6	1	0	10^6
Small Momentum	0	10^{15}	10^4	1	0	10^6

Table 6.2: Experimentally derived parameters for the MPC cost function.

Figure 6.1 shows the attitude quaternion error for different timestep lengths when the satellite is tracking a reference attitude trajectory. The weights in the simulations were kept as described in subsection 6.2.1, and the prediction horizons were chosen through trial and error based on performance. The prediction horizons were chosen as follows: For the timestep of 0.5s, the prediction horizon was six; The timesteps of 1s, 1.5s, and 2s, all had a prediction horizon of three.

6.2.3 Prediction Horizon

The prediction horizon parameter was found experimentally based on simulations. As was the case for the cost function parameters, the prediction horizon parameter was identified for different actuator configurations and control objectives.

The results are organized based on actuator configuration, which includes both large and small momentum maneuvers. The actuator configurations discussed are (1) *Reaction Wheels and Magnetorquer*, (2) *Aurora Thrusters, Magnetorquer, and Reaction Wheels*, (3) *Aurora Thrusters and Magnetorquer*, and (4) *NanoFEEP Thrusters and Magnetorquer*.

Reaction Wheels and Magnetorquer

Figures 6.2 and 6.3 present the results from the **large momentum maneuver**. It is observed that a prediction horizon of $\mathbf{PH = 3}$ gives a desirable attitude response and the least deviation from the reference trajectory. Both larger and smaller prediction horizons result in larger overshoot and longer transient periods.

The **small momentum maneuver** is given in Figure 6.4. It is observed that when the emphasis is put on the precision in small corrections, the shortest prediction horizon of $\mathbf{PH = 1}$ performs the best. Increasing the prediction horizon results in more oscillatory behavior.

Aurora Thrusters, Magnetorquer, and Reaction Wheels

Figures 6.5 and 6.6 presents the satellite attitude response when the controller tracks a large momentum reference trajectory, and figure 6.7 presents the satellite rotational velocity when the controller tracks a small momentum slew rate trajectory.

The optimal prediction horizon for **large momentum maneuvers** is found by comparing the performance of different prediction horizon lengths in Figures 6.5 and 6.6. It is observed that a prediction horizon of $\mathbf{PH = 3}$ leads to the smallest attitude quaternion deviation, and minimal overshoot on the reference signal.

For the **small momentum maneuvers**, it is once again shown that the smallest prediction horizon of $\mathbf{PH = 1}$ performs the best, with broader prediction horizons resulting in more oscillatory and noisy behavior.

Aurora Thrusters and Magnetorquer

Plots comparing different prediction horizon lengths for the case in which the satellite is actuated by the Aurora thrusters and a magnetorquer are presented in Figures 6.5, 6.6, and 6.10.

Figures 6.5 and 6.6 presents the satellite attitude response when the controller tracks a reference attitude trajectory, and is used to find the optimal prediction horizon for **large momentum maneuvers**. From the plots, it is seen that a prediction horizon of $\mathbf{PH = 15}$ performs well in terms of reference tracking and

overshoot compared to the other data points.

The optimal parameter for a **small momentum maneuver** is found by studying Figure 6.10, in which the satellite is tracking a reference slew rate trajectory. The shortest prediction horizon of $\mathbf{PH = 1}$ is found to provide the best results.

NanoFEEP Thrusters and Magnetorquer

As the satellite dynamics actuated by the NanoFEEP thrusters and magnetorquer are much slower compared to the dynamics actuated by the Aurora thrusters or reaction wheels, a different timescale is used to find the optimal parameters for this set of actuators.

Figures 6.11 and 6.12 provide information on the performance in **large momentum maneuvers**, with the satellite tracking an attitude reference trajectory. A prediction horizon of $\mathbf{PH = 150}$ is chosen, based on the observation that it both handles the step response and steady state tracking well.

The optimal value for **small momentum maneuvers** is found by studying Figure 6.13, in which the satellite is tracking a reference slew rate trajectory. Although the differences are smaller than in previous actuator configurations, the shortest prediction horizon of $\mathbf{PH = 1}$ is still found to provide the best performance.

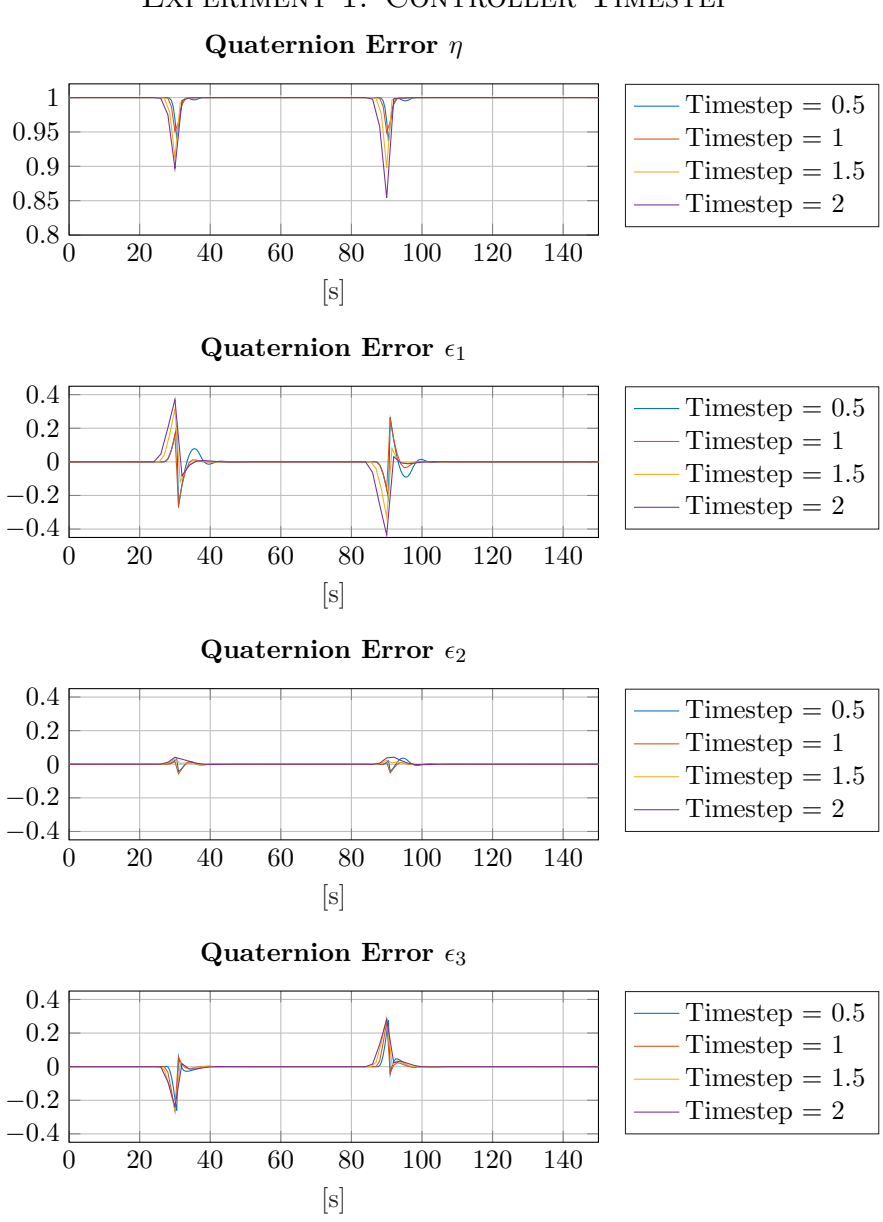

Figure 6.1: Attitude quaternion error for different timestep lengths when following a reference trajectory. Simulated with the Aurora Thrusters, Magnetorquer and Reaction Wheels actutors.

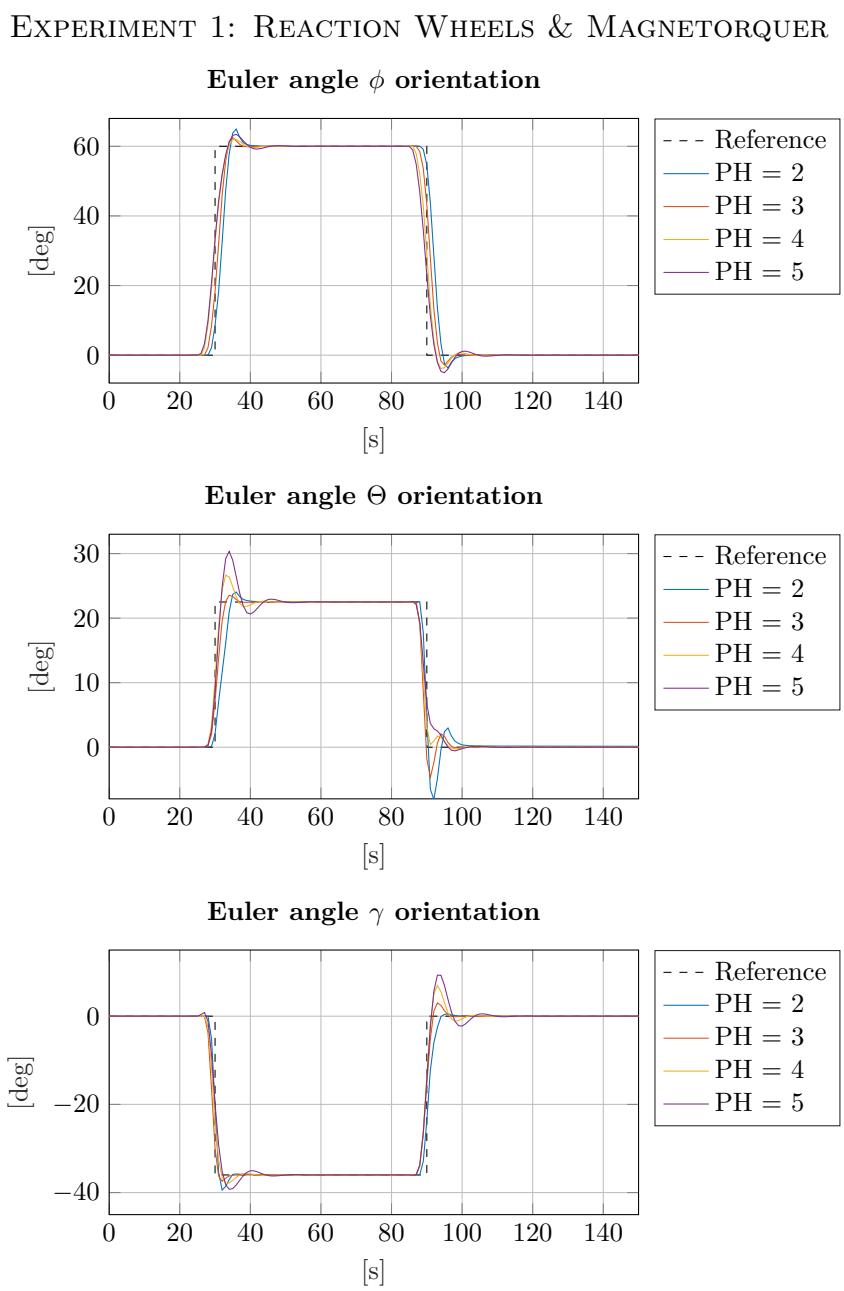

Figure 6.2: Satellite attitude responses based on different prediction horizon lengths, in large momentum maneuvers with Reaction Wheels and Magnetorquer actutors. Measured in Euler ϕ, Θ and γ angles (*zyx* convention).

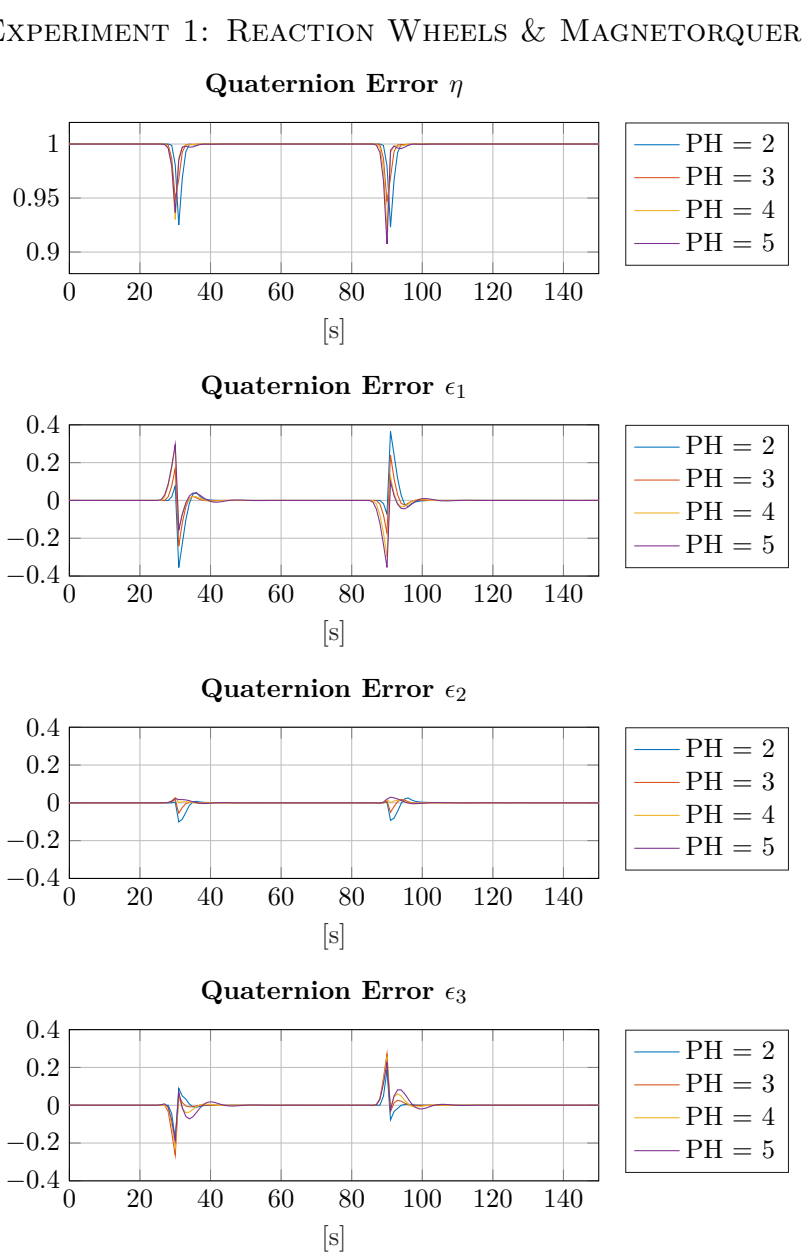

Figure 6.3: Attitude quaternion error based on different prediction horizon lengths, in large momentum maneuvers with Reaction Wheels and Magnetorquer actutors.

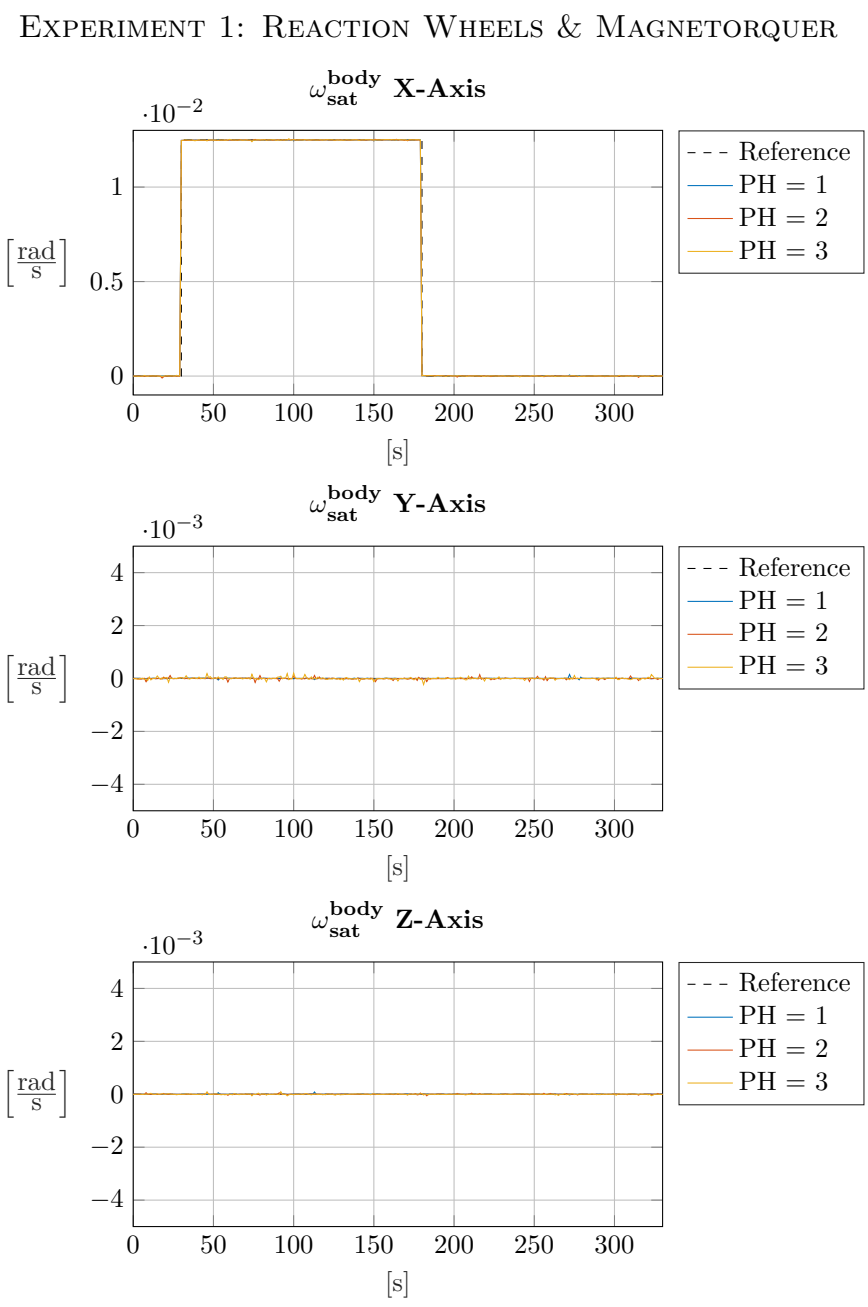

Figure 6.4: Satellite angular velocity response for different prediction horizon lengths. Represents small momentum maneuver with Reaction Wheels and Magnetorquer actutors.

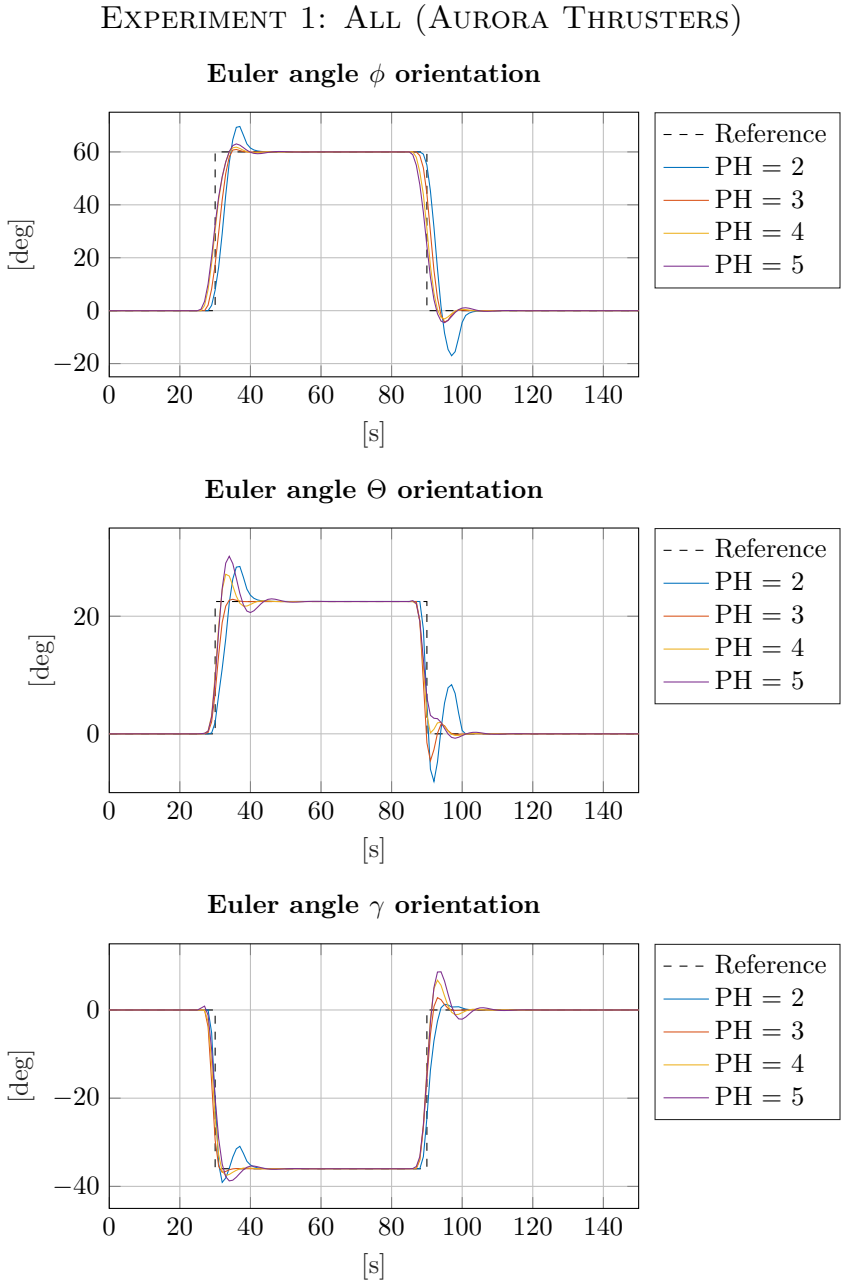

Figure 6.5: Satellite attitude responses based on different prediction horizon lengths, in large momentum maneuvers with Aurora Thrusters, Magnetorquer and Reaction Wheels actutors. Measured in Euler ϕ, Θ and γ angles (*zyx* convention).

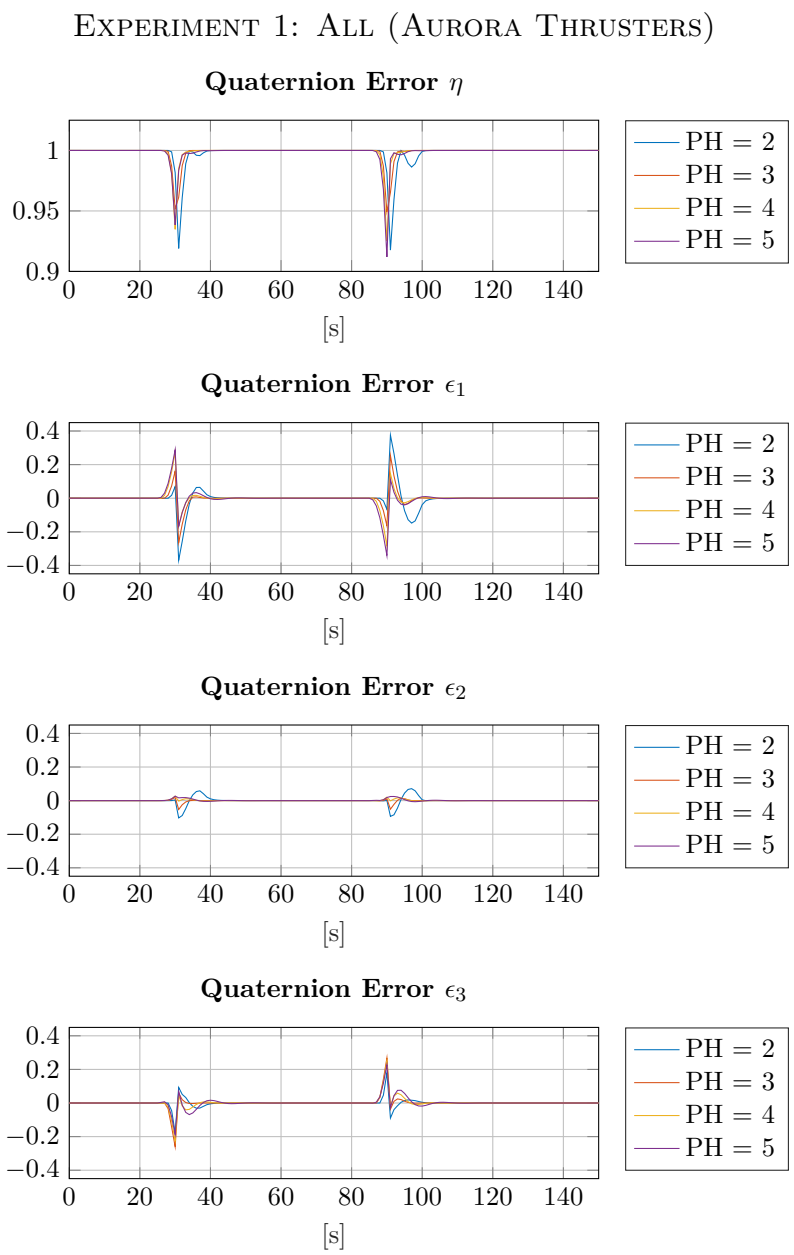

Figure 6.6: Attitude quaternion error based on different prediction horizon lengths, in large momentum maneuvers with Aurora Thrusters, Magnetorquer and Reaction Wheels actutors.

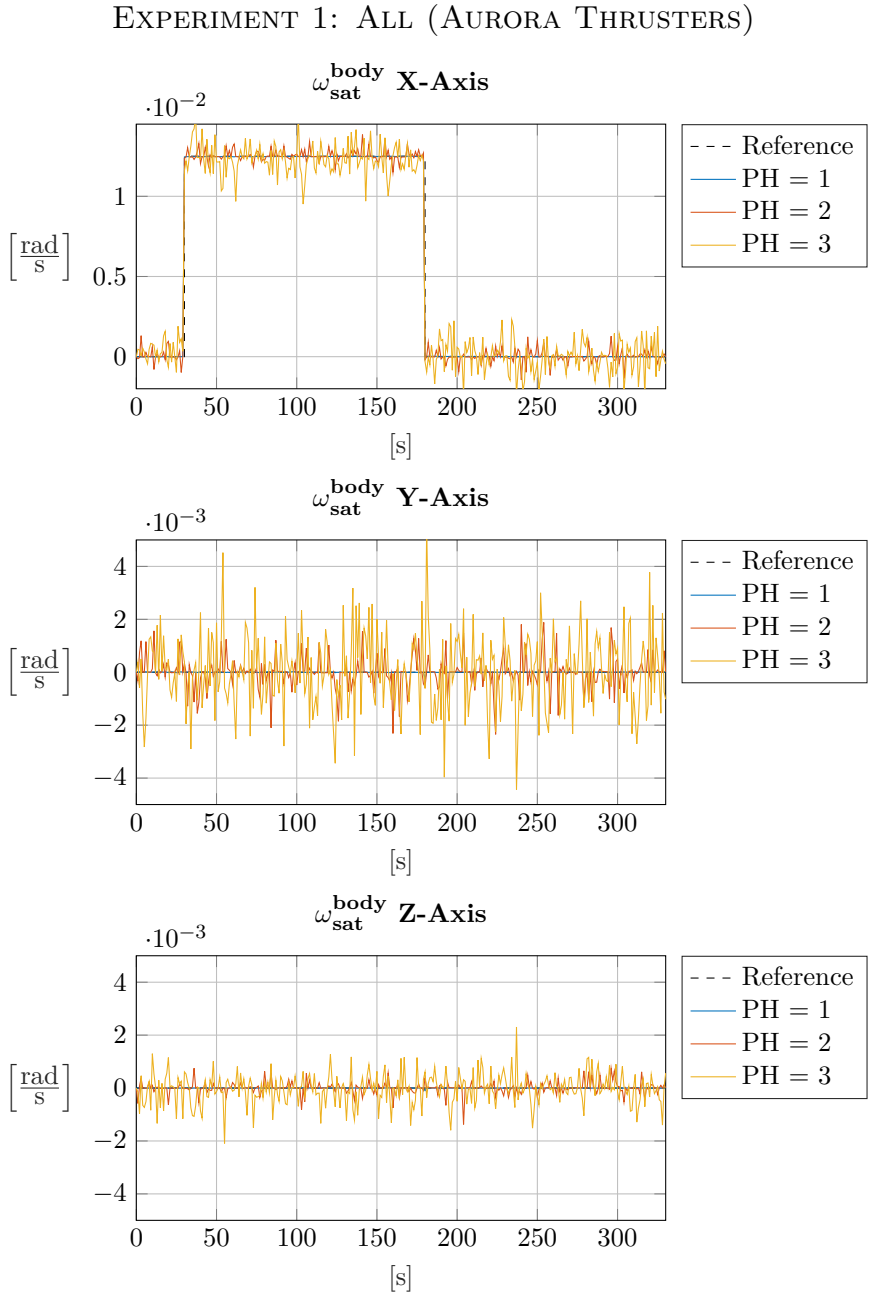

Figure 6.7: Satellite angular velocity response for different prediction horizon lengths. Represents small momentum maneuver with Aurora Thrusters, Magnetorquer and Reaction Wheels actutors.

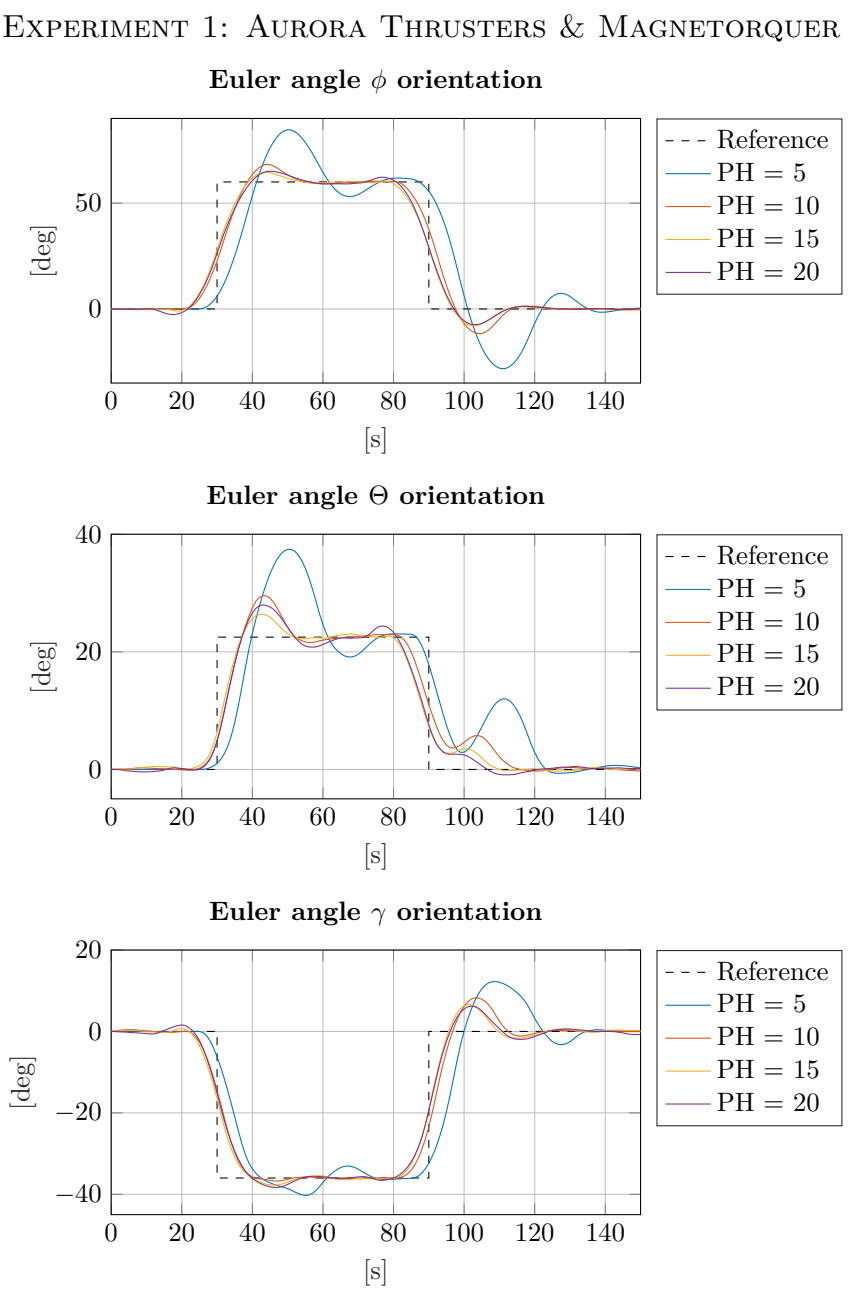

Figure 6.8: Satellite attitude responses based on different prediction horizon lengths, in large momentum maneuvers with Aurora Thrusters and Magnetorquer actutors. Measured in Euler ϕ, Θ and γ angles (*zyx* convention).

EXPERIMENT 1: AURORA THRUSTERS & MAGNETORQUER

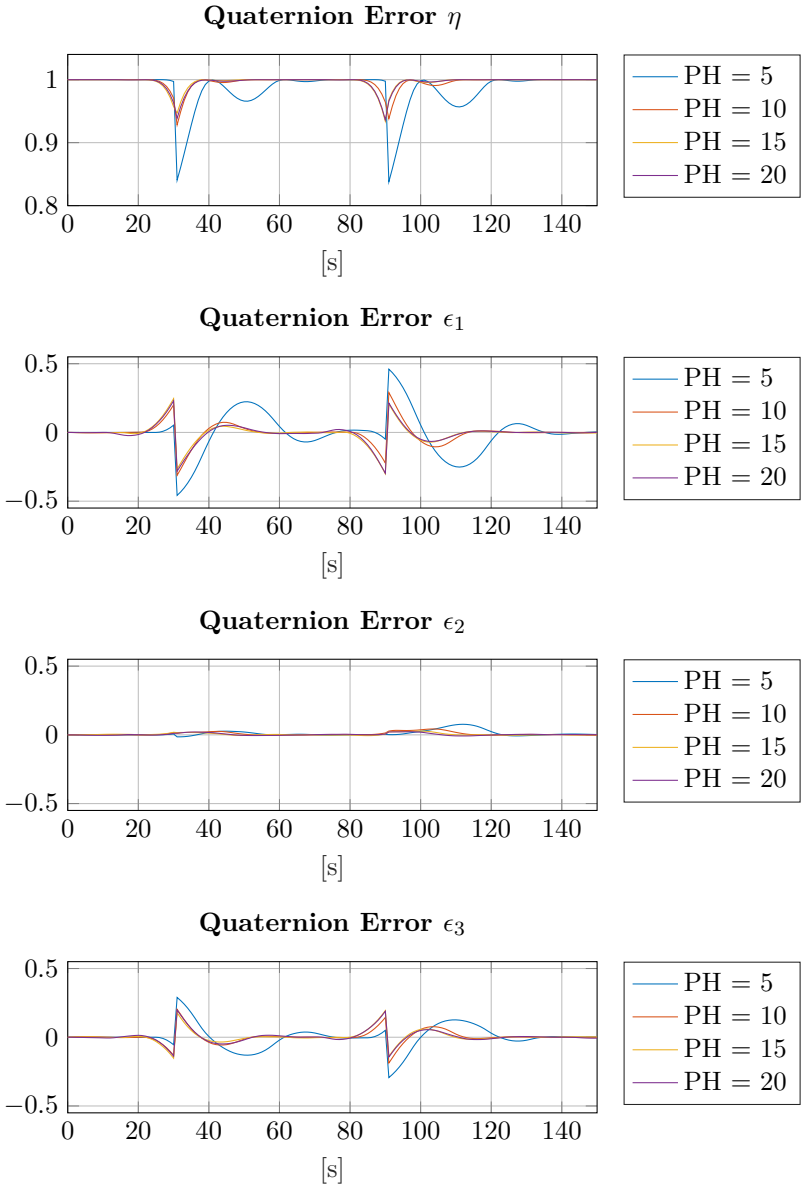

Figure 6.9: Attitude quaternion error based on different prediction horizon lengths, in large momentum maneuvers with Aurora Thrusters and Magnetorquer actutors.

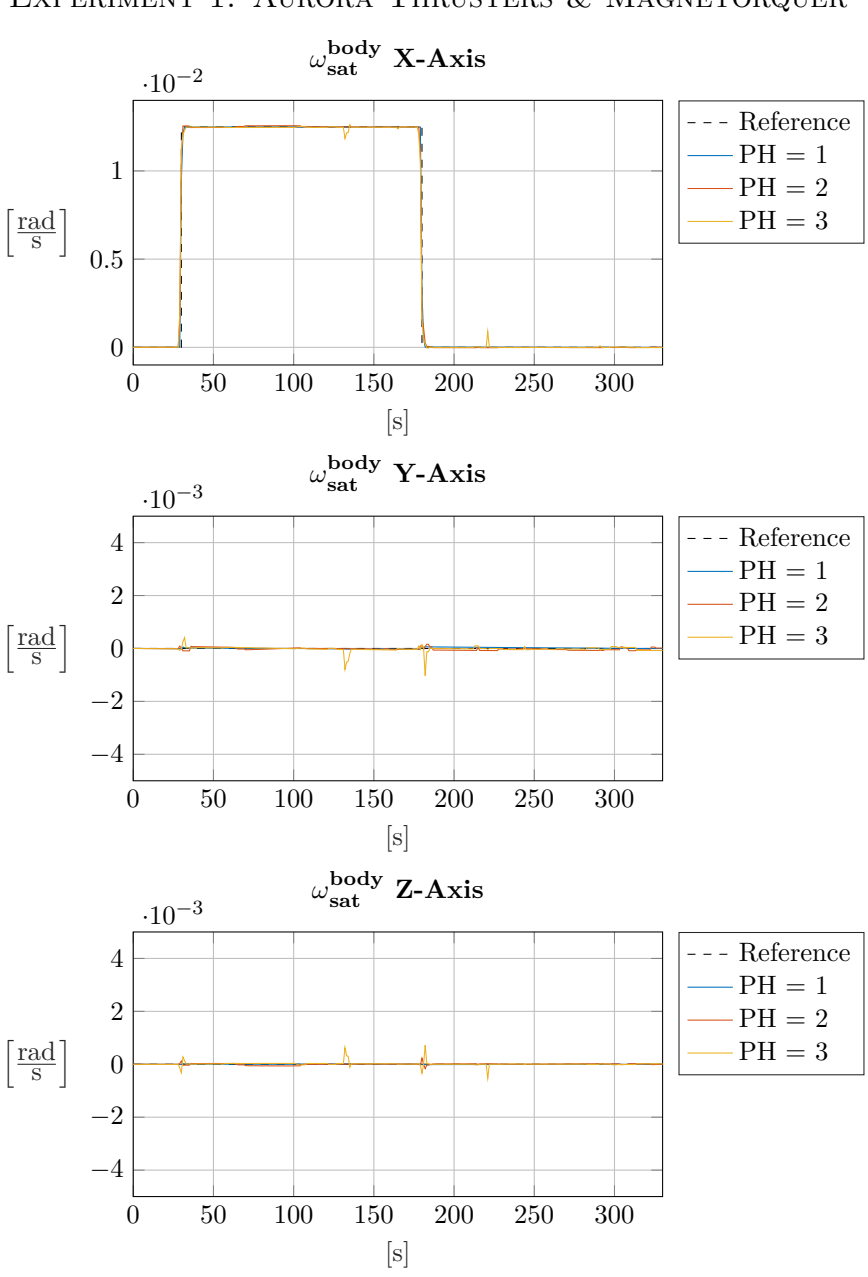

Figure 6.10: Satellite angular velocity response for different prediction horizon lengths. Represents small momentum maneuver with Aurora Thrusters and Magnetorquer actutors.

EXPERIMENT 1: NANOFEEP THRUSTERS & MAGNETORQUER

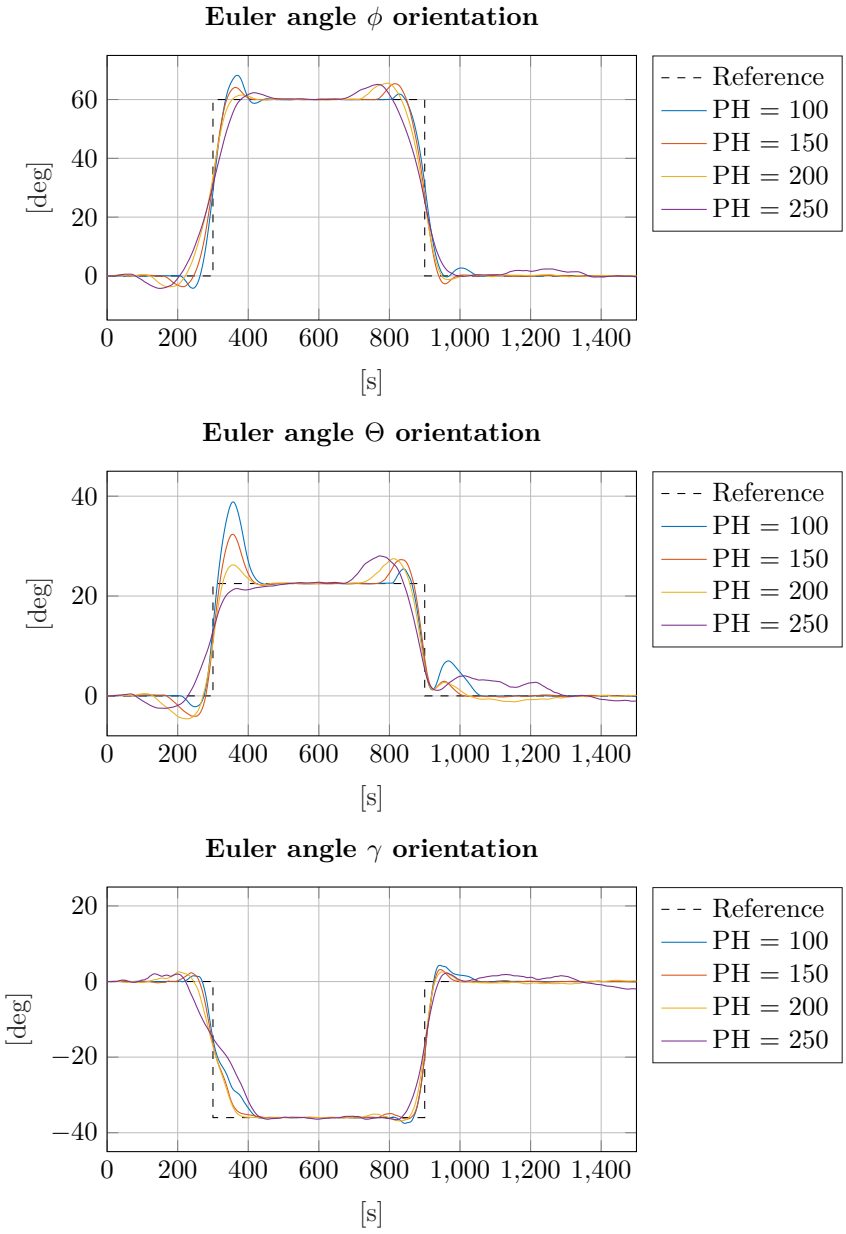

Figure 6.11: Satellite attitude responses based on different prediction horizon lengths, in large momentum maneuvers with NanoFEEP Thrusters and Magnetorquer actutors. Measured in Euler ϕ, Θ and γ angles (*zyx* convention).

Experiment 1: NanoFEEP Thrusters & Magnetorquer

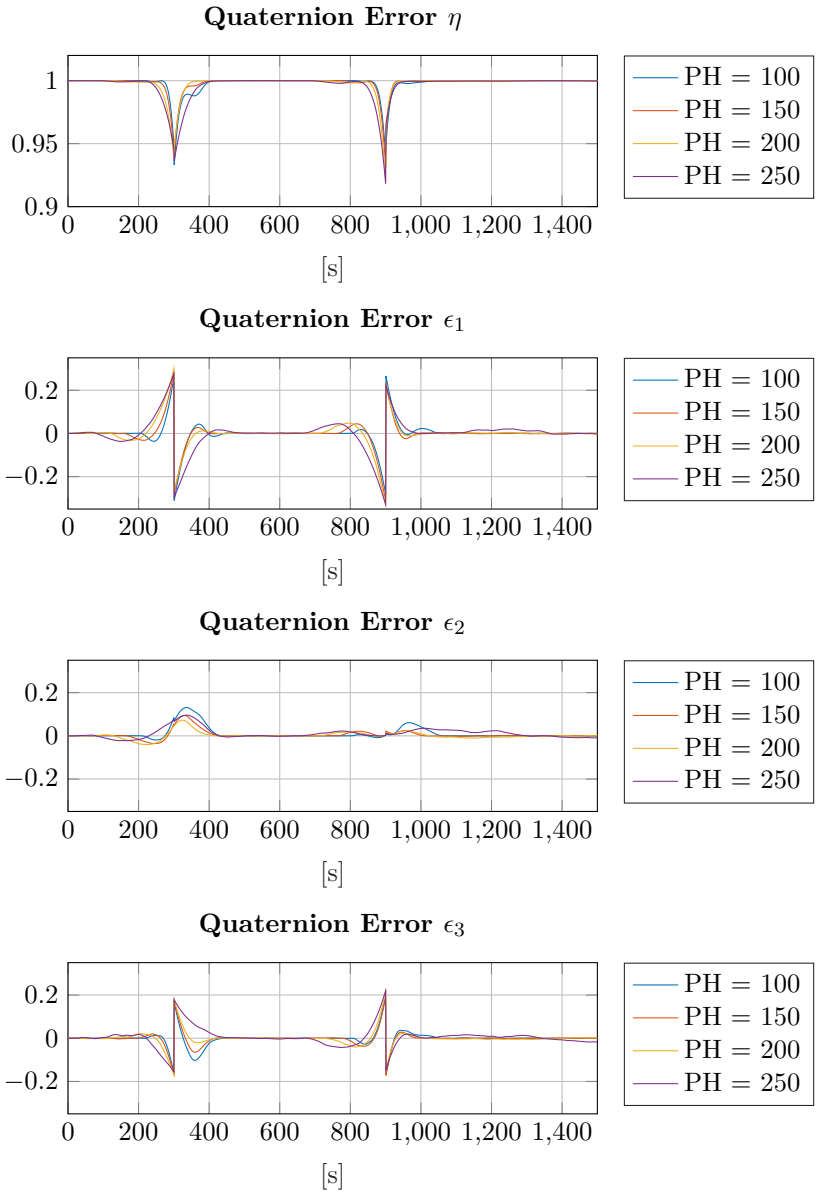

Figure 6.12: Attitude quaternion error based on different prediction horizon lengths, in large momentum maneuvers with NanoFEEP Thrusters and Magnetorquer actutors.

EXPERIMENT 1: NANOFEEP THRUSTERS & MAGNETORQUER

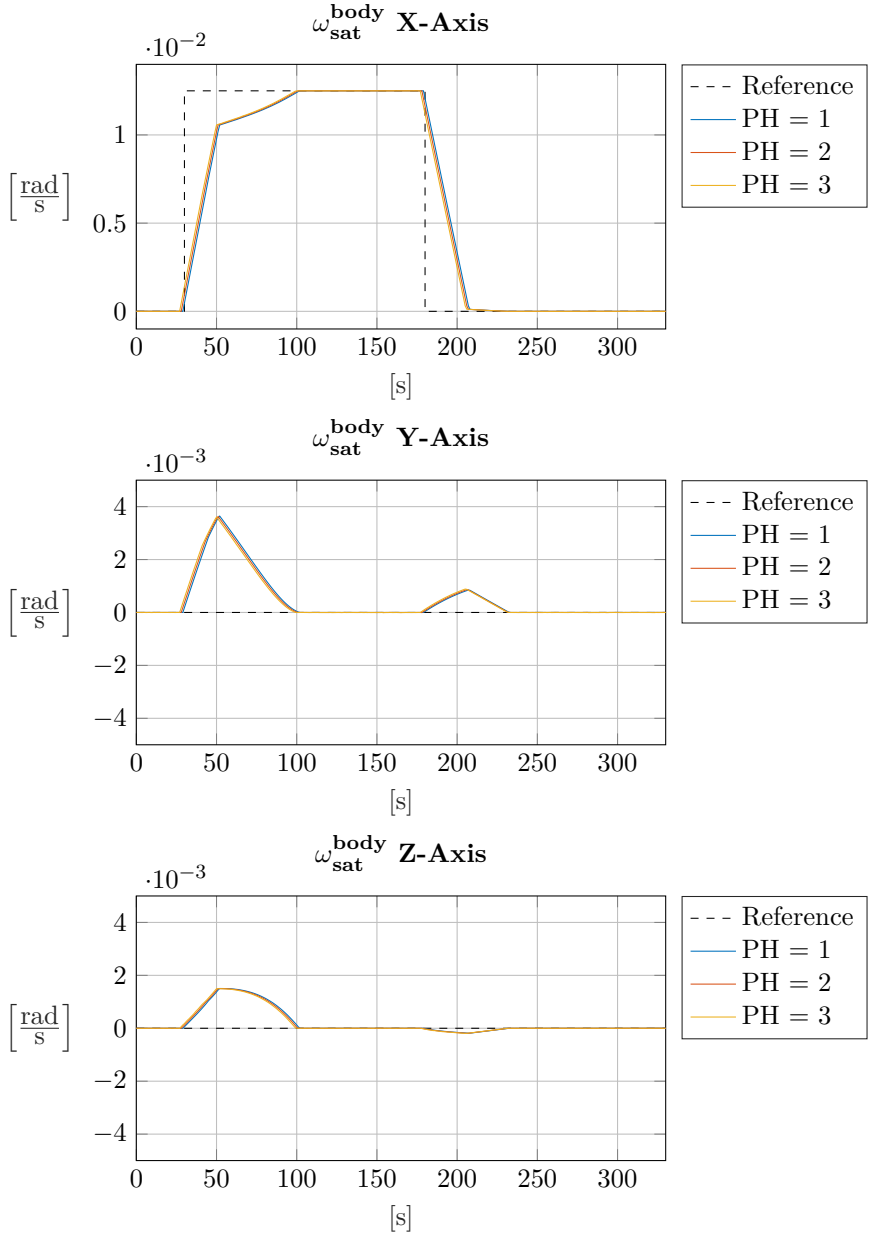

Figure 6.13: Satellite angular velocity response for different prediction horizon lengths. Represents small momentum maneuver with NanoFEEP Thrusters and Magnetorquer actutors.

6.3 Experiment 2

The second experiment was conducted to compare the performance of different actuators and controllers on rapid rest-to-rest slew maneuvers. In the experiment, the satellite had a reference attitude trajectory, presented in table 6.3. The initial conditions of the satellite are presented in table 6.4. Both an MPC and PD controller were used in the experiment, with the controller parameters given in table 6.5. The experiment is considered a large momentum maneuver, and as such, the corresponding MPC parameters from the previous experiment (6.2) are applied.

The results are divided into two subsections, 6.3.1 *Short duration simulations* and 6.3.2 *Long duration simulations*. The attitude dynamics of the satellite is much slower when actuated by the NanoFEEP propulsion system. To show the variation in performance of both the NanoFEEP propulsion system and the remaining actuators, the simulations and results of the NanoFEEP actuated system are presented in subsection 6.3.2 *Long duration simulations*, and the satellite response when actuated by the remaining actuators are presented in subsection 6.3.1 *Short duration simulations*.

The Root-Mean-Square error is calculated as in Equation (6.1).

$$\text{RMS} = \sqrt{\frac{1}{n}\sum_{i=0}^{n}\left(\boldsymbol{x}_i - \boldsymbol{x}_{Ref_i}\right)} \tag{6.1}$$

Experiment 2 Objectives	
Short Duration Reference Attitude Quaternion Trajectory	$\begin{cases} \begin{bmatrix} 1 & 0 & 0 & 0 \end{bmatrix}', & t \in [0, 30), \\ \begin{bmatrix} 0.7777 \\ 0.5186 \\ 0.0091 \\ -0.3552 \end{bmatrix}, & t \in [30, 90), \\ \begin{bmatrix} 1 & 0 & 0 & 0 \end{bmatrix}', & t = [90, \infty). \end{cases}$
Long Duration Reference Attitude Quaternion Trajectory	$\begin{cases} \begin{bmatrix} 1 & 0 & 0 & 0 \end{bmatrix}', & t \in [0, 300), \\ \begin{bmatrix} 0.7777 \\ 0.5186 \\ 0.0091 \\ -0.3552 \end{bmatrix}, & t \in [300, 900), \\ \begin{bmatrix} 1 & 0 & 0 & 0 \end{bmatrix}', & t = [900, \infty). \end{cases}$
Reference Reaction Wheel Velocities	$1000 \text{ RPM} \cdot \begin{bmatrix} 1 & 1 & 1 & 1 \end{bmatrix}'$

Table 6.3: Objectives of Experiment 2.

6.3.1 Short duration simulations

The short duration simulations lasted for 150s and concerned the Reaction Wheels, Magnetorquer, and Aurora thruster systems.

Experiment 2 Initial Conditions	
Time	12:00:00 31.10.2005
Periapsis, Apoapsis	500 km, 500 km
Inclination	97 deg
Right Ascension of the Ascending Node	0 deg
Argument of Perigee	0 deg
True Anomaly	45 deg
Initial Attitude Quaternion	$\begin{bmatrix}1 & 0 & 0 & 0\end{bmatrix}'$
Initial Rotational Velocity	$\begin{bmatrix}0 & 0 & 0\end{bmatrix}'$
Initial Reaction Wheel Velocities	$\begin{bmatrix}0 & 0 & 0 & 0\end{bmatrix}'$

Table 6.4: Initial Satellite Conditions in Experiment 2.

Satellite Attitude Response

Figure 6.14 presents the step response of the satellite attitude, measured in Euler angles using the *zyx* convention. A closer look at the attitude response is provided in Figure 6.15. The step response is simulated by initializing the satellite in the given orientation and feeding the reference attitude trajectory. The details of this is provided in tables 6.3 and 6.4. Figure 6.16 presents the attitude quaternion deviation between the satellite and the reference trajectory.

The average settling time and Root-Mean-Square errors are presented in table 6.6. The settling time is defined as the period from a change in the reference

Experiment 2 Controller Parameters								
MPC	Freq.	PH	ζ_a	ζ_ω	ζ_m	κ_{MTQ}	κ_T	κ_{RW}
All (Aurora)	1 Hz	3	10^{15}	0	10^6	1	10^{14}	10^6
RW, MTQ	1 Hz	3						
Aurora, MTQ	1 Hz	15	10^{15}	0	0	1	10^{14}	0
NanoFEEP, MTQ	1 Hz	150	10^{15}	0	0	1	10^9	0
PD	Freq.	K_p	K_d	K_{dd}				
Only RW	10 Hz	10	10	0				

Table 6.5: Parameters used in Experiment 2 for the Model Predictive and Proportional-Derivative Controllers. The frequency parameter governs how often the control signals are updated. The PH parameter sets the length of the Prediction Horizon in the MPC. The cost of the attitude deviation is given by ζ_a, angular velocity deviation by ζ_ω, and the cost of the reaction wheel momentum deviation is given by ζ_m. κ_{MTQ}, κ_T, and κ_{RW} are the factors by which the Magnetorquer, Thruster and Reaction Wheels actuation weights are multiplied by, respectively. The K_p parameter is the term assigned to the attitude deviation, K_d is assigned to the angular velocity deviation, and K_{dd} is assigned to the angular acceleration deviation.

signal is applied to the η value of the attitude error quaternion remains within $1 \cdot 10^{-5}$ from the unit value.

Experiment 2 Short Duration Performance Measures			
	Total RMS Error	RMS Error Post Settled	Average Settling Time [s]
RW PD	$3.5474 \cdot 10^{-2}$	$9.3053 \cdot 10^{-7}$	10.4
All (Aurora)	$7.2811 \cdot 10^{-3}$	$8.0111 \cdot 10^{-7}$	9.0
Aurora, MTQ	$1.0852 \cdot 10^{-2}$	$1.3034 \cdot 10^{-5}$	36.5
RW, MTQ	$7.2213 \cdot 10^{-3}$	$1.9401 \cdot 10^{-7}$	9.0

Table 6.6: Root-Mean-Square and Settling Time Measures for the Short Duration Simulations in Experiment 2.

Actuator Response

The reaction wheels velocities are presented in Figure 6.18. The MPC's ability to regulate both the desired attitude and reaction wheel momentum compared to the PD controller is visible in these plots. Figures 6.19 and 6.20 present the force applied by the induvidual thrusters in the Aurora propulsion system. The propellant consumption is presented in figure 6.21. The applied magnetic dipoles of the magnetorquer in the different scenarios are presented in Figure 6.22.

6.3.2 Long duration simulations

The results in this subsection are obtained by using the NanoFEEP propulsion system for attitude control, which results in slower satellite attitude dynamics.

Satellite Attitude Response

The satellite attitude, measured in Euler angles using the *zyx* convention, is presented in Figure 6.23. Figure 6.25 presents the attitude quaternion error used by the MPC to calculate the actuation gains.

The average settling time and Root-Mean-Square errors are presented in table 6.7. The settling time is again defined as the period from a change in the reference signal is applied to the η value of the attitude error quaternion remains within $1 \cdot 10^{-5}$ from the unit value, as was the case for the short-duration simulations.

Experiment 2 Long Duration Performance Measures			
	Total RMS Error	RMS Error Post Settled	Average Settling Time [s]
NanoFEEP, MTQ	$7.8778 \cdot 10^{-3}$	$1.8440 \cdot 10^{-6}$	108.5

Table 6.7: Root-Mean-Square and Settling Time Measures for the Long Duration Simulations in Experiment 2.

Actuator Response

The propellant consumption of the NanoFEEP thrusters is presented in Figure 6.26. The total propellant consumption of the NanoFEEP thrusters is approximately 3 μg, compared to about 1300 μg of the Aurora system. The applied magnetic dipoles of the magnetorquer are presented in Figure 6.27.

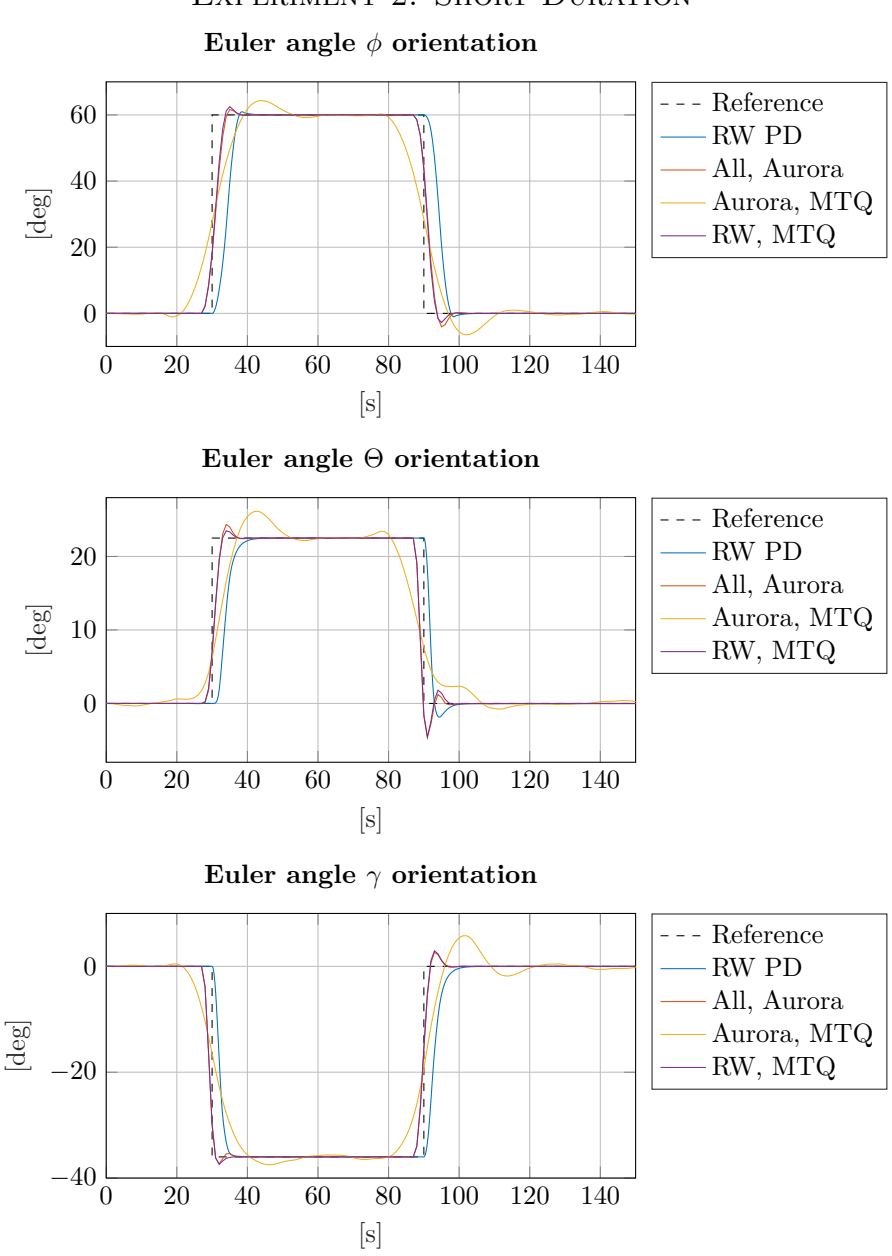

Figure 6.14: Satellite attitude response in Short Duration Experiment 2, measured in Euler ϕ, Θ and γ angles (*zyx* convention).

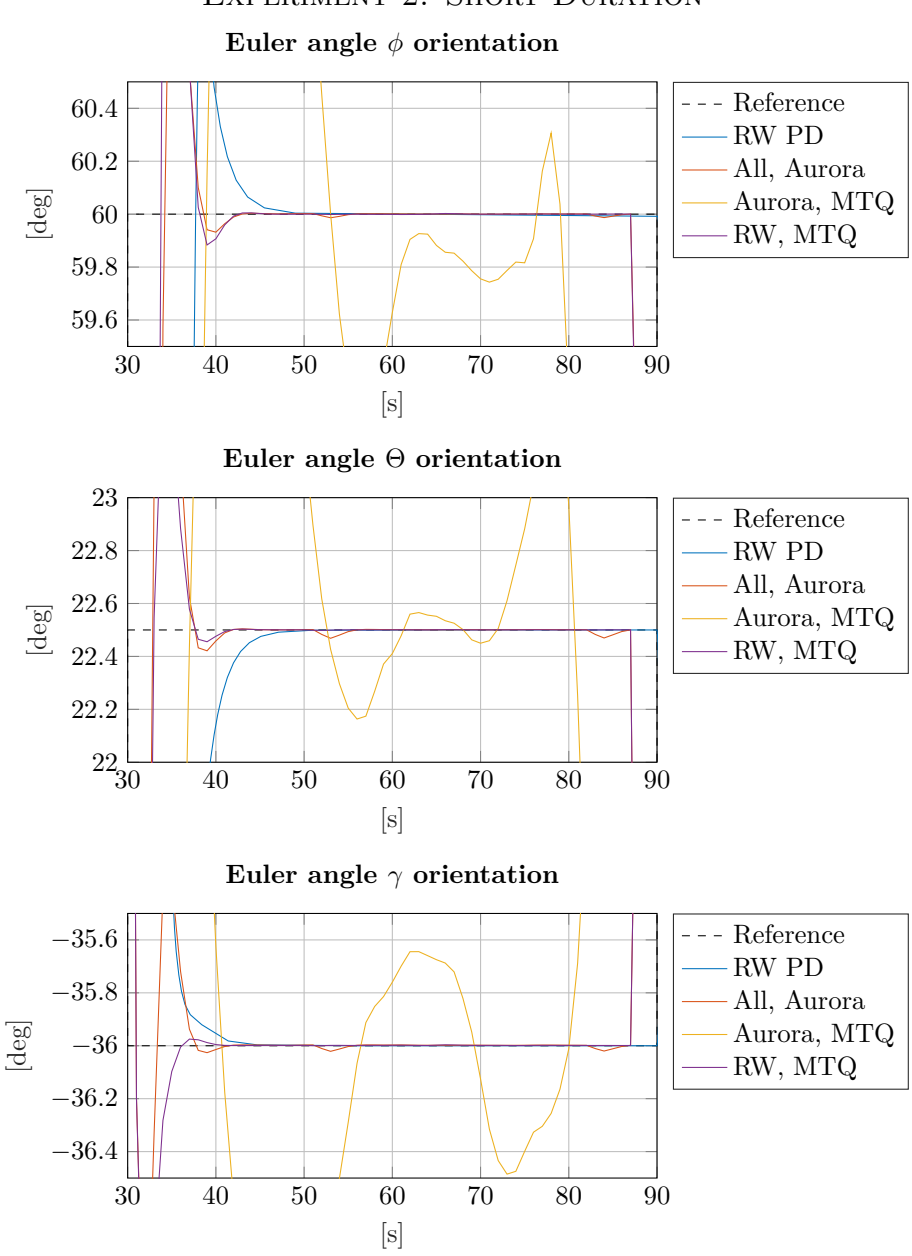

Figure 6.15: Satellite attitude response in Short Duration Experiment 2, measured in Euler ϕ, Θ and γ angles (*zyx* convention).

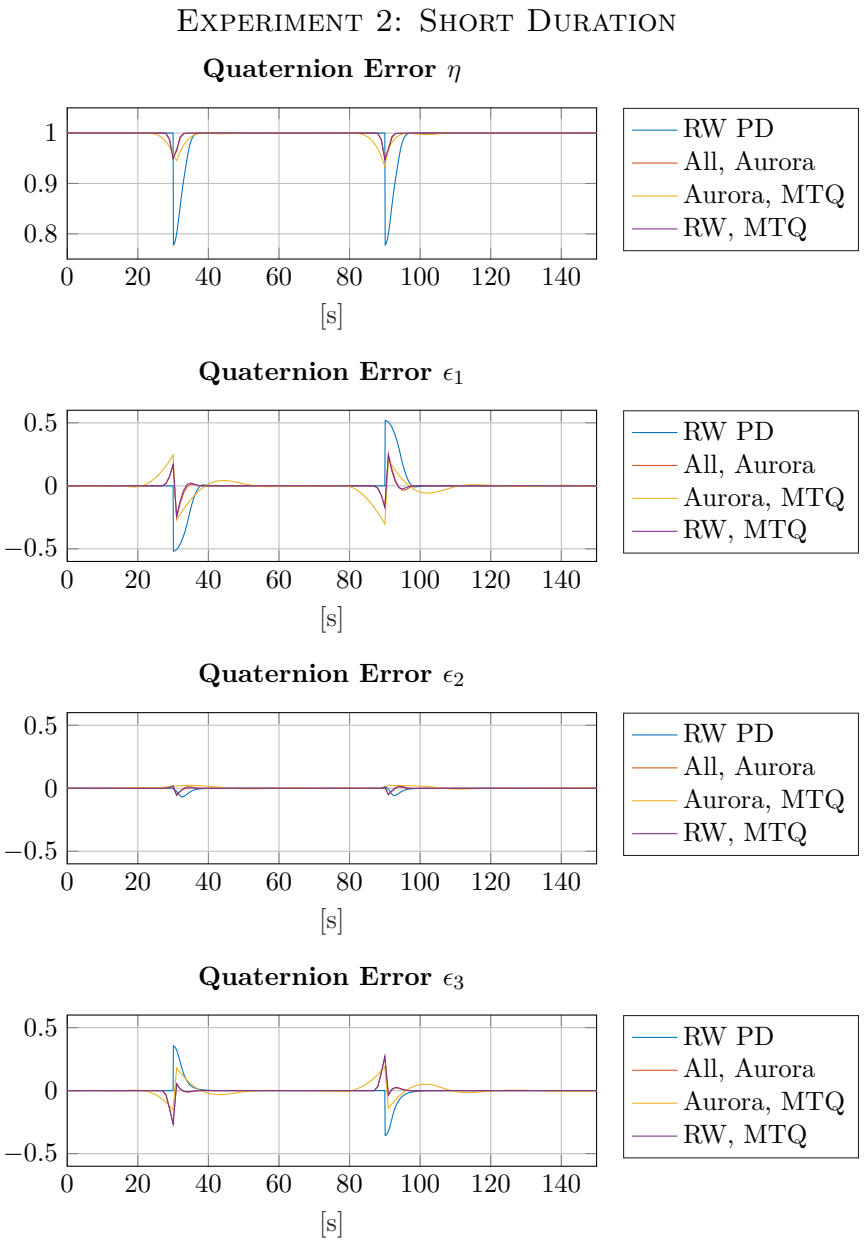

Figure 6.16: Attitude quaternion deviation in Short Duration Experiment 2.

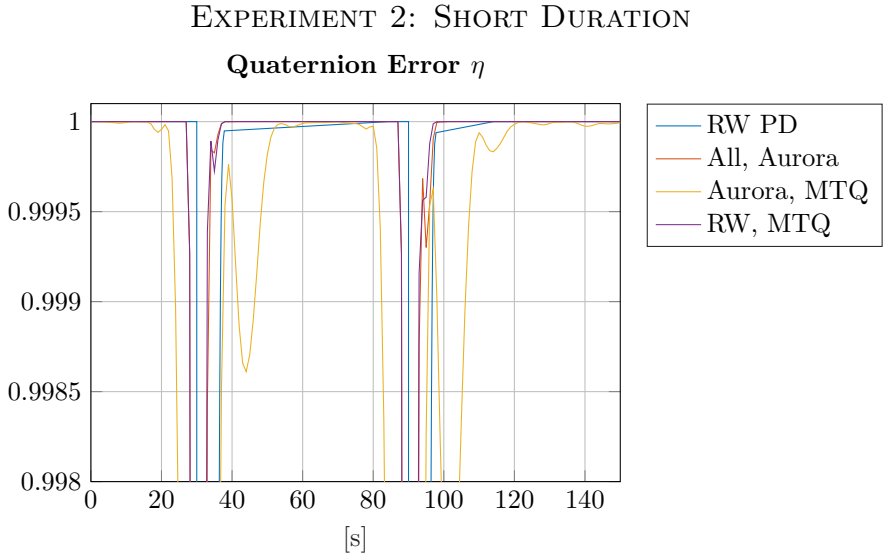

Figure 6.17: Attitude quaternion deviation in Short Duration Experiment 2.

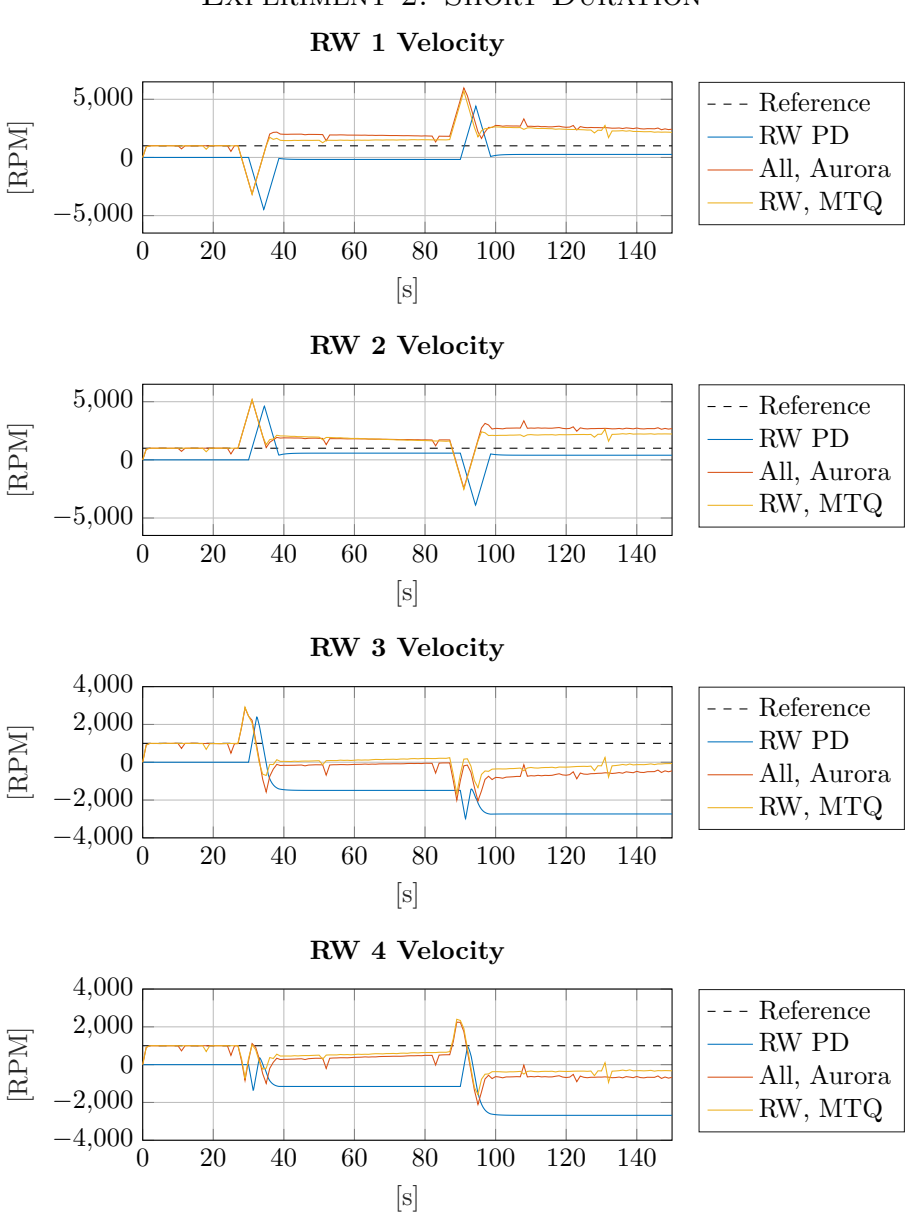

Figure 6.18: Reaction wheels velocities in Short Duration Experiment 2 given in the wheel frame for the different actuation scenarios.

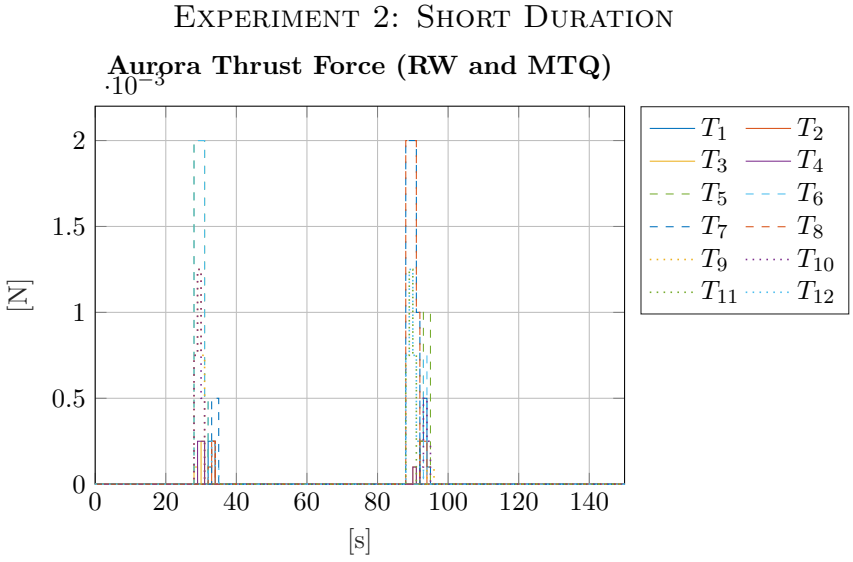

Figure 6.19: Force applied by the individual thrusters of the Aurora propulsion system in Short Duration Experiment 2, when following a reference attitude trajectory in combination with reaction wheels and magnetorquer actuators.

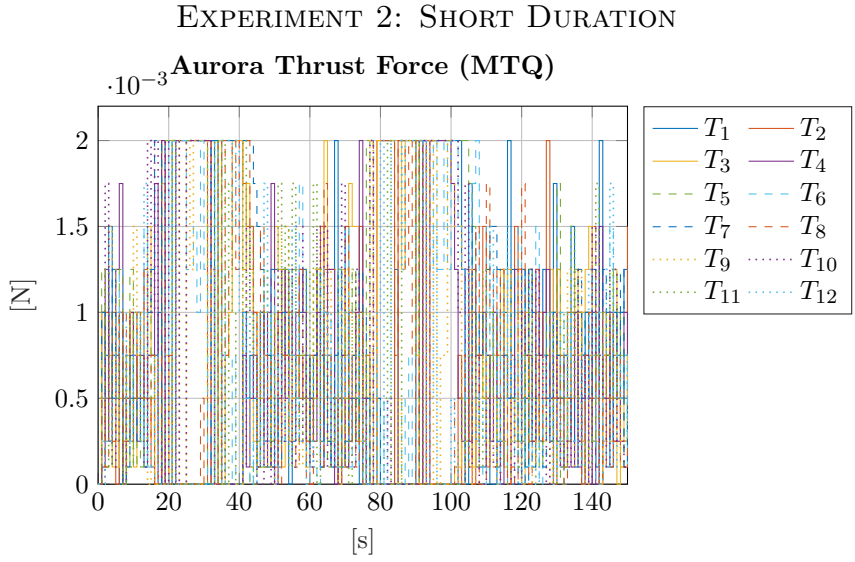

Figure 6.20: Force applied by the individual thrusters of the Aurora propulsion system in Short Duration Experiment 2, when following a reference attitude trajectory in combination with a magnetorquer.

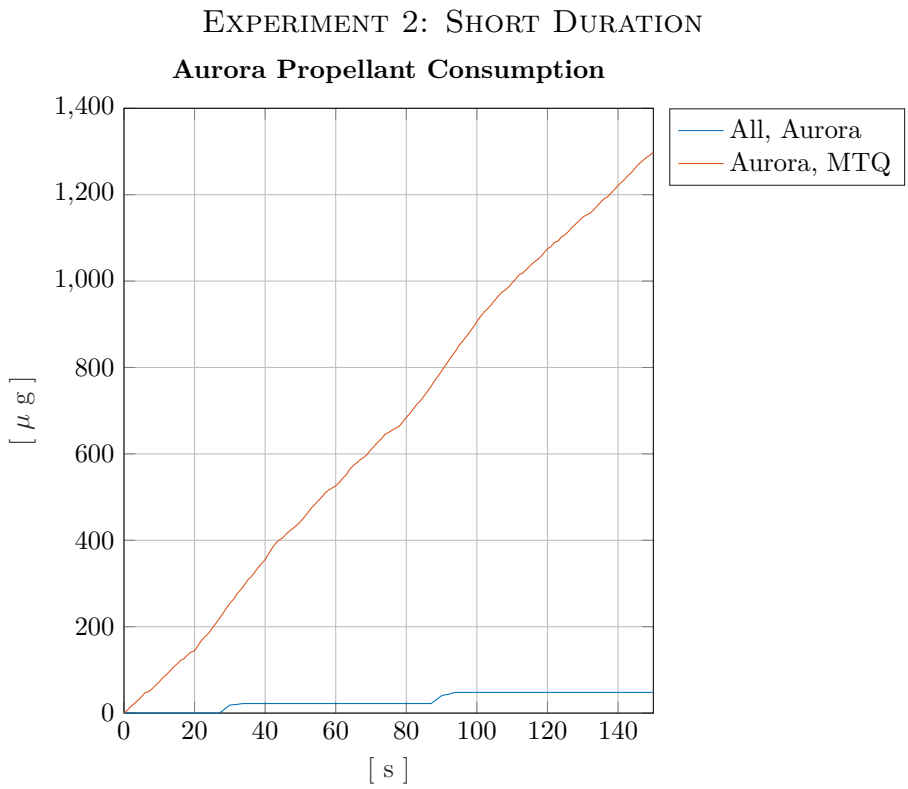

Figure 6.21: Cumulative representation of propellant consumption of the Aurora propulsion system in Short Duration Experiment 2.

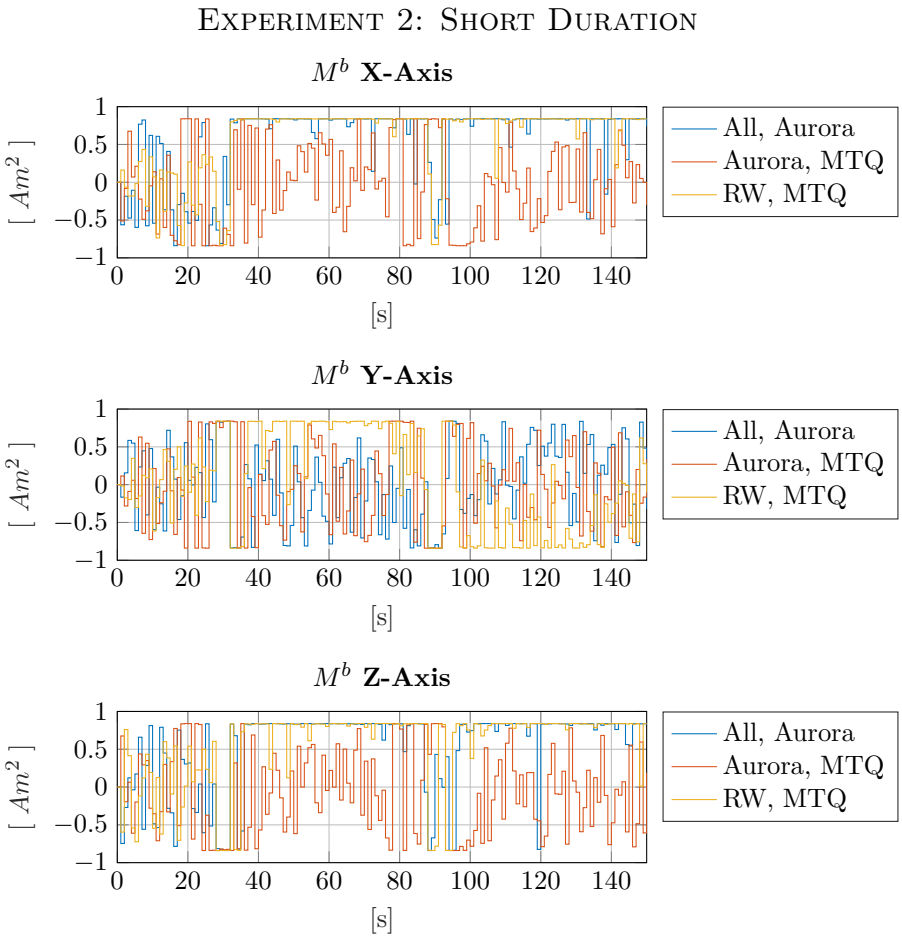

Figure 6.22: Dipole strengths applied by the magnetorquer actuator in Short Duration Experiment 2.

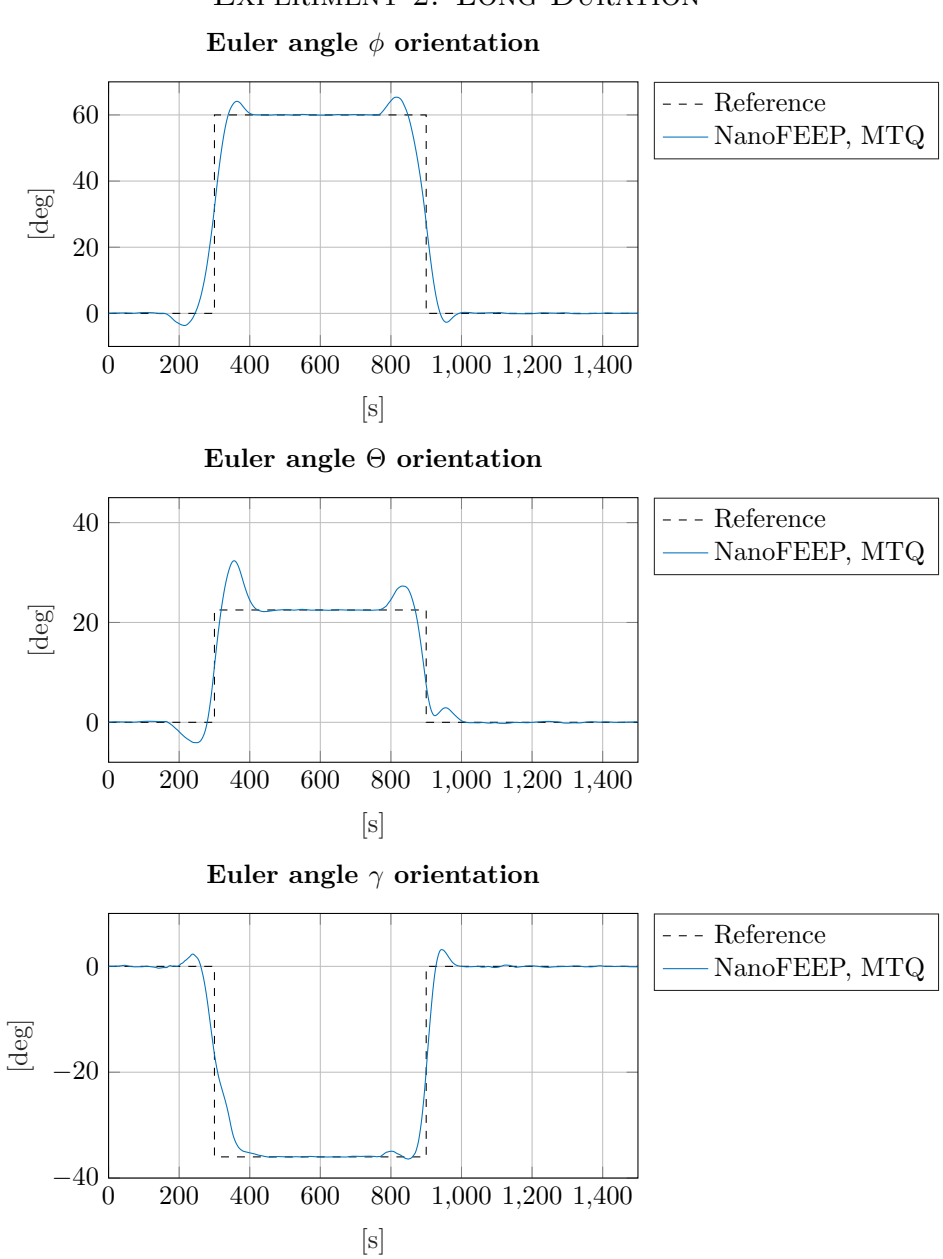

Figure 6.23: Satellite attitude response in Long Duration Experiment 2, measured in Euler ϕ, Θ and γ angles (*zyx* convention).

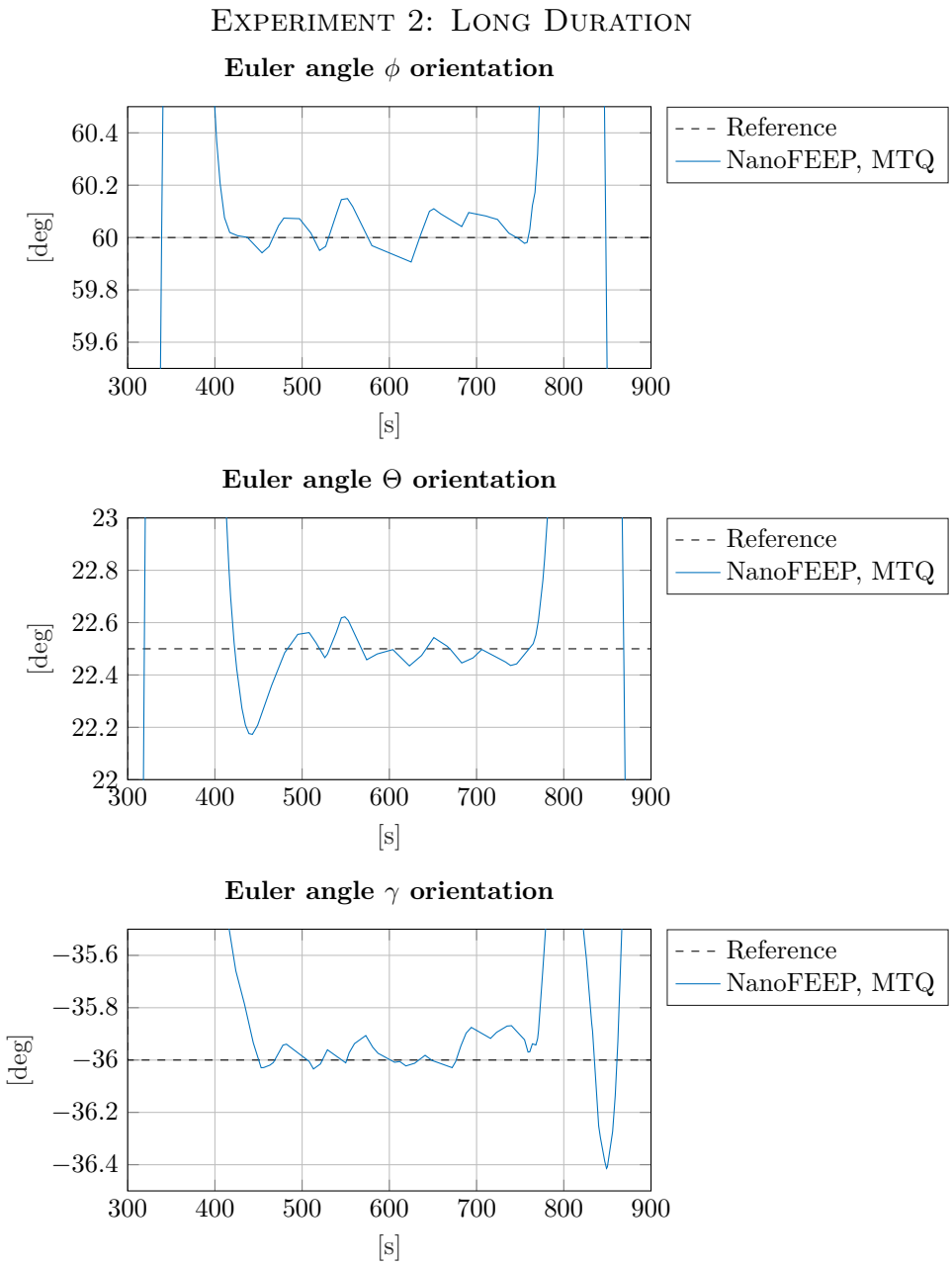

Figure 6.24: Satellite attitude response in Long Duration Experiment 2, measured in Euler ϕ, Θ and γ angles (*zyx* convention).

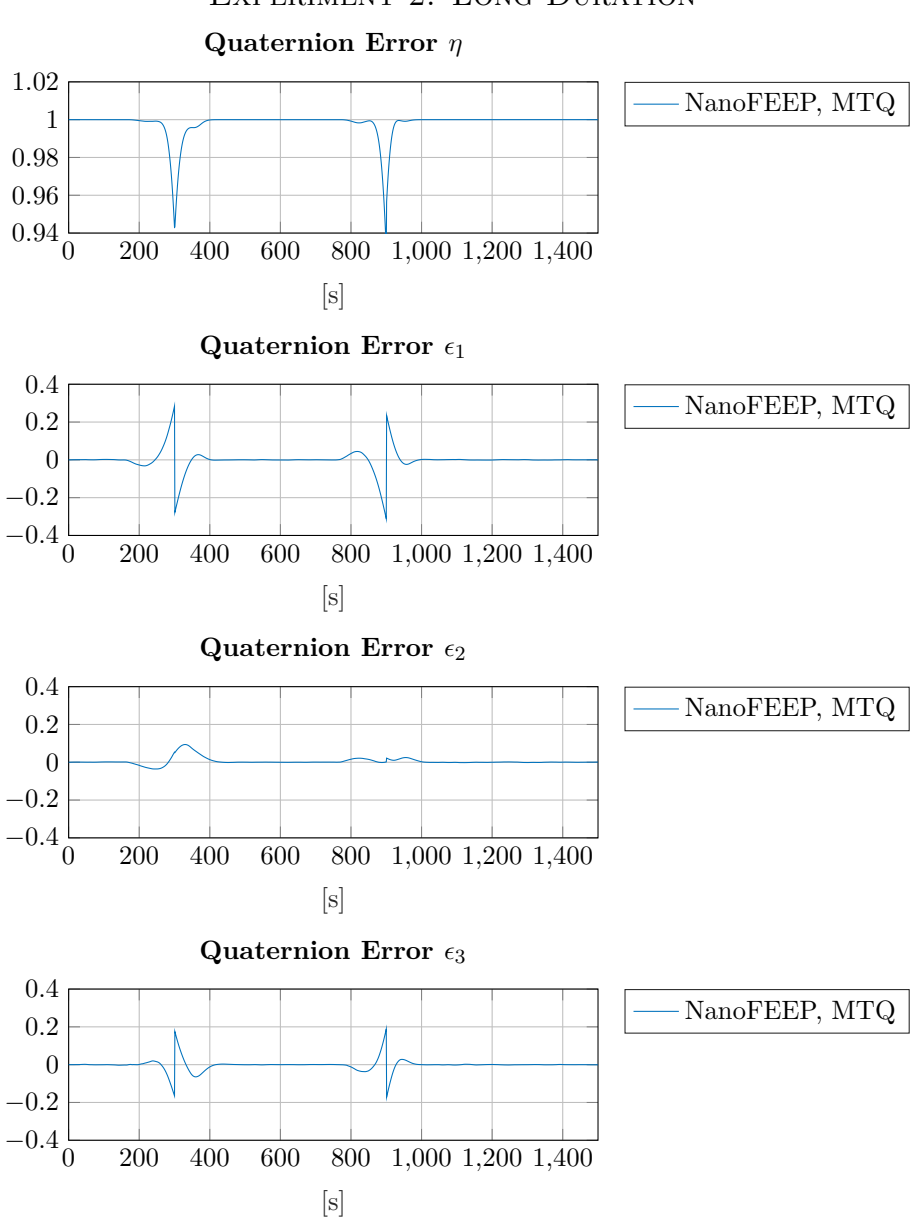

Figure 6.25: Attitude quaternion deviation in Long Duration Experiment 2.

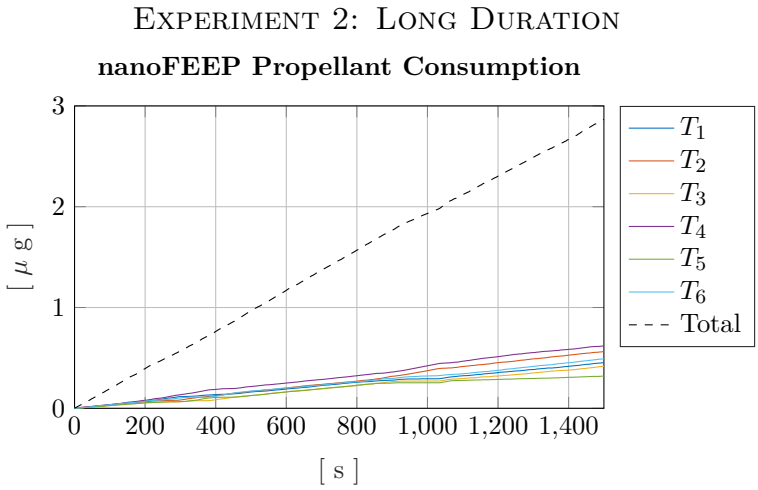

Figure 6.26: Cumulative representation of propellant consumption of the NanoFEEP propulsion system in Long Duration Experiment 2.

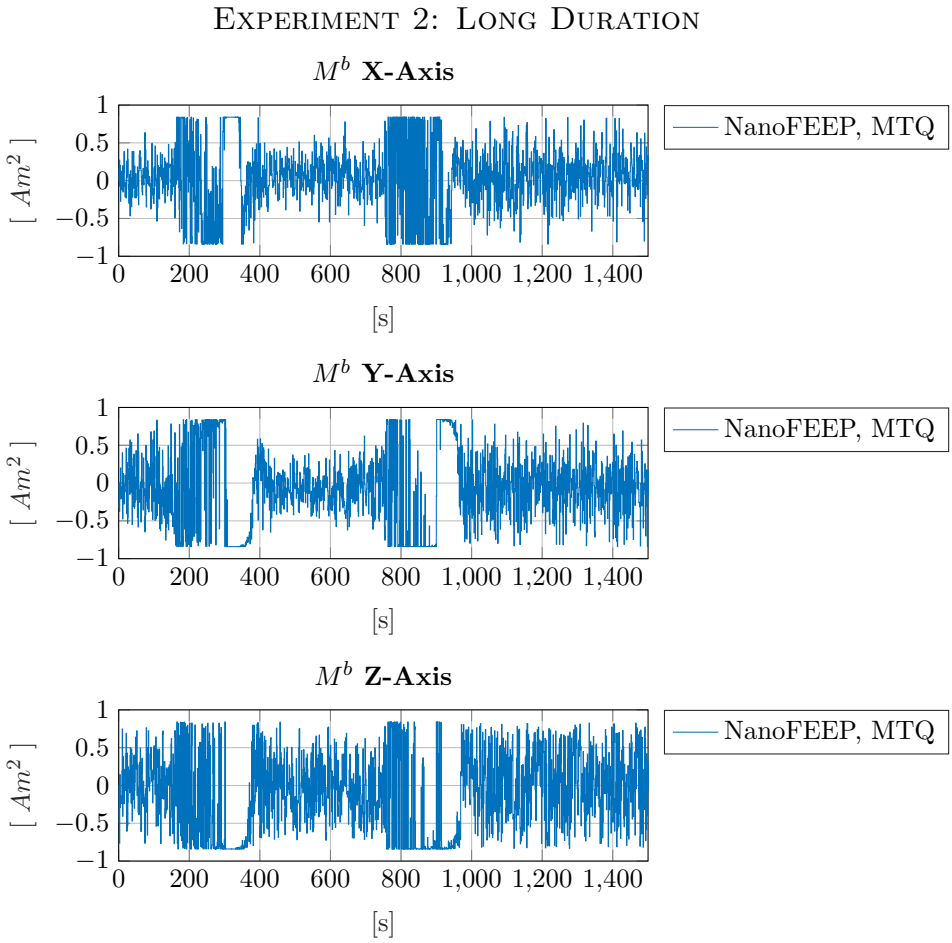

Figure 6.27: Dipole Strengths Applied by the Magnetorquer Actuator in the Long Duration Simulation of Experiment 2.

6.4 Experiment 3

The third experiment's objective is to measure the performance of the actuators and controllers in tracking reference slew rates. This measure is vital for the NTNU HYPSO mission, as data acquisition is made through precision slew maneuvers in which the camera lens is swept over designated land areas.

The initial satellite conditions in this experiment are the same as in previous experiments, presented in table 6.4. The reference angular velocity trajectory is given in table 6.8. Both the MPC and PD controller were applied, with the parameters given in table 6.9.

Experiment 3 Objectives	
Reference Angular Velocity	$\begin{cases} \begin{bmatrix} 0 & 0 & 0 \end{bmatrix}', & t \in [0, 30) \\ \begin{bmatrix} 0.0125 & 0 & 0 \end{bmatrix}', & t \in [30, 90) \\ \begin{bmatrix} 0 & 0 & 0 \end{bmatrix}', & t = [90, \infty) \end{cases}$
Reference Reaction Wheel Velocities	$1000 \text{ RPM} \cdot \begin{bmatrix} 1 & 1 & 1 & 1 \end{bmatrix}'$

Table 6.8: Reference Angular Velocity of the Satellite and Reaction Wheels in Experiment 3.

Experiment 3 Controller Parameters								
MPC	Freq.	PH	ζ_a	ζ_ω	ζ_m	κ_{MTQ}	κ_T	κ_{RW}
RW, MTQ	1 Hz	1	0	10^{15}	10^4	1	0	10^6
NanoFEEP, MTQ	1 Hz	1	0	10^{15}	10^4	1	10^9	10^6
Aurora, MTQ	1 Hz	1	0	10^{15}	0	10^3	10^{12}	0
All (Aurora)	1 Hz	1	0	10^{15}	$5 \cdot 10^5$	10^3	10^{12}	10^8
PD	Freq.	K_p	K_d	K_{dd}				
Only RW	10 Hz	0	10	0.1				

Table 6.9: Parameters used in Experiment 3 for the Model Predictive and Proportional-Derivative Controllers. The frequency parameter governs how often the control signals are updated. The PH parameter sets the length of the Prediction Horizon in the MPC. The cost of the attitude deviation is given by ζ_a, angular velocity deviation by ζ_ω, and the cost of the reaction wheel momentum deviation is given by ζ_m. κ_{MTQ}, κ_T, and κ_{RW} are the factors by which the Magnetorquer, Thruster and Reaction Wheels actuation weights are multiplied by, respectively. The K_p parameter is the term assigned to the attitude deviation, K_d is assigned to the angular velocity deviation, and K_{dd} is assigned to the angular acceleration deviation.

Satellite Slew Rate Response

The satellite angular velocity is plotted together with the reference trajectory in Figure 6.28. Figure 6.29 provides a closer look at the transient period of the actuators, and Figure 6.30 provides a closer look at the steady state precisions.

The average settling times and Root-Mean-Square errors are presented in table 6.10. The settling time is defined as the period from the reference signal is applied to the angular velocity deviation remains less than $5 \cdot 10^{-5}$ $\frac{\text{rad}}{\text{s}}$.

Experiment 3 Performance Measures			
	Total RMS Error	RMS Error Post Settled	Average Settling Time [s]
RW PD	$3.4250 \cdot 10^{-4}$	$8.0094 \cdot 10^{-8}$	0.5
All (Aurora)	$3.8345 \cdot 10^{-5}$	$1.8208 \cdot 10^{-5}$	1.0
Aurora, MTQ	$2.7485 \cdot 10^{-4}$	$4.8359 \cdot 10^{-5}$	3.0
NanoFEEP, MTQ	$4.4044 \cdot 10^{-3}$	$1.0204 \cdot 10^{-6}$	57.0
RW, MTQ	$2.7888 \cdot 10^{-5}$	$2.6833 \cdot 10^{-5}$	0.0

Table 6.10: Root-Mean-Square and Settling Time Measures for Experiment 3.

Actuator Response

The reaction wheel velocities are presented in Figure 6.31. Figures 6.32 show the thrust force applied by the Aurora propulsion system, with the propellant consumption given in Figure 6.33. The thrust force applied by the NanoFEEP propulsion system is given in Figure 6.34, with the propellant consumption provided in Figure **??**. Finally, the magnetic dipoles applied by the magnetorquer are provided in Figure 6.35.

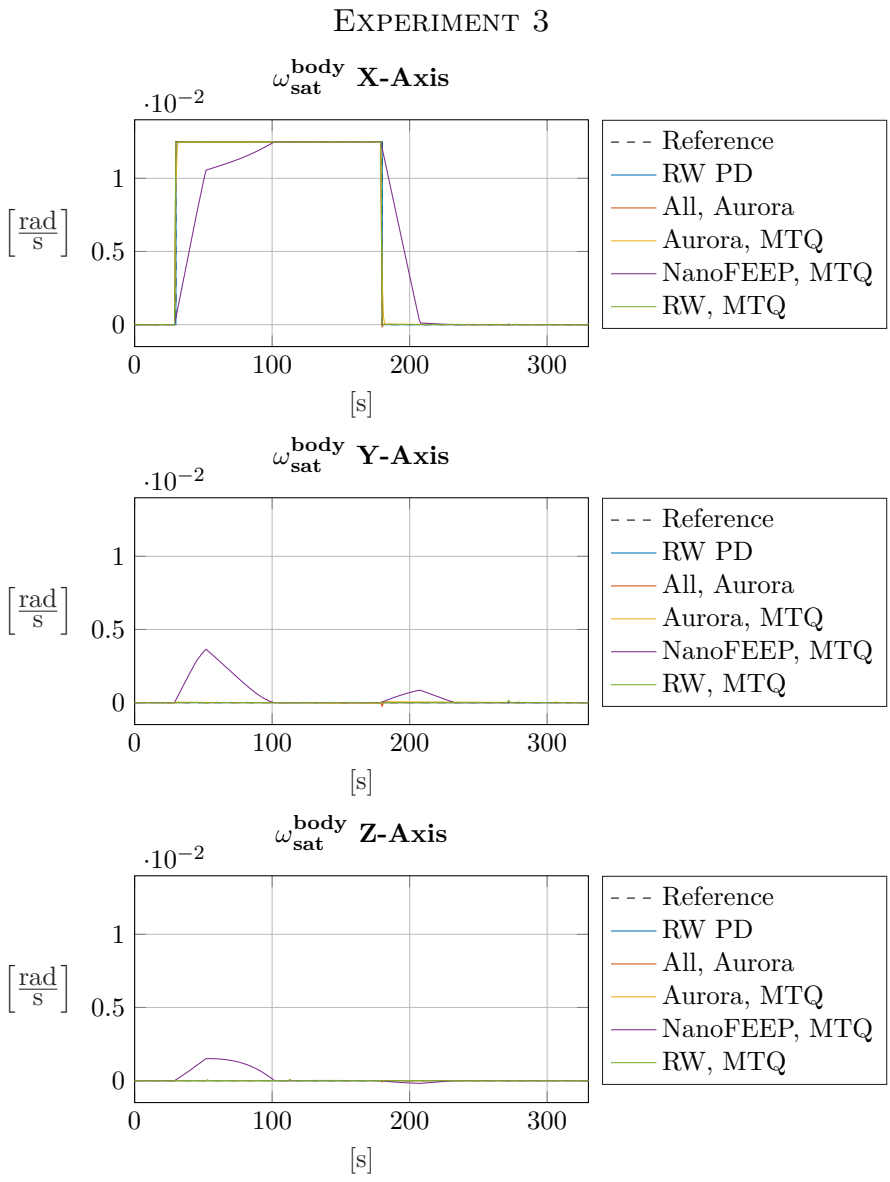

Figure 6.28: Angular Velocities in Satellite Body Frame of Experiment 3.

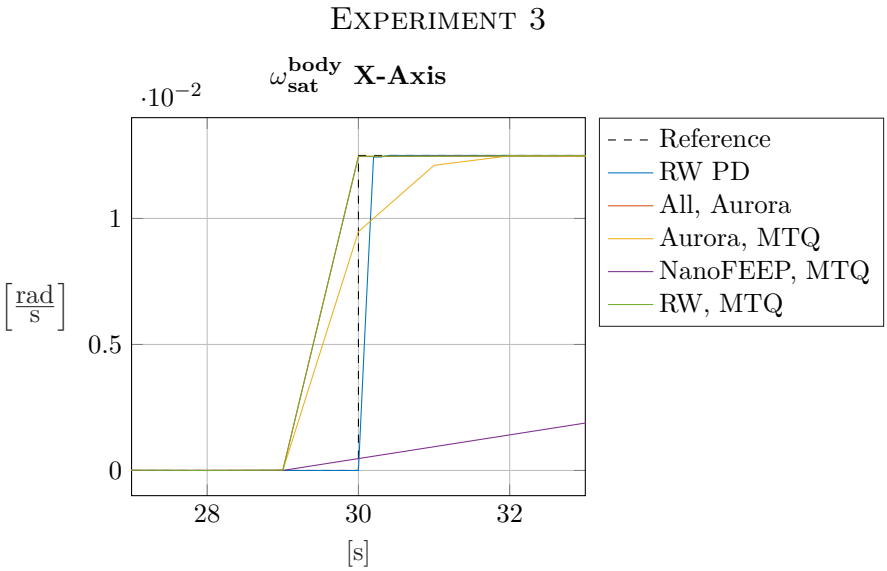

Figure 6.29: Magnification of the Step Response in Satellite Body Frame Angular Velocity of Experiment 3.

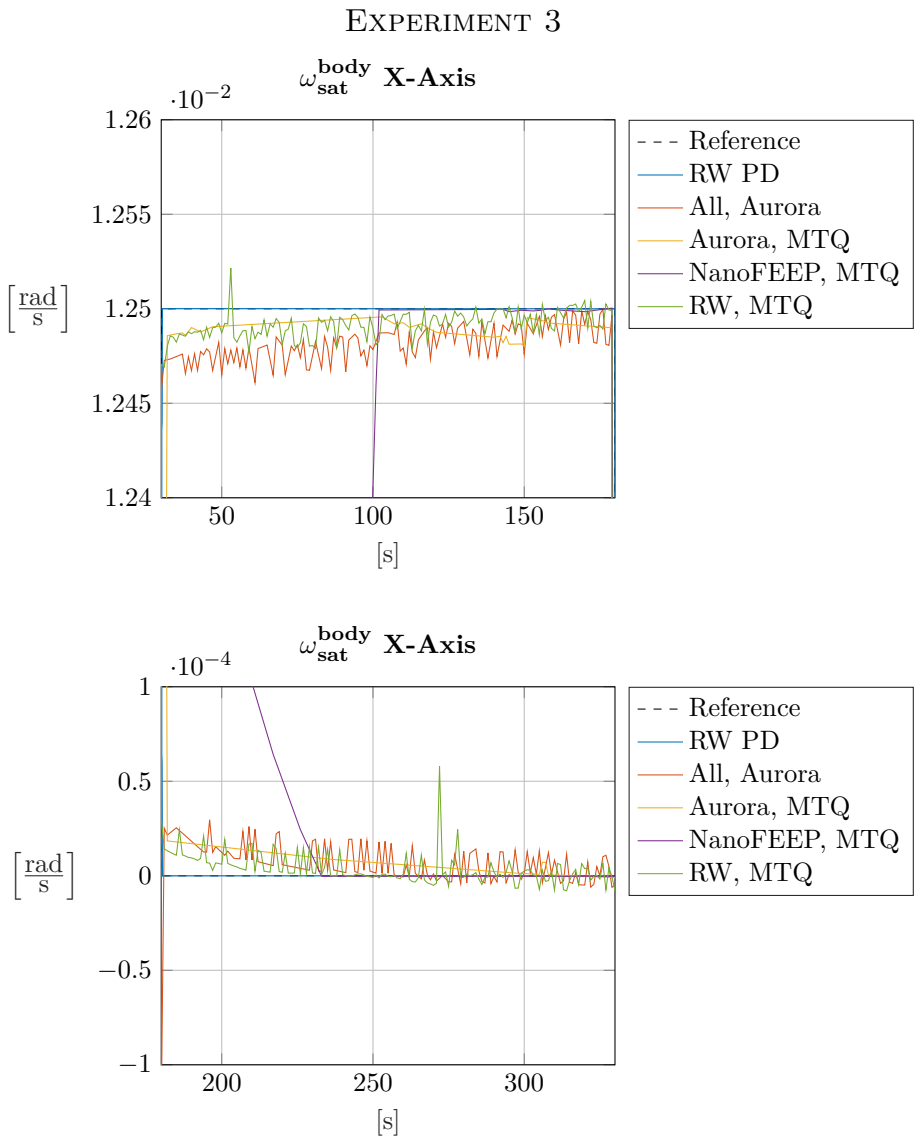

Figure 6.30: Magnification of the Steady State Accuracy in Satellite Body Frame Angular Velocity of Experiment 3.

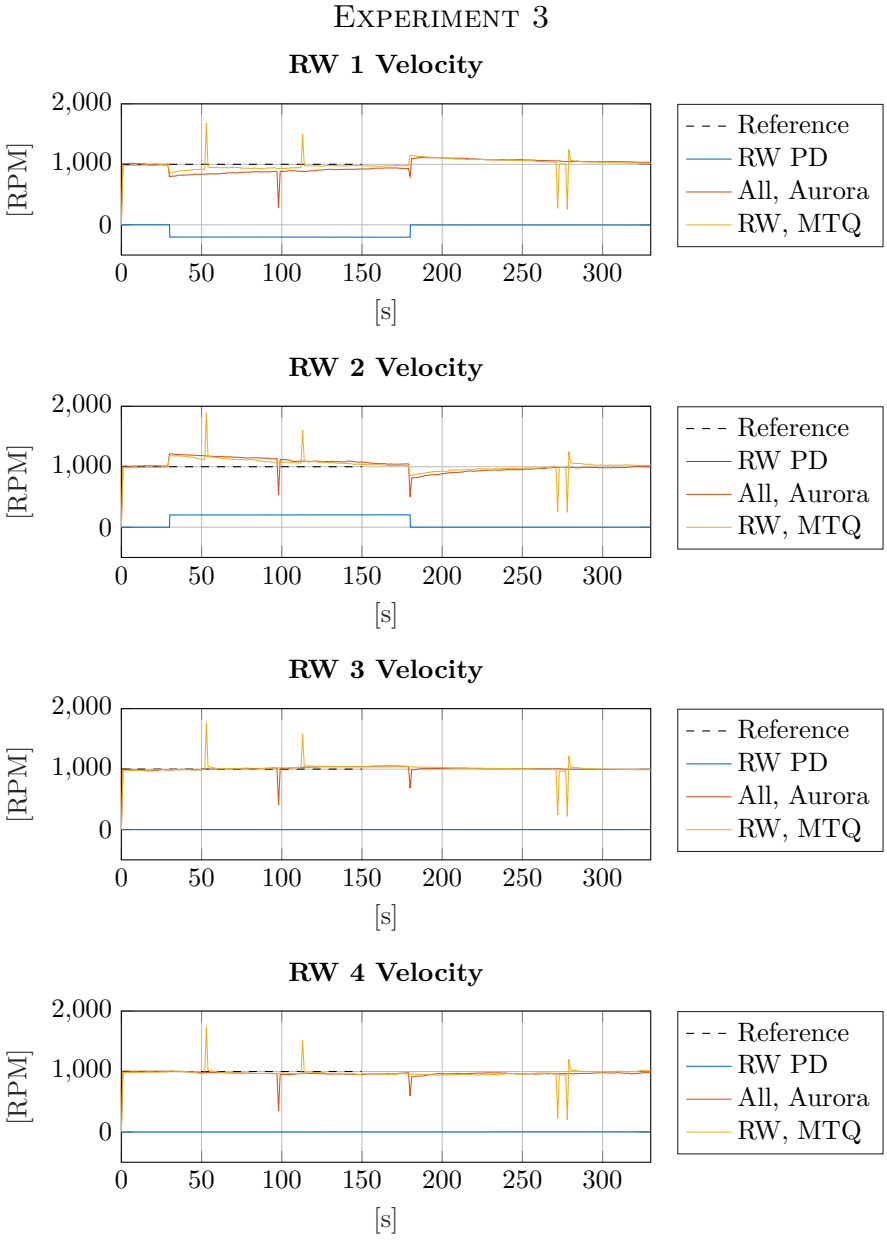

Figure 6.31: Reaction Wheels Velocities in Experiment 3.

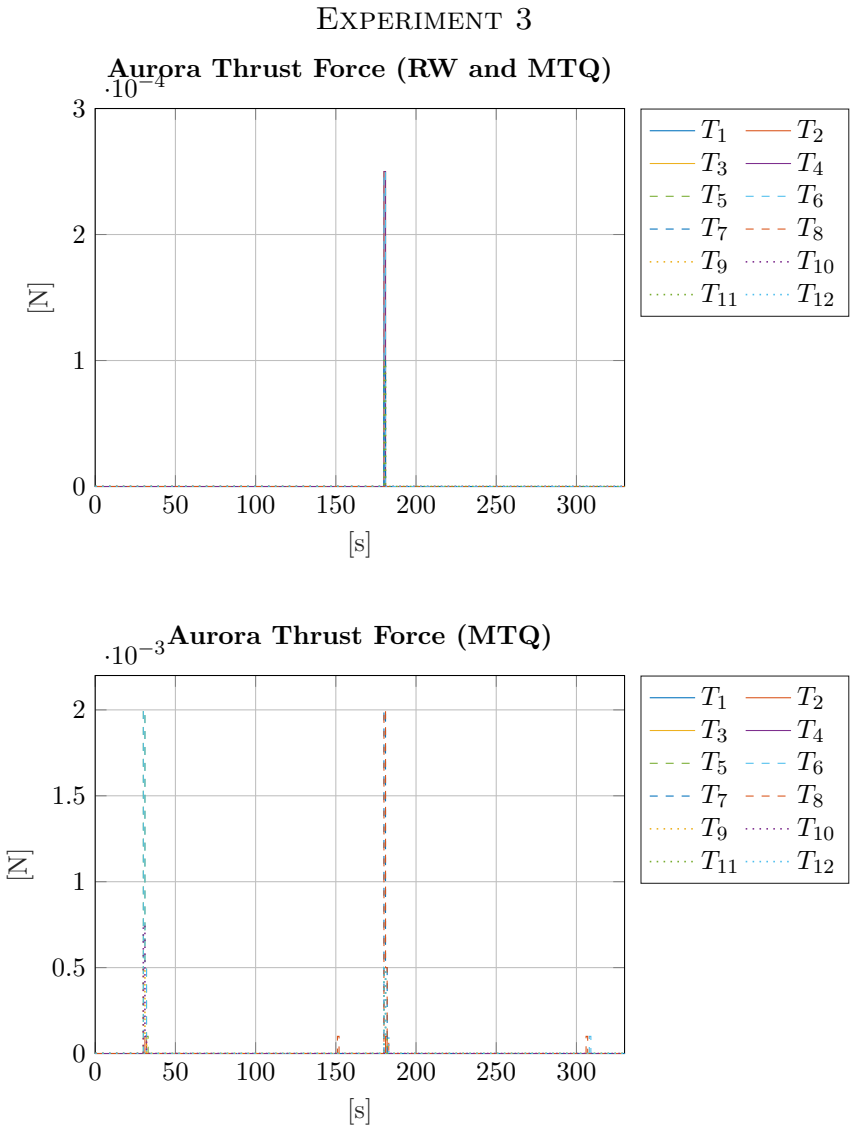

Figure 6.32: Applied Force by the Aurora Propulsion System in Experiment 3.

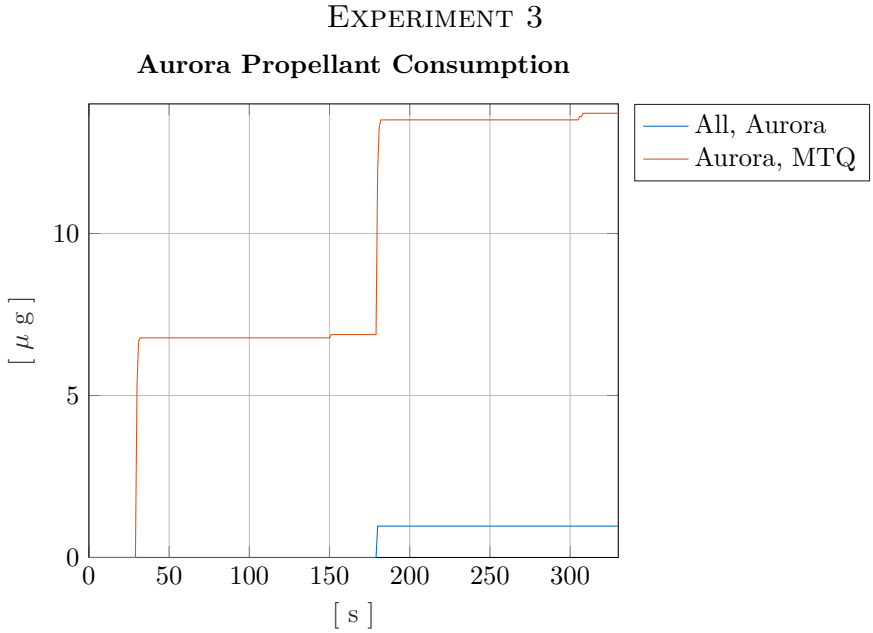

Figure 6.33: Cumulative Representation of Propellant Consumption of the Aurora Propulsion System in Experiment 3.

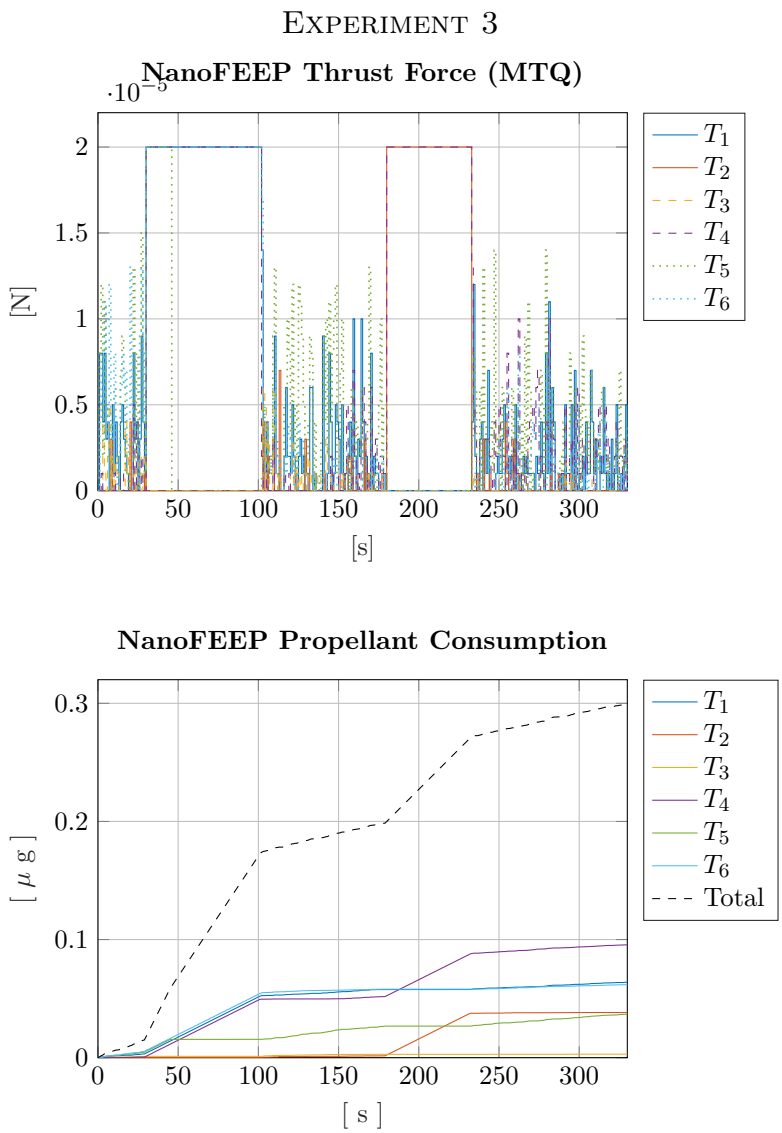

Figure 6.34: Applied Thrust Force and Cumulative Representation of Propellant Consumption of the NanoFEEP Thrusters in Experiment 3.

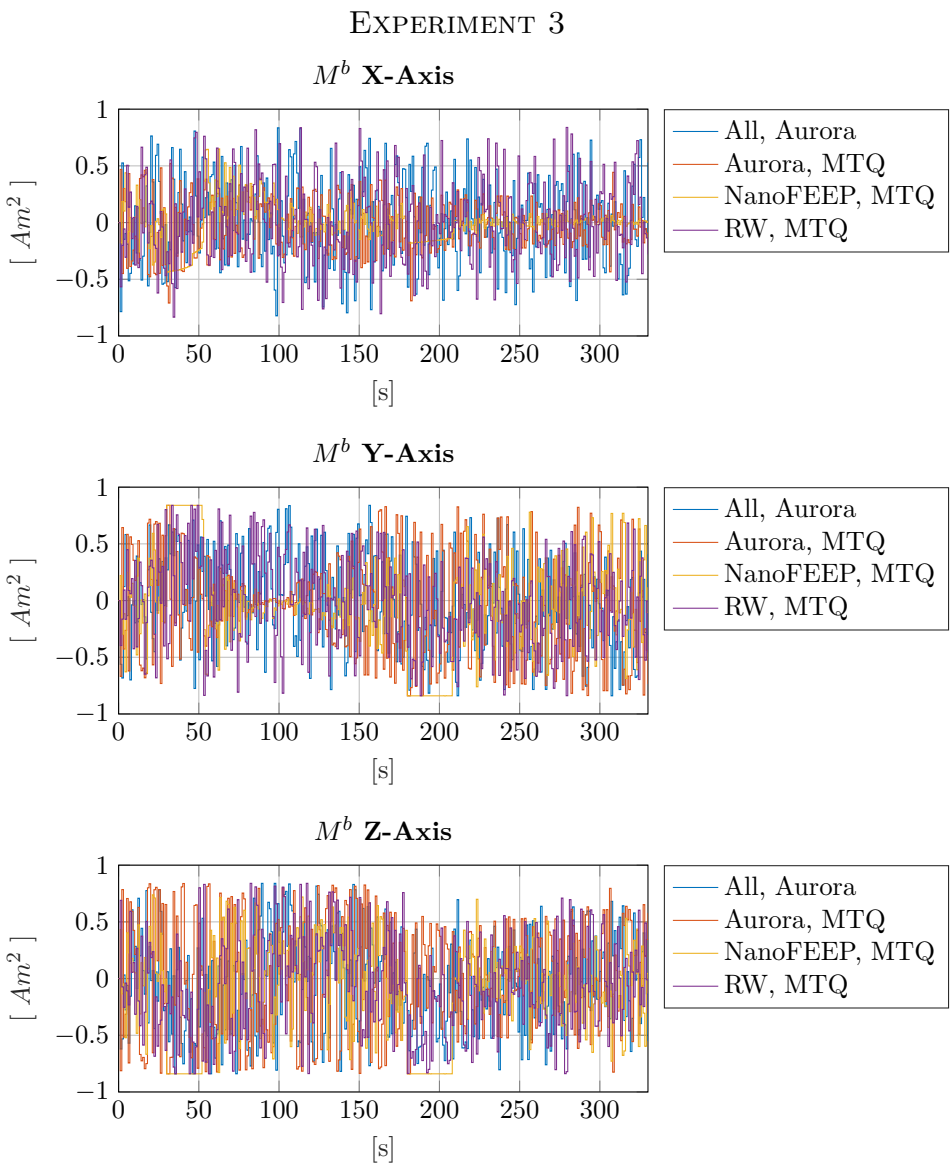

Figure 6.35: Applied Dipoles of the Mangetorquer in Experiment 3.

6.5 Experiment 4

The fourth experiment is designed to test the momentum dumping capabilities of the MPC. The reaction wheels are initialized in a saturated state, and the controller's objective is to reach the reference reaction wheel momentum while keeping the satellite in approximately the same orientation. The initial conditions for the experiment are given in table 6.12, and the objectives are presented in table 6.11. Table 6.13 provides the controller parameters for the different actuation scenarios.

Figure 6.36 presents the reaction wheel velocities for the different actuation scenarios. The satellite attitude response is given in Figure 6.37 using Euler angles, and in Figure 6.38 using the attitude error quaternion.

The magnetorqer actuation is presented in Figure 6.39, and the actuation of the Aurora and NanoFEEP propulsion systems in Figure 6.40.

Experiment 4 Objective	
Reference Orientation Quaternion	$\begin{bmatrix}1 & 0 & 0 & 0\end{bmatrix}'$
Reference Reaction Wheels Velocities	1000 RPM $\cdot \begin{bmatrix}1 & 1 & 1 & 1\end{bmatrix}'$

Table 6.11: Objectives of Experiment 4.

Experiment 4 Initial Conditions	
Time	12:00:00 31.10.2005
Periapsis, Apoapsis	500 km, 500 km
Inclination	97 deg
Right Ascension of the Ascending Node	0 deg
Argument of Perigee	0 deg
True Anomaly	45 deg
Initial Attitude Quaternion	$\begin{bmatrix}1 & 0 & 0 & 0\end{bmatrix}'$
Initial Rotational Velocity	$\begin{bmatrix}0 & 0 & 0\end{bmatrix}'$
Initial Reaction Wheel Velocities	6500 RPM $\cdot \begin{bmatrix}1 & 1 & -1 & -1\end{bmatrix}'$

Table 6.12: Initial Satellite Conditions in Experiment 4.

Experiment 4 Controller Parameters								
MPC	Freq.	PH	ζ_a	ζ_ω	ζ_m	κ_{MTQ}	κ_T	κ_{RW}
Aurora	1 Hz	3	10^{14}	0	10^6	0	10^{12}	10^6
NanoFEEP	1 Hz	3	10^{14}	0	10^6	0	10^6	10^6
MTQ	1 Hz	3	10^{14}	0	10^6	1	0	10^6

Table 6.13: Parameters used in Experiment 4 for the Model Predictive Controller. The frequency parameter governs how often the control signals are updated. The PH parameter sets the length of the Prediction Horizon in the MPC. The cost of the attitude deviation is given by ζ_a, angular velocity deviation by ζ_ω, and the cost of the reaction wheel momentum deviation is given by ζ_m. κ_{MTQ}, κ_T, and κ_{RW} are the factors by which the Magnetorquer, Thruster and Reaction Wheels actuation weights are multiplied by, respectively.

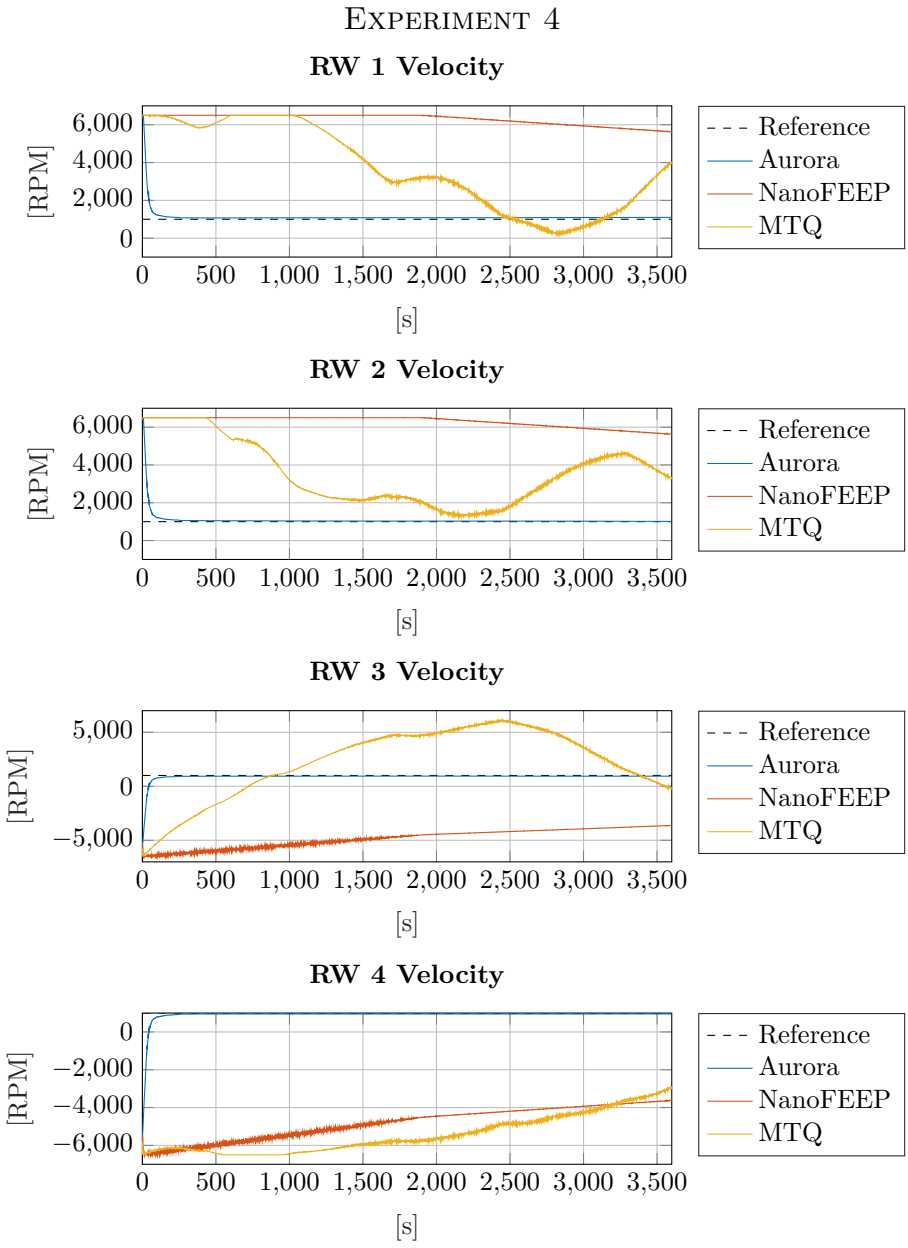

Figure 6.36: Reaction Wheels Velocities in Experiment 4.

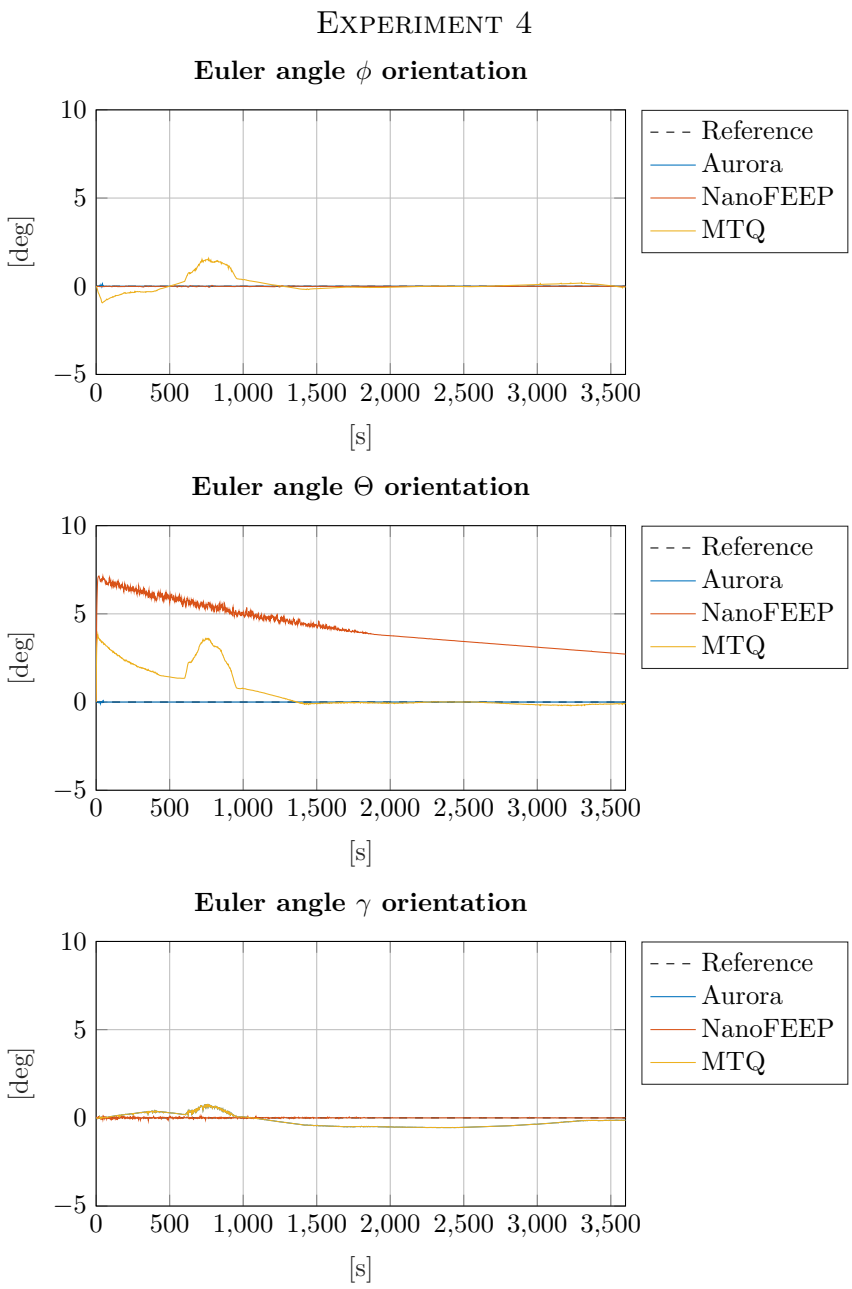

Figure 6.37: Satellite attitude response in Experiment 4, measured in Euler ϕ, Θ and γ angles (*zyx* convention).

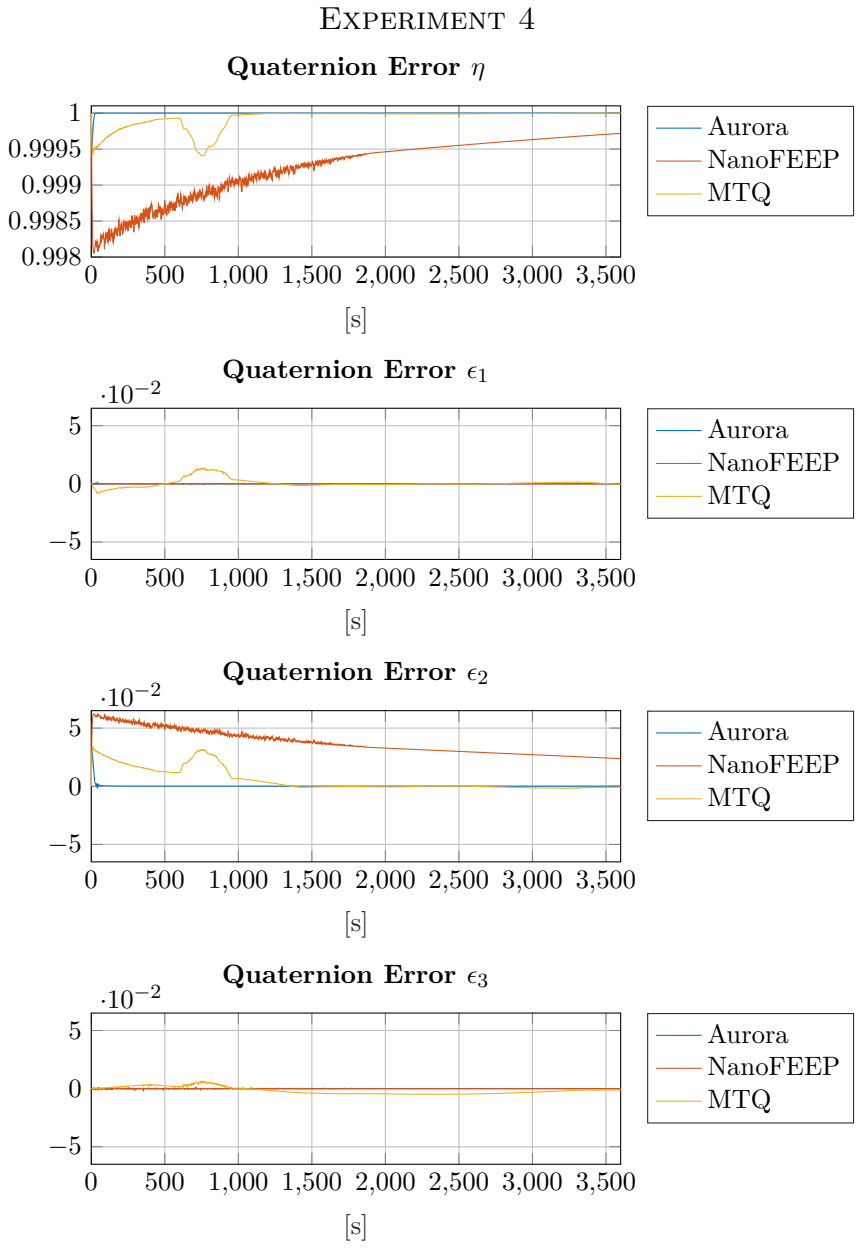

Figure 6.38: Attitude quaternion deviation in Experiment 4.

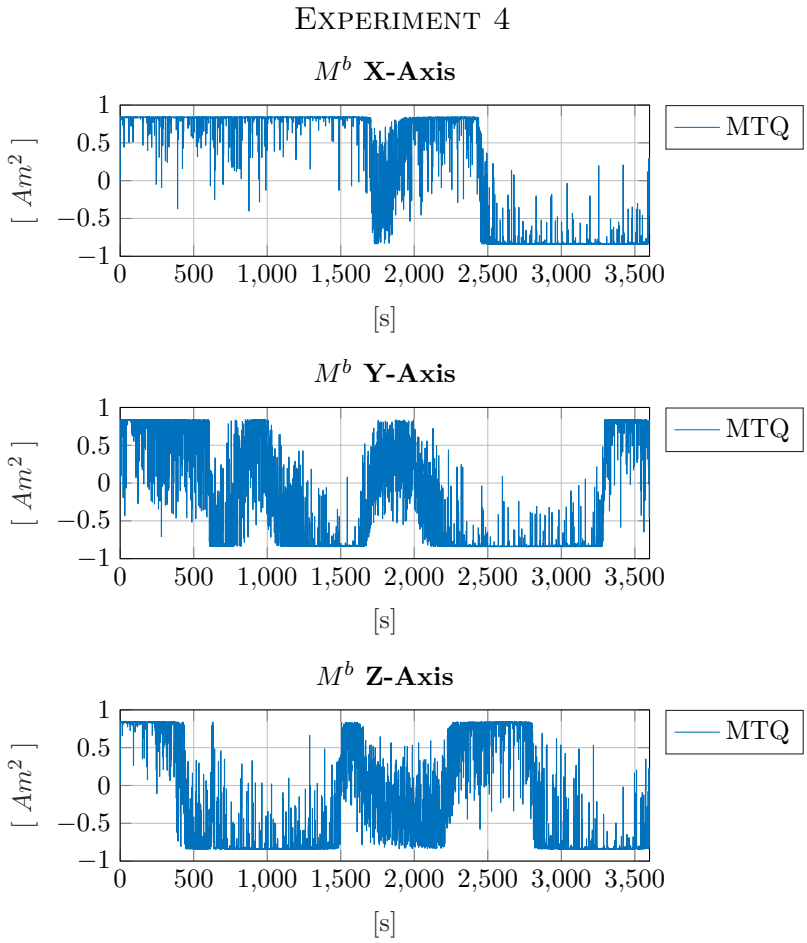

Figure 6.39: Dipole strengths applied by the magnetorquer actuator in Experiment 4.

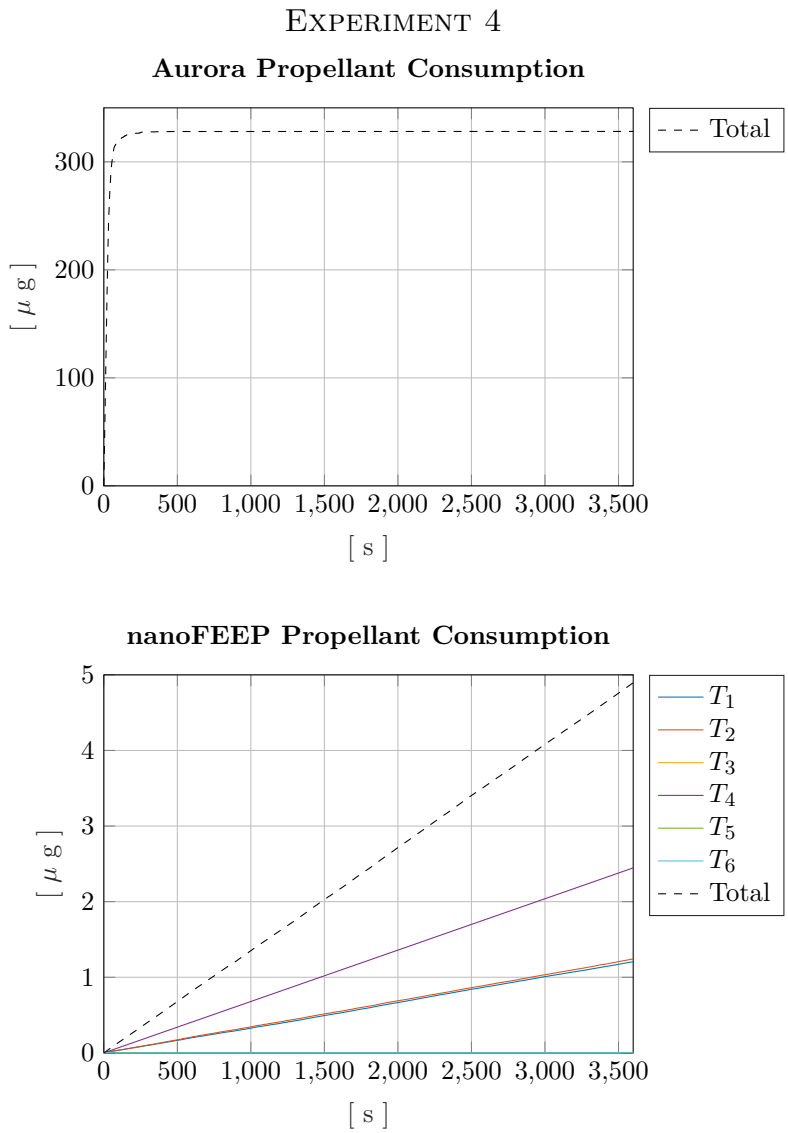

Figure 6.40: Cumulative representation of propellant consumption of the Aurora and NanoFEEP propulsion systems in Experiment 4.

6.6 Summary of Results

This section summarizes the results from the four experiments carried out.

The first experiment showed that all actuator configurations performed best on small momentum maneuvers with the shortest possible prediction horizon. For the large momentum maneuver, the different actuator configurations' optimal prediction horizons seemed to correspond with the torque producing capabilities. With the reaction wheels present, which is the most potent attitude actuator in the simulations, the estimated optimal prediction horizon on large momentum maneuvers was just three, but for the low-powered NanoFEEP thruster system, the optimal prediction horizon was 150.

The second experiment considered large momentum rest-to-rest attitude maneuvers. The measured settling times show that the reaction wheels in combination with MPC and PD control show comparable results. The Root-Mean-Square error post settling is lower for the MPC than the PD controller. The NanoFEEP propulsion system was shown to result in considerably slower attitude dynamics, with a settling time ten times slower than the actuator configuration with reaction wheels, and three times slower than the configuration based on the Aurora propulsion system. Although slower, the NanoFEEP propulsion system was noticeably more precise in steady-state tracking compared to the Aurora propulsion system.

Small momentum maneuver performance was investigated in the third experiment. Here, the reaction wheel actuator paired with PD control drastically

outperformed the other solutions, comprising a much lower post-settled RMS error. The NanoFEEP propulsion system showed significantly lower post-settle RMS error than the remaining MPC configurations. All actuator configurations except the NanoFEEP system were capable of tracking the reference slew rate with almost no transient period, except from the NanoFEEP propulsion system, which showed adverse settling times. The settling time for the NanoFEEP system was close to one minute, whereas the remaining configurations had settled within three seconds.

The fourth experiment investigated the ability of the controller and actuators to dump excess reaction wheel momentum. The Aurora propulsion system, capable of producing the most considerable torques, far outperformed the magnetorquer and NanoFEEP propulsion system. The performance of the magnetorquer and NanoFEEP thrusters was comparable. The dynamics of the system actuated by the magnetorquer were faster, but the system actuated by the NanoFEEP thrusters was more stable.

Chapter 7

Discussion

This study set out with the aim of assessing the performance of propulsion systems in attitude control of nanosatellites. The project involved designing an optimal attitude controller and analyzing its performance using different actuation solutions. Section 7.1 discusses the developed controller, and section 7.2 discusses the different actuators' performance .

7.1 Controller

This section discusses the developed optimal controller. Subsection 7.1.1 discusses the reasoning that led to the model predictive controller design, and subsection 7.1.2 discusses the performance observations made in the experiments. As the proportional-derivative controller was included only to establish a performance basis for comparison, it will only be discussed in subsection 7.1.2 *Controller*

Performance.

7.1.1 Choice of Controller

The choice of an adaptive model predictive controller was based mainly on the properties of a satellite propulsion system. Here, the force from the thrusters is modeled as an integer value, assigned from a predefined set of possible force values. This was considered a reasonable simplification, as the minimum impulse bit property and output uncertainty are two of the main limitations of propulsion systems. Although seen as necessary, the integer behavior complicates the control aspect of such systems. A predictive control approach was chosen to enable the system to handle the future impact of generated satellite momentum and plan propulsion impulses accordingly.

Although the satellite dynamics are nonlinear by nature, a linearization of the system was used to simplify derivations and decrease the controller's computational load. The controller was made adaptive such that new linearizations could be made at each timestep, to better represent the system dynamics around the current operating point of the satellite. One of the drawbacks of the linearization is that the satellite dynamics are not well represented outside a small region of the current operating point, which decreases the accuracy and thus the optimality gain of long prediction horizons. This could explain the controller overshooting the reference.

The controller needed to be able to handle multiple actuators working in conjunction, incorporating both integer and continuous control signals. The resulting

optimization problem is a mixed-integer quadratic program (MIQP). The problem is defined using linear constraints, a quadratic cost function, and a subset of the control signals being integral. As MIQP is NP-hard, it was decided to allow sub-optimal solutions, to increase computational efficiency. The MATLAB genetic algorithm solver *ga()* from the Global Optimization Toolbox was chosen as the solver. The choice was based on the fact that it incorporated all the necessary features and performed better than other candidate solvers such as the MATLAB surrogate optimization algorithm *surrogateopt()*. One of the drawbacks of the genetic algorithm solver is that it does not necessarily converge towards the optimum, and is prone to local minima convergence. As a design choice, the solver was specified with a maximum computational time allowance.

The resulting adaptive MPC had several parameters that needed to be defined. They included (1) the *controller timestep*, (2) the *prediction horizon length*, (3) the *satellite state weights*, and (4) the *actuation weights*. The results of the first experiment confirmed that the best-suited values for the parameters depended on the actuator and reference trajectory specification, and it was decided to differentiate the parameter values based on this. The different parameter configurations can be seen as different modes of operation for the controller.

Initially, it was believed that the shortest possible MPC **controller timestep** would perform the best. Surprisingly, simulations with controller timesteps of less than one second were found to perform worse than simulations with a controller timestep equal to one second. It is difficult to explain this result, but it might be related to the fact that an increased number of predicted steps are needed to cover the same period of satellite dynamics; In case the pre-

diction horizon is not increased when the timestep length is decreased, this could make the predicted dynamics miss out on the future impact of satellite momentum. If the prediction horizon is increased, this will allow more steps to be taken away from the point of linearization, which possibly makes the predicted dynamics less accurate. As a result, the controller timestep of one second could be a compromise between the controller's adaptiveness and stability.

Increasing or decreasing the **prediction horizon length** was shown in the first experiment to come with both positive and negative effects. Longer prediction horizons made the controller better at handling reference trajectories involving substantial satellite momentum with minimal reference overshoot. On the other hand, steady-state precision increased with shorter prediction horizons. A possible explanation for these results is that the linearization of the satellite dynamics and the unaccounted perturbing forces decrease the prediction accuracy, favoring shorter prediction horizons when the objective is tracking a steady-state reference. Although the prediction might not be accurate enough for precise tracking, it was shown to provide the system with momentum handling capabilities.

The **satellite state weights** and the **actuation weights** were determined based on trial and error. These results, therefore, need to be interpreted with caution. The actuation weights were based on the power consumption models, with the initial idea being that optimal control could be derived to minimize energy consumption. However, it was shown in the simulations that this could lead to unwanted excess use of certain actuators. Additionally, the propellant consumption of the propulsion system had to be limited, which does not directly correspond to power usage. For the reasons mentioned above, it was decided

to add a scaling factor to the actuation weights, which could be altered freely. The inclusion of scaling factors makes the actuation weights no longer represent actual power consumption, but rather the author's preferred actuator response. Similarly, the satellite state deviation weights were chosen freely to provide sufficient but not excessive actuation, and a preferred emphasis on some of the controlled satellite states compared to other states.

The developed MPC handles actuators being switched on and off and change of control objectives at any point in time, making it a robust all-in-one solution for attitude control. With moderate further development, the controller could be extended to control both satellite attitude and position. This would enable complex operations such as formation flying and rendezvous maneuvers. However, the MPC's large computational load, combined with the inaccuracies at low controller frequencies, could make the solution unsuitable for onboard processing. Real-time and onboard processing capabilities are necessary performance measures for a satellite attitude control system, and a further study with more focus on performance is therefore suggested.

7.1.2 Controller Performance

An advantage of the developed model predictive controller is the simultaneous tracking of multiple control objectives. The controller can regulate both the satellite attitude, slew rate, and reaction wheel velocities in a minimal cost fashion. This was highlighted in the fourth experiment, in which the controller, combined with different actuators, was set to desaturate the reaction wheels with a limited effect on the satellite attitude. Additionally, the MPC's ability to

predict changes in the reference signal makes it perform well on settling time measures.

In the second experiment, concerning a large momentum maneuver, the reaction wheels in combination with the PD controller showed more significant post-settling Root-Mean-Square errors than the MPC. When studying these results, it is observed that near the reference trajectory, the PD controller continues to converge slowly towards the desired value, whereas the MPC oscillates around the reference. It can, therefore, be assumed that the RMS error comparison depends on the duration of the experiment; On a short time-scale, the MPC is shown to perform better, whereas, on a longer time scale, the PD controller is believed to outperform the MPC.

An observed disadvantage of the MPC is the failure of the control signals to converge, which leads to wear and tear on the actuators. A shorter time period may potentially help converge the control signals, as this was the case for the PD controller, but as previously discussed, a shorter MPC timestep is not considered realistic in terms of computational load.

It is assumed that the more powerful actuators quickly exceed the validity region of the linearized system in the MPC prediction, and thus shorter prediction horizons perform better for these systems. This was observed in the second experiment when the reaction wheels actuator was compared to the Aurora and NanoFEEP propulsion systems. The same argument about the region of estimation for the linearization is used on the small momentum maneuver of experiment three; When emphasize is put on the accuracy of the controller,

the best performance is achieved with the shortest possible prediction horizon, which keeps the dynamics close to the point of linearization. Regardless of these limitations, the prediction of satellite dynamics enables the controller to handle satellite momentum, which is shown both in the case of powerful and less powerful actuator configurations.

7.2 Actuators

Three types of attitude actuators were included in the simulations: magnetorquers, reaction wheels, and a propulsion system. This section compares and discusses the different actuators.

First, the benefits and drawbacks of each actuator is discussed, in subsection 7.2.1 *Magnetorquers*, subsection 7.2.2 *Reaction Wheels*, and subsection 7.2.3 *Propulsion Systems*. Then, combinations of actuators and the comparative performances are discussed in subsection 7.2.4 *Actuator Combinations and Comparisons*.

7.2.1 Magnetorquers

Magnetorquers are highly compact and lightweight actuators, commonly used for satellite detumbling purposes. The torque production is restricted to being perpendicular to Earth's magnetic field, a property that limits the attitude control precision. The torque direction limitation is less restrictive in orbits where Earth's magnetic field has significant variations in direction, such as polar orbits. In this case, the satellite orientation can be fully actuated in the course

of a full orbit. As a result of these properties, the magnetorquer is best suited for steady-state attitude maneuvers.

The magnetorquer can be combined with other actuators to achieve secondary objectives. An example of this is momentum dumping of reaction wheels, which was simulated in Experiment 4. Here, the magnetorquer was shown to perform well on desaturating maneuvers, with results comparable to the NanoFEEP propulsion system. It could also be combined with propulsion modules to achieve torques smaller than what is achievable through the minimum impulse bit of the propulsion system.

7.2.2 Reaction Wheels

Reaction wheels enable precise satellite attitude control through internal momentum exchange and are suitable for all attitude maneuvers studied in this thesis.

The drawbacks of the reaction wheel actuator are mostly related to the weight and mechanical lifetime of the components. The flywheel is required to have certain inertia for the momentum exchange to be effective, and an assembly of three actuation wheels are needed for full three degrees of freedom actuation, with a fourth reaction wheel typically included for redundancy purposes. This makes it a relatively large and heavy actuator.

As the actuator is based on internal momentum exchange, the flywheels of the actuator are prone to saturating due to external torques from perturbing forces and require frequent momentum dumping maneuvers. Secondary attitude actua-

tors that produce external momentum are needed to perform such desaturating maneuvers.

7.2.3 Propulsion Systems

Two different propulsion systems were studied in this thesis. The NanoFEEP system is compact and lightweight, with a very small force output. The Aurora propulsion system takes up more space and requires more propellant, but produces a more significant force. In terms of torque producing capabilities, the Aurora propulsion system can produce about one hundred times more torque than the NanoFEEP system, although the Aurora system only produces one-tenth of the reaction wheel assembly's combined torque.

The different specifications led to different qualities being present. The performance on high momentum maneuvers is governed by the ability to produce large forces. By this measure, the Aurora thruster, which can produce 2 mN, outperforms the NanoFEEP system, which produces 20 μN. Pointing and slew rate accuracy is believed to be highly dependent on the minimum impulse bit of the propulsion system, as the momentum corrections made by the actuators ideally need to converge towards zero. Opposite of what was the case for the high momentum maneuvers, this leads to the less powerful actuator performing the best.

In terms of size and weight, the two propulsion systems vary greatly. The Aurora Propulsion Technologies *AOCS* assembly has a dry mass in its most extensive configuration of about 350 grams and takes up approximately 0.5 U,

including the propellant tank. The individual NanoFEEP thrusters weigh in at 6 grams and take up 3 cm^3 each, and thus a system of six thrusters weighs less than 40 grams and takes up about 0.02 U. For comparison, the weight of the NanoAvionics *CubeSat Reaction Wheels Control System SatBus 4RW0* is approximately 665 grams when the harness is excluded, and the size is 0.5 U. Designing the attitude control system with NanoFEEP thrusters could achieve considerable weight and space savings on the satellite. The Aurora propulsion system has customizable propellant storage, and with careful mission analysis, it could be possible to achieve a weight saving over the reaction wheel assembly if the propellant requirement is low.

Propulsion units also bring with them advantages that are not studied in this thesis. The use of external force from a thruster enables orbital maneuvers, which opens up an array of features; These include prolonging the lifespan of the satellite by compensating the loss of orbital momentum due to atmospheric drag and other perturbing forces, micro-adjusting the orbit after launch, engaging in controlled formation flying, and facilitating a means of deorbiting the satellite as an end-of-life procedure to comply with space-debris regulations. Combining the orbit and attitude control in one actuator could make it possible to save weight and space on the satellite.

Considering the HYPSO mission specifically, the possibility of propellant residue on the camera lens should be examined, as such contamination could place risk on the satellite's mission.

7.2.4 Actuator Combinations and Comparisons

Table 7.1 presents design and performance measures related to the actuators. The reaction wheels assembly is the heaviest actuator. However, as the flywheel inertia requirement is small on nanosatellite, a lighter alternative to the NanoAvionics *CubeSat Reaction Wheels Control System SatBus 4RW0* could be considered, which would make the difference on reaction wheels and propulsion systems in terms of weight, and thus launch costs, minimal.

Actuator Data					
	Max Torque [Nm]	Min Torque [Nm]	Dry Mass [kg]	Simulated Mass [kg]	Volume [cm^3]
RWs	$5.90 \cdot 10^{-3}$	0.0	0.665	0.665	500.0
Magnetorquer	$2.69 \cdot 10^{-5}$	0.0	0.186	0.186	27.7
Aurora	$6.92 \cdot 10^{-4}$	$1.73 \cdot 10^{-5}$	0.350	0.450	500.0
NanoFEEP	$3.46 \cdot 10^{-6}$	$1.73 \cdot 10^{-7}$	0.036	0.096	18.0

Table 7.1: Comparison Table of the Actuator Data.

Several actuator combinations were considered in the simulations. The combination of reaction wheels and the Aurora propulsion system would take up much space on the satellite and lead to a heavy design, which makes it a less desirable combination. Reaction wheels combined with the NanoFEEP propulsion system is potentially a good combination in terms of performance, size, and weight, and could lower the power consumption compared to a system in which the magnetorquer is applied. In the third experiment, it was observed that using

only the reaction wheels in combination with a PD controller led to the smallest steady-state RMS error. If the MPC was to be used, the combination of NanoFEEP thrusters and a magnetorquer had the most precise control, whereas the combination of Aurora thrusters and a magnetorquer had the worst precision.

Chapter 8

Conclusions

This thesis set out to examine the use of propulsion systems on nanosatellites. Despite its exploratory nature, this research has led to the development of a modular dynamical satellite model, an orbital simulator with space environment disturbances, and an optimal controller for pointing and slew maneuvers in the form of an Adaptive Model Predictive Controller.

These results add to the rapidly expanding field of nanosatellite technology, and the insights gained from this study may be of assistance to the NTNU SmallSat Lab in specifying future satellite designs by providing a deeper insight into the use of miniaturized propulsion systems.

The main limitation of the developed attitude controller is the heavy computational load, which makes on-board computing difficult. An additional weakness is the observed failure of the control signals to converge, which causes significant

wear and tear on the actuators. In spite of its limitations, the controller certainly contain valuable properties. The predictive approach was shown to successfully control the nonlinear propulsion actuators, manage satellite momentum, simultaneously utilize a variety of actuators, and handle several objectives at once. When tracking a reference slew rate over a short time period, the developed Model Predictive Controller was shown to achieve a lower Root-Mean-Square error compared to the Proportional-Derivative Controller.

Reaction wheels are prone to momentum buildup over time caused by external forces acting on the satellite. This study has shown that there is potential for power savings onboard the satellite by utilizing a minituarized propulsion system to dump excess reaction wheel momentum compared to the more commonly used magnetorquer actuator.

The scope of this research was limited in terms of the simulation duration and the number of scenarios studied. Notwithstanding these limitations, the results of this research suggest that a lightweight Proportional-Derivative Controller in combination with a Reaction Wheel assembly is the most suitable solution for the HYPSO satellite's mission. This is argued based on the simulated performance, stability of the controller, and possibly neglible additional size and weight of a reaction wheel assembly compared to a propulsion based system. That being said, the inclusion of a propulsion system on a nanosatellite is interesting from a research perspective, as there is little published data on this matter.

8.1 Further Work

Further research could usefully explore how implementing a more detailed model of the thruster dynamics improves prediction and simulation accuracy. Another question raised by this study is whether avoiding prediction linearization would improve the controller performance. In this case, a nonlinear control approach needs to be applied.

Another natural progression of this work is to look at whether adaptively changing controller's timestep and prediction horizon length while it is running could help improve its computational efficiency. Additionally, decoupling the attitude dynamics by tracking the principal axes of the system could potentially make it easier to compute the control gains. A greater focus on reducing the computational load of the controller could produce interesting results with real-world flight potential, which would be a fruitful area for further work.

Looking beyond the scope of this research, the use of propulsion systems on nanosatellites enables the satellite operator to perform orbital maneuvers in addition to attitude control. The force of the propulsion system may be utilized to perform orbital corrections, prolong the satellite's lifespan by counteracting orbital decay, and perform controlled end-of-service deorbiting. Orbital corrections are essential for rendezvous maneuvers and formation flying, which have applications in several fields of research, and is essential in active space debris removal.

Bibliography

[1] European Space Agency. *CubeSats*. 2020. URL: https://www.esa.int/Enabling_Support/Preparing_for_the_Future/Discovery_and_Preparation/CubeSats (visited on 06/06/2020).

[2] Aurora Propulsion Technologies Oy. *Aurora Products*. 2020. URL: https://www.aurorapt.fi/home/products/ (visited on 05/08/2020).

[3] Daniel Bock and Martin Tajmar. "Highly miniaturized FEEP propulsion system (NanoFEEP) for attitude and orbit control of CubeSats". In: *Acta Astronautica* 144 (Jan. 2018).

[4] Wanpracha Chaovalitwongse, Ioannis Androulakis, and Panos Pardalos. "Quadratic Integer Programming: Complexity and Equivalent Forms". In: *Encyclopedia of optimization. 7 Vols. 2nd revised and expanded ed* (Jan. 2008).

[5] Howard D. Curtis. *Orbital Mechanics for Engineering Students*. 2nd ed. Elsevier, 2009.

[6] Olav Egeland and Jan Tommy Gravdahl. *Modeling and simulation for automatic control*. Wiley, 2002.

[7] T.I. Fossen. *Handbook of Marine Craft Hydrodynamics and Motion Control*. Wiley, 2011.

[8] Hellerick. [Published under the *Creative Commons Attribution-Share Alike 3.0 Unported* License]. June 2013. URL: https://en.wikipedia.org/wiki/File:Division_of_the_Earth_into_Gauss-Krueger_zones_-_Globe.svg (visited on 05/04/2020).

[9] Morten Hovd. *A brief introduction to Model Predictive Control*. Engineering Cybernetics Department, NTNU. Mar. 2004.

[10] Swapna Krishna. *The rise of nanosatellites*. 2018. URL: https://theweek.com/articles/761349/rise-nanosatellites (visited on 06/06/2020).

[11] Bjørn Kristiansen. "Nonlinear Attitude Control of a Pointing and Slewing Spacecraft". MA thesis. Norwegian University of Science and Technology, 2019.

[12] Lasunncty. [Published under the *GNU Free Documentation License*]. Oct. 2007. URL: https://commons.wikimedia.org/wiki/File:Orbit1.svg (visited on 12/02/2019).

[13] Meysam Mahooti. *High Precision Orbit Propagator*. https://www.mathworks.com/matlabcentral/fileexchange/55167-high-precision-orbit-propagator. 2019.

[14] MathWorks. *ga*. 2020. URL: https://se.mathworks.com/help/gads/ga.html?s_tid=srchtitle (visited on 06/15/2020).

[15] W.D. McClain and D.A. Vallado. *Fundamentals of Astrodynamics and Applications*. Space Technology Library. Springer Netherlands, 2001.

[16] Arash Mehrparvar. "CubeSat Design Specification". In: (Feb. 2014).

[17] Melanie Mitchell. *An Introduction to Genetic Algorithms*. Cambridge, MA: MIT Press, 1996.

[18] Nano Avionics. "Reaction Wheels Datasheet NA-4RW0-G0-R6". June 2018.

[19] A.H. de Ruiter, C. Damaren, and J.R. Forbes. *Spacecraft Dynamics and Control: An Introduction*. Wiley, 2013.

[20] Loren Shure. *ODE Solver Selection in MATLAB*. 2015. URL: https://blogs.mathworks.com/loren/2015/09/23/ode-solver-selection-in-matlab/ (visited on 05/08/2020).

[21] J. Sanz Subirana, J.M. Juan Zornoza, and M. Hernández-Pajares. *Conventional Celestial Reference System*. 2011. URL: https://gssc.esa.int/navipedia/index.php/Conventional%5C_Celestial%5C_Reference%5C_System (visited on 11/12/2019).

[22] Theodore Wildi. *Electrical Machines, Drives, and Power Systems, SixthEdition*. Prentice Hall, 2006.

Carl Martin Krokeide

Propulsion-based Attitude Control of Nanosatellites

NTNU
Norwegian University of
Science and Technology